THE UNIVERSITY *of* EDINBURGH

Structure, Dynamics and the Role of Particle Size in Bicontinuous Pickering Emulsions

Matthew Reeves

Doctor of Philosophy
The University of Edinburgh
2016

Abstract

Bicontinuous Pickering emulsions (or bijels) are a relatively new class of novel soft material with many potential industrial applications, including microfluidics, tissue engineering and catalysis. They are typically formed by initiating the spinodal decomposition of a binary liquid mixture in the presence of neutrally-wetting colloidal particles. The particles attach at the liquid-liquid interface and arrest the phase separation by jamming when the concentration of particles approaches the 2D close-packing limit. Predicted by simulations in 2005 and realized in the laboratory in 2007, many aspects of the bijels complex behaviour and properties have remained unexplored. This thesis expands the knowledge of the bijels structural and dynamical properties, while focusing specifically on the role of particle size.

The bijels porosity (average interfacial separation L) according to simulations can be controlled by varying the size r and volume fraction ϕ of particles in the system ($L \propto r/\phi$). The inverse scaling of L with ϕ has been verified for one size of particle, but to access smaller values of L (to allow the structure to be used for a wider range of industrial applications) the scaling with r must be tested. Chapter 3 presents the first systematic study of reducing particle size in bijels made with the liquid pair water/lutidine (W/L). We find that a five-fold reduction in r only requires moderate modification to preparation methods (concentrations of reactants during particle synthesis and increased particle sonication time) and in principle allows L values of between 1 & 10 μm to be accessed in the W/L system, where previously 10 μm was the limit. We demonstrate that this reduced lower bound of L can be translated into a lower bound for polymerized bijels also. Unfortunately, reducing particle size even further (in the same way) reveals a law of diminishing returns, as the uptake fraction of particles to the interface also reduces as we reduce particle size. Hence, to reduce lengthscale even further, a new bijel fabrication paradigm is required. Unexpectedly, we find that the

temperature quench rate becomes less important for smaller particles (which constitutes a direct material synthesis advantage) and develop a new theoretical framework to take account of this observation. Large particles promote domain pinch-off during the coarsening (due to a larger driving force towards spontaneous curvature) resulting in bijel failure when slow rates are used because the time required to jam is greater than the time required for depercolation.

To further probe the bijels structure as a function of particle size and quench rate, and to account for the success/failure scenarios which seem not to depend on L, in Chapter 4 we quantitatively characterize the morphology by measuring distributions of interfacial curvatures. By computing area-averaged quantities to make valid comparisons, we find that smaller particles and faster quench rates produce bijels with greater hyperbolic 'open' character, aligning with our understanding of bijel formation gained from Chapter 3. We compare to simulated bijel data and an estimate of the hyperbolicity of the bare liquids undergoing spinodal decomposition, validating the results. In addition, we uncover a time-dependent 'mutation' of the curvature distributions when large particles are used, but not when smaller particles or a different liquid pair is used. The mutation appears to correlate with the propensity of the interfacial particles to form a 'monogel', whereby the interfacial particles develop permanent bonds and remain as a 3D percolating network after the interface is removed, although the precise mechanism of the mutation is still to be verified.

Following the results from Chapters 3 & 4 it is clear that there are potentially microscopic phenomena in the bijel which result in macroscopic aging and/or a determination of macroscopic structural properties. To investigate further, we use diffusing-wave spectroscopy (a form of light scattering) to probe the microscopic dynamics of the interfacial particles and/or the particle-laden liquid-liquid (L-L) interface. We find that bijel dynamics show two-step (fast/slow) decay behaviour, with the dynamics slowing as the system ages. The two-step decay is very similar to that observed in colloidal gels formed by diffusion-limited cluster aggregation (DLCA), with the initial (fast) decay due to thermally-activated modes of the gel network, and the later (slow) decay due to the relaxation of internal stresses induced by gel syneresis. For a bijel, the internal stresses could be due to syneresis, but could also be due to the jamming transition and/or the monogelation process and/or the forces acting on the L-L interface by the particle layer. In terms of the aging, if the system does not form a monogel, the correlation functions can be (almost) rescaled on to a master curve, indicating the property of universal aging.

If the system does monogel, the functions cannot be superimposed, implicating the monogelation process as a potential cause for a different kind of aging in this system.

Due to the interesting differences found when changing the size of the stabilizing particles in a bijel, in Chapter 6 we combine large and small particles (making 'bimodal' bijels) and look for evidence of particle segregation by size, quantitatively estimate the ratio of particle uptake fractions and measure kinetics. Larger particles are found to adsorb to the interface in twice the quantity as smaller particles, and we find evidence to suggest the preference of larger particles for interfaces curved in only one direction, corroborating results from previous Chapters. Bimodal bijels take longer to jam than an equivalent monomodal (standard) bijel, which is backed up by simulations and highlights the increased ability of the bimodal particles to reorganise at the interface before arriving at the jammed metastable state. Finally, we also observe that the lengthscale of a bimodal bijel can heavily depend on the quench rate used during the preparation, suggesting that quench rate could be used (as well as particle size, volume fraction and contact angle) as a lengthscale control parameter.

This thesis adds to the bijel literature, building on previous experimental studies and verifying/contradicting simulations. Particle size is shown to be a pivotal parameter for bijel formation in the W/L system, with particles of size $r = 63$ nm proving more versatile (markedly less sensitive to quench rate) than particles of size $r \approx 300$ nm. However, even-smaller particles (of the same type) do not provide any additional advantage. We also show how the particle size can not only control bijel porosity (according to $L \propto r/\phi$ as predicted by simulations) but can control bijel topology (smaller particles result in structures with greater hyperbolic character). By monitoring the bijel structure over time (topology and dynamics) we have shown that the bijel (in some cases) continues to age for at least c. 1 hr (topology) and in all cases c. 1 day (dynamics). For the first time experimentally, we have used a bimodal dispersion of particles to stabilize a W/L bijel and have uncovered a potentially useful new way to produce samples with different porosities from the same starting mixture, by changing the quench rate. The knowledge of the interplay between particle size and quench rate along with the effect on bijel topology will both assist in the scaling up of processes for industrial-level production and inform future strategies for tailoring the structure for specific applications.

Future research should focus on several remaining open questions. The volume

fraction of $r = 63$ nm particles in the W/L system should be increased towards 10% and sonication procedures improved to allow good redispersion to test the lower bound of L, which we expect to be around 1 μm. Also, a new W/L fabrication paradigm should be devised which uses sterically-stabilized particles, to continue the reduction of r towards the value used in simulations (5 nm) in order to test the fundamental physics of bijel formation, specifically what value of interfacial attachment energy is needed for long-term stability. Bijel dynamics can be further probed by using a technique which allows a variation in the probe lengthscale (e.g. differential dynamic microscopy, DDM), as well as developing a better theoretical model for (multiple) light scattering in a bijel system to arrive at the mechanisms responsible for the anomalous aging, and compare to the predictions of monogelation. Finally, higher magnification/resolution microscopy should be used to look for particle segregation on the liquid-liquid interface (as seen in simulations) and to identify in real-space the locations of the changes in Gaussian curvature over time as measured in Chapter 4.

Lay Summary

Soft materials exist in abundance throughout the home and are used in many industrial settings. A soft material (as opposed to a hard material) is any material which displays properties somewhere between a pure liquid and a pure solid. Toothpaste for example displays liquid properties when being squeezed out of its tube, but solid properties when sitting on the toothbrush. Other examples include ice cream, rubber and paint.

This thesis concerns itself with a novel soft material called the bijel which consists of two different liquids (water and an oil) and small solid particles (smaller than the width of a human hair), which forms a sponge-like structure. The water and oil are separated by a layer of said particles into interpenetrating regions with a characteristic size. The size of the regions (domains), unlike the particles, are larger than the width of a human hair but still too small to be seen by eye. The bijel potentially lends itself for use in a variety of industrial applications including biological tissue engineering, materials for energy storage and vessels for chemical reactions.

Bijels can readily be prepared in the laboratory, but the effect of various design parameters (e.g. the size of the particles, the speed of the preparation) on the final structure of the bijel are ill understood. To aid the development of the bijel for applications, and to gain further understanding about the physics of the system, we prepared bijels with a range of particle sizes and preparation speeds and characterized the structures in various ways.

We found that bijel production is less prone to failure when we use particles smaller than that traditionally used to stabilize bijels, and have developed a new theoretical framework to take account of this. This will allow, in future, for the preparation of bijels with smaller domain sizes, and expand its applicability. However, we identified a practical limit to our approach, meaning that to use

even smaller particles a new methodology will be required.

To shed more light on the small changes which result when different particles sizes and speeds of preparation are used, we measured and characterized bijel shape. Again, this work will allow, in future, better tuning of the structure for specific purposes for example, a more open sponge structure is created when smaller particles and faster speeds are used, which would be preferable if wanting to flow material through the structure. We also observed that the structure continues to change (mutate) slowly if large particles are used, suggesting some kind of aging phenomenon.

To investigate how bijels age, we used a laser to measure very small movements of the particles in the bijel structure. We found that the particle movement slows down as the bijel ages in a similar fashion to other soft matter systems, but that there were some differences. Depending on the type of particles, the movement slowed down more quickly or less quickly. This has provided the first insight into the nature of the particle interactions in the bijel.

We rounded off our investigation of bijels by using small *and* large particles together. We found that the size of the domains can (under certain conditions) be controlled by the speed of preparation, which offers a new way to control the structure of bijels. In addition, we observed competitive behaviour between the small and large particles, further enhancing our understanding of the physics of bijels.

Declaration

I declare that this thesis was composed by myself, that the work contained herein is my own except where explicitly stated otherwise in the text, and that this work has not been submitted for any other degree or professional qualification except as specified.

Chapter 3 along with Appendix A form the basis for Ref. [1] and Chapter 4 along with Appendix B forms the basis for Ref. [2].

(*Matthew Reeves, 2016*)

Acknowledgements

Many thanks, first and foremost, to my supervisor Job Thijssen, for the expert instruction, guidance and wisdom received over the past few years which I am incredibly grateful for. Thanks also to my second supervisor, Paul Clegg, for advice and support throughout this process.

Thanks to Joe Tavacoli for helping me with the diffusing-wave spectroscopy project, and Andy Schofield for the provision of colloids big and small.

Thanks to Mike Cates, Michiel Hermes, Cait MacPhee, Simon Titmuss and Davide Marrenduzzo for useful discussions over the course.

Thanks to Katherine Rumble for the preparation of the nitromethane/ethanediol bijels used in Chapters 4 & 5.

Thanks to Kevin Stratford for providing bijel simulation data and useful discussions.

And finally, love and thanks to Lauren, for all your support.

Contents

List of Figures

List of Tables

Chapter 1

Introduction

1.1 Overview

Particle-stabilized bicontinuous emulsions are studied as part of the wider field of soft matter, which concerns itself with physical systems displaying both liquid-like and solid-like properties, depending on their environment [12]. Such systems form the basis of materials which exist in abundance around the home, in factories, and in nature, and we rely heavily on them in our daily lives, e.g. polymers [13], lipid membranes [14] and composite materials [15]. Although the field is broad, there are some unifying concepts, such as the mesoscopic length scales which allow quantum effects to be ignored, but emphasizes the importance of thermal motion. Some soft matter systems exist in a state far from thermodynamic equilibrium [16], enhancing the richness in their behaviour. One such class of system is the emulsion [17], where two otherwise immiscible liquids are blended together to create a metastable mixture. Everyday examples include mayonnaise, milk, and paint.

The phenomenon of emulsification has been well documented over the past couple of centuries, with many material washing and food preparation techniques utilizing molecular emulsifiers [18]. At the beginning of the 20^{th} century however, an alternative method of emulsification was discovered. Pickering and Ramsden reported that emulsification could take place without soluble emulsifiers, but with insoluble solid particles, which attach at the interface [19, 20]. This initial discovery opened up a brand new area of emulsion research,

which has seen increased activity during the past 10-20 years, owing to the advancement of a related area of research into colloidal particles [4, 21]. Particle stabilized emulsions, or Pickering emulsions, have many technological applications including, but not limited to, materials templating [22] and the fabrication of controlled-release mechanisms [23]. Some have suggested that such systems should be referred to as Pickering-Ramsden emulsions to acknowledge the work of both seminal authors of the field [24], but here we stick with the convention adopted in the literature.

Very recently, the field has been expanded to include bicontinuous emulsions, nicknamed 'bijels', whereby two liquids are stabilized by solid particles into fluid bicontinuous interlocking channels [3]. This new class of soft material further enhances the technological applicability of emulsions to include microfluidics [25], gas storage [26], catalysis [27] and fuel cells [28]. This bijel field is relatively young, with much of the fundamental physics yet to be fully explored experimentally. The remainder of **Chapter 1** is dedicated to outlining the theoretical and experimental background of the bijel field.

The subsequent Chapters are arranged as follows. In **Chapter 2** we outline the materials and experimental methods used throughout this thesis while addressing some other relevant theoretical concepts. In **Chapter 3** we use nanoparticles instead of microparticles to stabilize water/lutidine bijels. We measure and analyze the bijel lengthscale dependence on particle volume fraction, examine the kinetics of bijel formation while exploring the effect of quench rate and report broadly on the similarities and differences. We end with a new theoretical framework for understanding the role of bending moduli in bijel formation. In **Chapter 4** we quantitatively characterize bijel morphology by measuring distributions of interfacial curvatures and explore the effect of particle size, quench rate, and time after bijel formation. We find that the most hyperbolic structures are formed when the smallest particles and fastest quench rates are used. The analysis opens up new avenues for choosing/controlling bijel microstructure beyond the simple characteristic length scaling relationship. In **Chapter 5** we study bijel dynamics with diffusing-wave spectroscopy, a type of light scattering. We uncover interesting aging behaviour across three bijel systems and discuss the potential origins. In **Chapter 6** we make bijels with both nanoparticles and microparticles simultaneously. We make carefully prepared specifications of samples to directly measure the relative interfacial uptake fractions of the particles. We observe that in a bidisperse system the bijel lengthscale can depend

heavily on the quench rate used, that the bidisperse bijel jams slower than a monodisperse bijel, and that the microparticles prefer to reside around droplets. In **Chapter 7** we summarize and discuss the main results of this thesis in the context of previous knowledge and identify potential avenues for future work. We finish the thesis with the conclusions in **Chapter 8**.

1.2 Emulsions

Two non-identical liquids in contact will be miscible, immiscible or partially miscible in varying proportions depending on thermodynamic conditions. Typically, a small amount of one liquid will be soluble in another, but as more is added this becomes thermodynamically unfeasible unless the temperature is raised or lowered (depending on specific interactions of the liquid molecules). At fixed temperature, a mixing or demixing event can be also be triggered by a change in pressure. This leads to combinations of liquid-liquid ratios and temperatures (or pressures) for which the system will exist as one phase (mixed) or two phases in coexistence (demixed) [12]. For a system in the demixed regime there is an increase in free energy associated with the interfacial area between the two phases, quantified as

$$\Delta G = \gamma A \tag{1.1}$$

where γ is the interfacial free energy per unit area (or interfacial tension) and A the interfacial area. It follows that a system in the demixed regime will spontaneously reduce its interfacial area to minimize the free energy (this is most obvious when observing that a dispersed phase will usually exist as spherical droplets, a sphere having the lowest 3D surface to volume ratio). This means that the emulsion will undergo coarsening processes, such as coalescence, Ostwald ripening and creaming or sedimentation, as depicted in Figure 1.1.

The first, coalescence, is the process by which two droplets of dispersed phase combine and result in a single droplet, thereby decreasing the ratio of surface area to volume, and hence decreasing the free energy. The second, Ostwald ripening, is the process by which large droplets of dispersed phase grow at the expense of small ones nearby, without actually coming into contact and coalescing. This is driven by a difference in Laplace pressure between the big and small droplet – the pressure is higher in the smaller droplet. Creaming or sedimentation of droplets is driven by the density difference (if any) between the dispersed and continuous

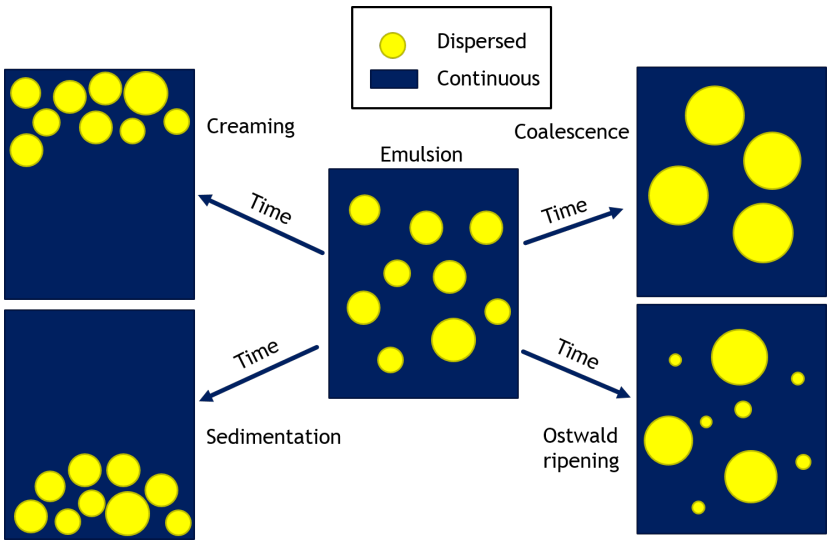

Figure 1.1: A schematic of the coarsening processes an emulsion will undergo (see text for explanations).

phases. If the droplets have a lower density, they will rise (creaming), whereas if they have a higher density, they will sink (sedimentation).

To emulsify two liquids in the demixed regime it is therefore necessary to halt or at least dramatically curtail these processes. The tendency to coalesce and Ostwald ripen can be reduced either by reducing γ (using molecular surfactants [29] or proteins [30]) or by reducing A (using colloidal particles which adhere to the interface, see next section). Sedimentation or creaming can be curtailed by, say, increasing the viscosity of the continuous phase, providing a greater resistance to the movement of dispersed droplets.

The typical morphology of an emulsion is droplet-matrix – that is, droplets of one phase dispersed in a continuous (second) phase. In addition, a typical emulsion system will be out-of-equilibrium thermodynamically, meaning that energy must be put in to emulsify, and the direction of spontaneous change is towards complete phase separation. However, there are emulsions stabilized by surfactant which form spontaneously, i.e. equilibrium emulsions, the so-called 'microemulsions' [31]. Microemulsions find applications in drug delivery [32, 33], the production of catalytic materials [34] and nanoparticles/quantum dots [35]. Morphologically these systems can be similar to bijels (the subject of this thesis), however the lengthscales tend to be around 100 nm (or less) and the structures are not arrested in nature (i.e. are equilibrium, as opposed to non-equilibrium, structures). As shall become clear later, ideally we would like to prepare bijels with lengthscales around 100 nm in the laboratory but this has not been achieved (yet). If and when

this is achieved, it would be interesting to compare the structures formed with microemulsions to identify potential advantages for applications. One of which could be the greater resistance of the bijel structure to external perturbation because of its significant yield stress [36].

We now move on to a discussion of phase separation mechanisms which is crucial for understanding bijel formation – a bijel is formed when the spinodal decomposition of a binary mixture of liquids is arrested by a layer of interfacial colloids.

1.3 Liquid-liquid demixing

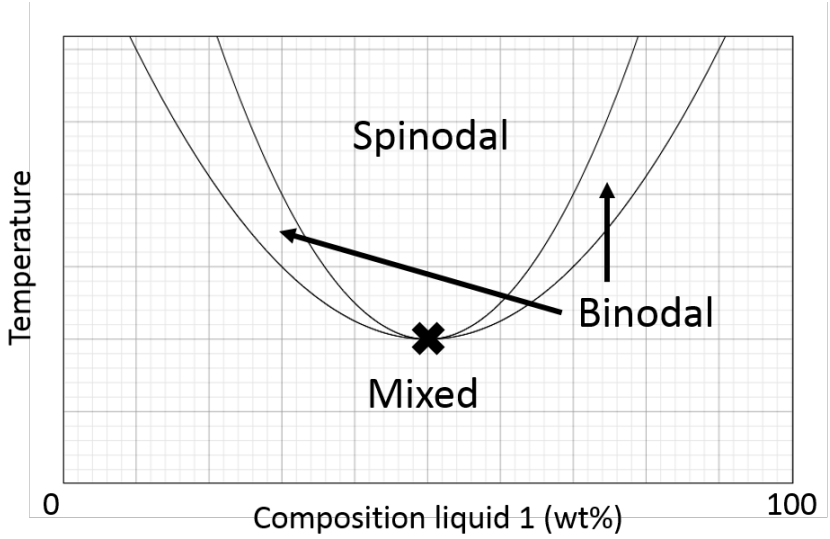

Figure 1.2: A schematic showing a typical binary liquid phase diagram with a lower critical solution temperature (LCST) marked by the cross.

Emulsions can be prepared by agitating a mixture of two immiscible or partly-miscible liquids at a temperature, pressure and composition which corresponds to a point in the phase diagram in the demixed regime. However, an alternative method exists, which makes use of a temperature, pressure or compositional quench (a change from one value to another). A typical binary liquid will have two phase-separation regimes, characterized by the position of the binodal and spinodal lines [12]. In the binodal region, the first derivative of free energy with respect to composition is negative, but the second derivative is positive, which leads to spontaneous nucleation of droplets with only the droplets exceeding a certain size surviving. In the spinodal region, the second derivative of free energy

with respect to composition is negative, meaning that the system is unstable to any fluctuation in composition, and the spontaneous phase separation proceeds unimpeded.

Figure 1.2 shows a typical binary liquid phase diagram with a lower critical solution temperature (LCST) i.e. a mixture which is demixed by heating. If the system is in the area below the binodal line, all mixtures exist as a single phase and are stable. If the system is in between the binodal and spinodal lines, it is metastable, in that thermal fluctuations in composition will nucleate droplets, but only those droplets over a certain size will survive and grow, leading to phase separation (the 'nucleation and growth' regime). The free energy of such a system is given by [12]

$$\Delta G = \frac{4}{3}\pi r^3 \Delta G_{\text{bulk}} + 4\pi r^2 \Delta G_{\text{interfacial}} \tag{1.2}$$

where ΔG_{bulk} and $\Delta G_{\text{interfacial}}$ are the bulk and interfacial free energies and r is the radius of the nucleated droplet. The energy barrier to be overcome is given by

$$\frac{\mathrm{d}\Delta G(r^*)}{\mathrm{d}r} = \frac{16\pi \Delta G^3_{\text{interfacial}}}{3\Delta G^2_{\text{bulk}}} \tag{1.3}$$

where

$$r^* = \frac{-2\Delta G_{\text{interfacial}}}{\Delta G_{\text{bulk}}} \tag{1.4}$$

is the critical nucleus size.

In the spinodal region, the system is unstable to even the smallest fluctuation in local composition, and spinodal decomposition will occur (original observation and understanding developed by Cahn [37, 38] and Hilliard [39]). In this regime, the free energy per unit volume F is given by [12]

$$F = A \int \left[f_0(\phi) + \kappa \left(\frac{\mathrm{d}\phi}{\mathrm{d}x} \right) \right] \tag{1.5}$$

where $f_0(\phi)$ is the free energy per unit volume of a uniform mixture of composition ϕ, κ is the gradient energy coefficient and x is a spatial coordinate. It is this spinodal composition which is arrested in the case of the bijel, so we will elaborate further on this phenomenon.

Upon entering the spinodal region, an initial interdiffusion of liquid molecules sets up distinguishable domains with a well-defined interface between them [12]. This process can be thought of as a superposition of sinusoidal composition fluctuations each with a certain amplification factor [37]. The domain size L (or sinusoid with

wavelength $2L$) which is most amplified by this process is the one which balances the diffusivity of the molecules with the amount of interfacial area produced. In other words, there are two competing factors – the system wants large domains to reduce interfacial area (and hence free energy) but is limited by the ability of the molecules to diffuse over long distances. With the domains established, the interfacial tension drives liquid movement over distances greater than the domain size, growing the domains and coarsening the structure. In this second regime, the 'viscous-hydrodynamic regime', L grows linearly with time. Then, as the domains become larger and more massive, inertial forces begin to dominate, and L grows as $t^{2/3}$ [40]. Further detail of phase separation mechanisms can be found in Ref. [41].

1.4 Particle-stabilized emulsions

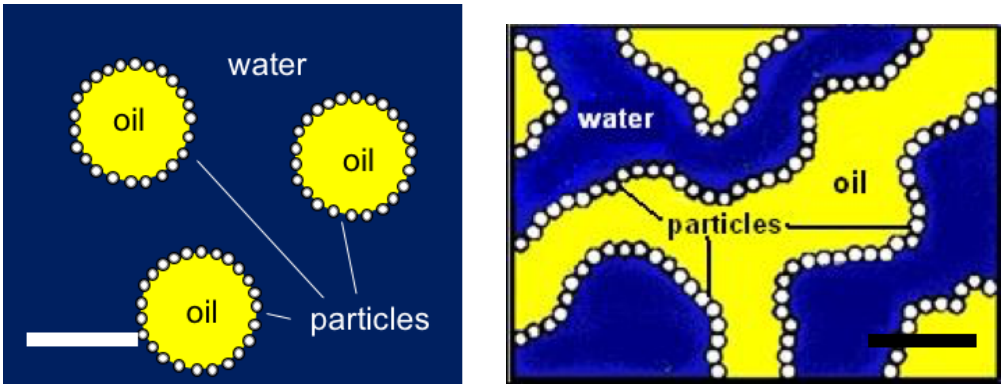

(a) (b)

Figure 1.3: (a) A schematic depicting an oil-in-water Pickering emulsion. The particles are adsorbed at the interface, offering resistance to coalescence. (b) A schematic depicting a bijel with two coexisting bicontinuous domains of oil and water. The particles are adsorbed at the interface and prevent further coarsening of the structure, locking it in place. Graphic adapted from Ref. [3]. Scale bars: $\approx$ 50 μm.

Instead of relying on molecular surfactants, colloidal particles of radius r with intermediate wettability for both liquids can become irreversibly adsorbed to the interface [24] (see Figure 1.3(a)), reducing the liquid-liquid (L-L) area by (at maximum) a disc of radius r. The amount of area reduction is determined by the three-phase contact angle θ, with the maximum reduction at $\theta = 90°$. The contact angle is generally measured through the aqueous phase, so a hydrophilic particle

will have $0^\circ < \theta < 90^\circ$ and a hydrophobic one $90^\circ < \theta < 180^\circ$ (see Figure 1.4). The particle's hydrophilicity is usually the main factor in determining which phase is dispersed and which one is continuous – however, with $\theta \approx 90^\circ$, the continuous phase will usually be the one which is in excess by volume[4].

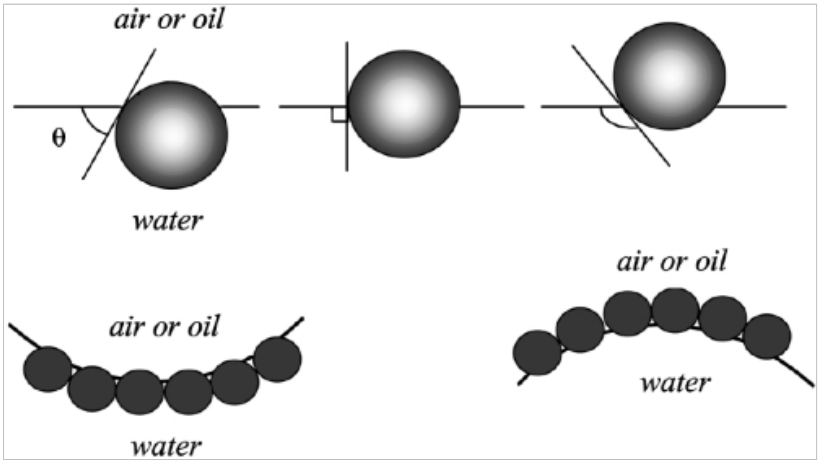

Figure 1.4: A schematic illustrating the particle contact angle and its influence over the type of emulsion formed. Graphic from Ref. [4].

The total attachment energy of a particle is given as [24]

$$E = \pi r^2 \gamma (1 - |\cos\theta|)^2 \tag{1.6}$$

The magnitude of this energy is generally on the order of $\approx 1000\ k_\mathrm{b}T$ for micron-sized particles and typical binary liquid interfacial tensions [8, 42], in effect resulting in an irreversible adsorption process. This situation differs from that of molecular surfactants which adsorb reversibly with energies of $\approx k_\mathrm{b}T$. Again, the energy is maximum for $\theta = 90^\circ$.

In this respect, colloidal particles can emulsify liquids by directly reducing the free energy. They also combat the destabilization mechanisms the emulsions undergo – coalescence, creaming and Ostwald ripening [4]. Coalescence is inhibited by the coating of particles on the surface of the droplets, in effect keeping the droplets from coming into close contact. The same coating hinders Ostwald ripening, which is the tendency for large droplets to grow at the expense of smaller ones due to the larger Laplace pressure in smaller droplets. Shrinking a droplet would require the expulsion of interfacial particles which is energetically unfavourable, hence providing an energy barrier for this process. Creaming, i.e. the moving apart of the phases because of differences in density, can be slowed by droplet-bridging through the continuous phase (which acts to increase its viscosity) and

either slowed or hastened due to the weight of the particles on the droplets.

There are two routes to Pickering emulsion formation – shearing two immiscible liquids in the presence of appropriate colloidal particles, or quenching a binary liquid into the de-mixed regime from the mixed [43]. In the latter case, reducing or increasing the temperature rapidly will force the system to phase-separate by either droplet nucleation and growth or spinodal decomposition [12]. The former will create a Pickering emulsion, and the latter will, if other conditions are satisfied, produce a bijel.

Large scale computer simulations reported in 2005 [5] explored the possibility of arresting the spinodal decomposition of a binary liquid in the presence of colloidal particles. The results suggested the existence of a kinetic pathway to the creation of amorphous soft solid materials, nicknamed 'bijels' (Bicontinuous Interfacially-Jammed Emulsion geLS). Similar to the formation of Pickering emulsions via phase separation, the final structure is representative of the separation kinetics, in this case with convoluted interconnected domains stabilized by nano- or micro-particles with a characteristic lengthscale (see Figure 1.3(b)). An overview of the simulation and experimental bijel studies is presented over the next two sections.

1.5 Bijels in simulations

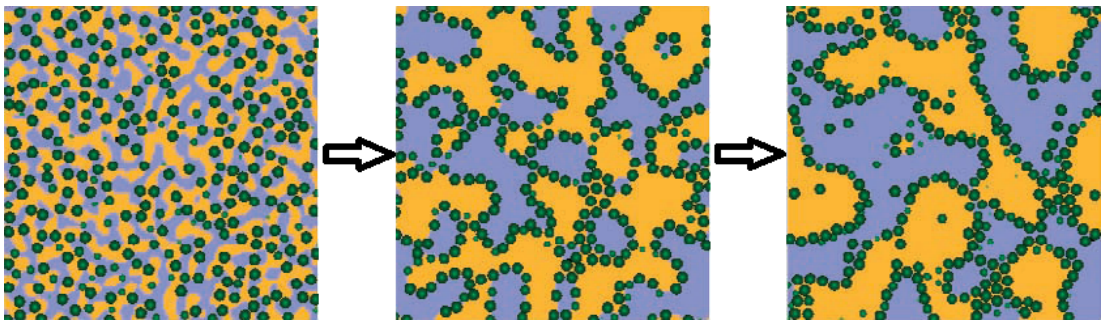

Figure 1.5: The simulated evolution of two coexisting liquids (blue/yellow) with dispersed colloids (green) at a volume fraction of 20% undergoing spinodal decomposition, according to Ref. [5].

The first bijel simulations were reported in 2005 [5], and since then many more have been performed in order to better understand various aspects of the formation and long-term behaviour of the structure [11, 44–49].

A typical bijel preparation scheme in simulation is as follows. A binary solvent,

with roughly equal volume fraction of liquids, whilst also containing neutrally-wetting colloidal particles of radius $r \approx 5$ nm, is quenched deep into the two-phase region of the phase diagram which induces spinodal decomposition. The requirement that the phase diagram be close to symmetric is so that neither phase, upon demixing, is favoured to be the continuous phase [5], although simulations using asymmetric liquid volumes still result in bijels [2]. In the case without particles, after the initial interdiffusion of liquid molecules A and B (which sets up the well-defined bicontinuous domains separated by a sharp interface), the average domain size grows as $L(t) \sim t$ in the 'viscous-hydrodynamic' regime, driven by a reduction in the interfacial free energy due to the reduction of L-L interfacial area (Figure 1.5) [50]. Later, as the domains increase above a certain size, a crossover is observed to the 'inertial' regime, which has $L(t) \sim t^{2/3}$. However, in the presence of neutrally-wetting particles, the particles sequester to the interface during the viscous-hydrodynamic coarsening. A jamming transition of the colloids takes place as their concentration on the L-L interface saturates, and a close packed monolayer is formed which dramatically curtails the coarsening [5]. The characteristic lengthscale of the bijel at the point of saturation scales as $L \propto r/\phi$, where r is the radius and ϕ the volume fraction of the colloids. Note that the particle contact angle does have a small effect on the final saturation lengthscale [48].

The non-equilibrium arrested nature of the resultant colloidal monolayer gives the bijel some unique and potentially useful properties. As well as a tunable pore size L, it should also have a tunable elasticity. The elastic modulus is predicted to scale with the interfacial energy density γ/L, or $\gamma\phi/r$. Structural stability of the bijel structure could be further enhanced by the attractive interactions between the colloids. The bijel could be used as a micro-reaction crossflow medium, since the structure would have high permeability to either of its component solvents and any reagents dissolved in them (i.e. at the interstices of the particle layer). Macroscopically, the structure should also be able to support the alternating flow of fluids [5]. In this respect, its permeability as a function of geometry has been quantitatively assessed and the bicontinuous morphology has been found to be superior to more traditional 'filled-pore' morphologies [51]. The principles of emulsion templating [22, 52, 53] are transferable to bijels, with the potential for the creation of (solid) bicontinuous macroporous materials [51, 54], with potential applications in gas storage [26], catalysis [27], fuel cells [28] and solar cells [55]. The colloidal skeleton could even be used for tissue engineering [56], or filtration [57].

Several aspects of bijel formation and behaviour have been investigated by the original and subsequent simulations. For example, the original lattice-Boltzmann simulations broached the question of the structure's long-term fate – due to the parameters and machinery used, the simulations barely exceeded the Brownian time of the particles, making it difficult to ascertain whether or not coarsening would continue indefinitely [5].

The system was also modified to include bimodal, instead of monomodal, particles. This was done to remove the opportunity for particle crystallisation at the interface, a possible mechanism for providing long term stability. $L(t)$ levels off slower than the equivalent monodisperse case, but still ends in a plateau which, due to the limited run times, cannot definitively say whether a bidisperse bijel will be stable on laboratory timescales. To investigate further, the simulations looked at the evolution of two specific geometrical motifs characteristic of the bicontinuous structure, namely a cylindrical fluid 'neck', and a rippled surface. Without particles, the first would be expected to break into droplets due to the Rayleigh-plateau instability, and the second would be smoothed out due to interfacial tension. However, with a dense layer of bidisperse particles, both motifs were arrested very close to their initial configuration, providing evidence for the long-term stability of such a bicontinuous structure.

If the bijel was to coarsen beyond the lengthscale at which the jamming transition occurs, particles would need to be expelled. Very little particle expulsion was observed however and the phase separation was almost, but not completely, arrested. This has also been seen in simulations with slightly modified parameters allowing the system to evolve 50% beyond the Brownian time [11]. If we consider neutrally wetting particles ($\theta = 90°$) which maximizes the attachment energy, for particles with $r = 5$ nm the energy is easily of the order 10 $k_{\mathrm{b}}T$, rendering individual expulsion unlikely [11], and even less likely for larger particles or higher interfacial tensions. Indeed, if the particle attachment energy is not high enough, the system completely phase separates, mediated by the desorption of particles from the interface [58]. A complete saturation of $L(t)$ has been observed but only when thermal motion of the colloids was not included in the simulation model [45], suggesting that colloidal Brownian motion could be the cause of the late-time dynamics. However, simulations using a continuum (rather than lattice-Boltzmann) approach, with Brownian effects included, also observed complete cessation [46]. Hence, simulations are inconclusive on this issue.

Another possible mechanism for the destabilization of bijels arises out of collective

effects, as observed in experiments for a Pickering drop under gravity [59]. A 'keystone' particle at the base of the drop is ejected if the total weight of particles above it is larger than the binding force of said particle. A similar mechanism is not ruled out for bijels [5], but has not been observed in either experiments or simulations.

Other aspects explored include the effect of the contact angle θ, concentration ϕ and phase volume parameter φ (i.e. the ratio of the volumes of coexisting phases) on the resultant structure (discrete Pickering emulsion or bijel). Although there is a rough requirement for bijels that the colloids be neutrally wetting and that φ be roughly 1:1 [5], these requirements have been subsequently found to be interdependent [45]. For $\varphi = 1{:}1$, contact angles of 90 $\pm 10^\circ$ produce bicontinuous structures. At fixed φ the range of successful θ is controlled by the concentration of particles – the range is increased upon an increase in ϕ, i.e. the requirement of $\theta = 90^\circ$ becomes less important when more particles are used. At fixed ϕ, when one liquid is added to decrease φ below 1:1, the particles must increasingly prefer the minority phase in order to maintain a bijel. If not, a Pickering emulsion is formed instead. In general, a contact angle of 90° can support bijel formation up to $\varphi = 5{:}9$.

A similar analysis has been performed on bijels stabilized by anisotropic particles, specifically ellipsoids [47]. In that case, a contact angle of 90° can support bijel formation up to a ratio of 5:9, which increases to 3:4 for a contact angle of 130°. The ellipsoids also proved more efficient stabilizers than spheres, i.e. each ellipsoid took up a larger area of L-L interface compared with a sphere of the same volume [47]. 3D packing of ellipsoids have also been investigated and at certain aspect ratios can pack more densely than the equivalent spheres [60]. 2D bijel simulations looked at the role of Laplace pressure in determining the equilibrium properties of adsorbed anisotropic particles (including stars, ellipsoids and assorted platelets), as well as the effect of interfacial jamming on the shape of L-L interface [61]. Isolated particles adsorbed to Pickering drops were found not to alter the homogeneous equilibrium curvature of the L-L interface, however a jammed layer of ellipsoids was found to alter the shape of the bicontinuous L-L interface. In the jammed bicontinuous case, the Laplace pressure vanishes as the interparticle repulsion balances the L-L interfacial tension.

Simulations have also looked at what happens when the spherical interfacial colloids are magnetic with permanent dipoles [44]. The creation of a monodomain of aligned magnetic moments, preferred by the dipolar interaction between the

colloids, is unable to form due to the curvature of the L-L interface, which creates frustration. For typical parameters, the bijel morphology is still determined by the balance between short range repulsive interaction and capillary forces, as in the non-magnetic case, although the magnetic interaction has the potential to affect the domain morphology. For example, applying a strong (≈ 0.6 T) uniform external magnetic field creates significant anisotropy in the bijel domains along the axis of the field (similar anisotropy can be introduced by using a centrifugal field [62], see next section). The extent of anisotropy depends on whether or not the field was turned on during the phase separation or after the jamming transition. This process could potentially turn the bijel into a droplet morphology, which would be useful for applications in a similar way to the controllable stability of Pickering emulsions as demonstrated in experiments [63], although this was not achieved in the simulations. However, in principle the same function could be achieved via the use of field gradients which exert forces on the particles (instead of torques in the case of a uniform field).

Finally, the most recent simulations have looked at the case of bijel formation when the spinodal decomposition is surface-directed (SDSD) [49]. Bijel formation was simulated in thin films, with both major surfaces preferentially wetted by one of the liquids. Without particles, the surface-wetting has a large effect on the morphology of the spinodal decomposition. The bicontinuous domains turn into cylindrical domains connecting the upper and lower surfaces. With particles, the resultant structure is dependent on the volume fraction of particles and the film thickness. At high volume fractions and large thicknesses, bicontinuous morphologies are found. Reducing the thickness and/or volume fraction makes it more likely for a discrete (droplet emulsion) morphology to be formed. Compared to SDSD itself, the particles extended the range of film thicknesses that could support the cylindrical domains, while stabilizing bijel structures at higher volume fractions.

1.6 Bijels in experiments

1.6.1 Systems

Bijels have been prepared in the laboratory in a variety of different forms (systems) since the reports of the first simulations [64]. The route to the

experimental realization of bijels involved a) the identification of appropriate binary liquids which meet the symmetric phase diagram requirement, b) the identification of an appropriate colloid with $\theta = 90^\circ$ and c) the development of reproducible protocols. Stöber silica [65] has been the colloid of choice so far, due to its low polydispersity [66] and highly tunable surface properties [67]. Stöber silica will not in general have $\theta = 90^\circ$ for any pair of liquids, but for some specific pairs it is possible to chemically modify the surface to achieve it. The first reported bijel was made using a system of water and lutidine (W/L, 2,6-dimethylpyridine) [6]. To access spinodal decomposition, the system was prepared at a critical composition at room temperature and quenched up moderately fast (17°C/min) through the critical point, as opposed to quenching fast through the nucleation and growth region, an alternative method explored in other work [43]. Stöber silica of radius $r = 290$ nm was subject to a drying protocol to achieve

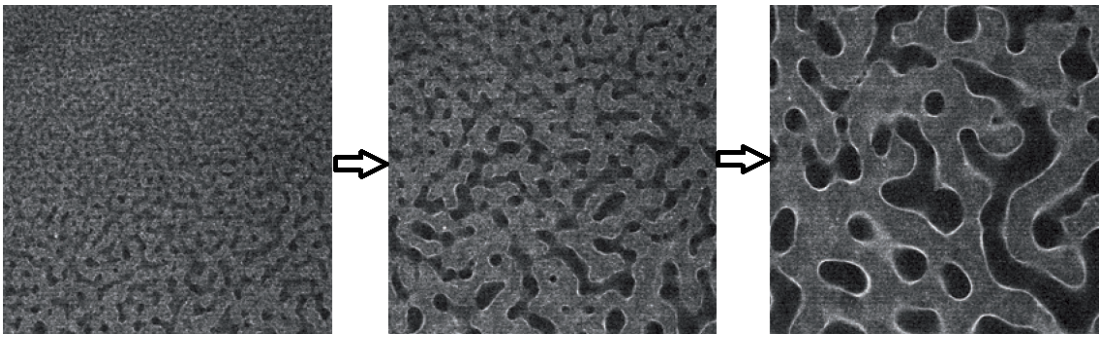

Figure 1.6: Confocal micrographs of W/L bijel formation after the initiation of spinodal decomposition by an experimental temperature quench (17°C/min), as reported in Ref. [6]. The fluorescence signal (white) comes from the particles. Left to right is increasing in time. The behaviour is reminiscent of the coarsening behaviour predicted by the simulations in Figure 1.5.

neutral wetting [68] and loaded into the mixture at 2% volume fraction, producing a pore size L of about 40 μm. L was found to scale linearly with $1/\phi$, with some deviation at low volume fractions (higher pore sizes, perhaps suggesting an upper limit). Overall, the relationship was in agreement with simulations, as was the observed phase-separation and coarsening behaviour (Figure 1.6). High resolution confocal microscopy showed an interfacial particle monolayer, suggesting that the bicontinuous structure was indeed formed due to interfacial tension and not particle-particle interactions. Samples were stable for several months, although small local particle rearrangements could not be ruled out. The bijel's mechanical strength was also probed, and the structure exhibited a small but significant yield stress as well as elastic self-healing properties.

However, one of the big experimental difficulties for W/L bijel production is the tuning of the silica surface chemistry. The interaction of W/L mixtures and silica surfaces is complex [69–71]. Native silica particles are hydrophilic [72], but on approach to spinodal decomposition they are 'pre-wetted' by the lutidine (acquire a layer of lutidine) and become, in effect, hydrophobic [73]. This renders them unable to stabilize bijels, as they will simply partition to the lutidine-rich phase and likely aggregate. This problem was overcome by the inclusion of the dye FITC, but on closer inspection it was found that it is highly likely the agent responsible for this inhibition is not the dye molecule itself, but the linking molecule APS which is added in excess, leaving many amine groups exposed on the surface [68, 69]. This, combined with the surface silanols (Si-OH), provides an interesting interplay between protonation and deprotonation sites when the particles are dispersed in de-ionised water. Surface charge measurements show that upon addition of APS/dye mixtures the surface charge is made more positive, and even more so upon drying [69]. The surface charge of dried particles will actually decrease over time upon dispersion in water. This can be correlated with the experimental observation of the particles increasingly preferring the lutidine phase over time after dispersion [69]. During the previous work on W/L bijels the amount of added APS was not accurately controlled, which created wetting discrepancies between the batches of Stöber silica. Introducing such control in future work seems to be a necessary step.

W/L bijels have also been stabilized by graphene-oxide (GO) sheets, providing a simple route to the production of graphene oxide frameworks [74]. Such frameworks could be used in biosensors or supercapacitors. After stabilizing domain sizes of between 10 and 100 μm, the water and lutidine were removed by freeze-drying, leaving behind a porous GO foam. Unlike the W/L bijel stabilized by silica spheres, the curtailment of the spinodal decomposition was attributed to the elastic nature of the GO-laden interface rather than a jamming transition.

After the seminal work on W/L bijels, a system of nitromethane and ethanediol (NM/ED) was successfully used to create a bijel, again using Stöber silica, but in this case the particles were modified via a silanization reaction to achieve neutral wetting [36]. Domain sizes of around 1 μm were achieved with a particle radius of $r = 67$ nm and volume fraction of 11.5%, significantly less than that previously achieved with W/L [6]. NM/ED, when prepared at critical composition, has a volume ratio (between the two coexisting phases) of 52:48, which is more symmetric than the W/L system at 69:31. Also, the NM/ED system is less

subject to creaming effects as the densities of the coexisting phases are more closely matched. The lower critical solution temperature of 40°C means that the bijels formed are stable at room temperature which allows more rigorous rheological measurements to be taken. It was shown that the domains align under shear and that the structure restores itself after compression.

The NM/ED system has also been used to create so-called 'bridged' bijels [75], which result if only a small number of particles initially adsorb to the spinodal interface, with the remaining particles adsorbing to droplets which nucleate in the ED phase due to the finite temperature quench [76]. This microstructure leads to much larger domain sizes (compared with a normal bijel at the same volume fraction) of up to 450 μm, which is the size typically sought for tissue engineering purposes [56].

Not only have NM/ED bijels been prepared with silica spheres, but also by silica rods [77]. Rods proved to be more efficient stabilizers of the spinodal interface, meaning that for the same volume fraction and volume-per-particle of rods vs spheres, the rods stabilized a bijel with smaller domains. The rods would be even more efficient if it wasn't for 'flippers', which flip out of the plane of the interface and hence occupy less interfacial area, and the tendency of the rods to form stacked layers. The overall morphology of the domains stabilized by rods vs spheres were broadly similar, apart from the ability of the rods to stabilize thinner liquid necks, purportedly due to the ability of the rods to align.

Experimental protocols have recently been devised which allow the preparation of polymeric ethylene carbonate and p-Xylene bijels with the use of commercially available (i.e. 'out of the box') silica particles, by combining particles of different wetting properties [78]. This has addressed the poor economics of bijel fabrication to date, as the relatively high cost of Stöber silica and variation between particle batches inhibits the scaling up of processes to an industrial level.

Another barrier to the scaling up of bijel formation is the dependence on a temperature quench. It would be easier if bijels could be made by direct-mixing, i.e. shearing or agitating the two liquid phases into the bicontinuous structure, in a similar fashion to the preparation of Pickering emulsions from a starting point of two completely phase-separated liquids. Evidence for the potential of this approach comes from Ref. [79], where carboxylated polystyrene nanoparticles dispersed in a mixture of silicone oils stabilized a wool-like structure after sustained mixing. It is not inconceivable that the same approach could be

applied to other systems which would result in bicontinuous structures similar to that formed by spinodal decomposition.

Another alternative method, to avoid the use of thermal quenching, is a technique entitled STRIPS (Solvent Transfer-Induced Phase Separation) [80]. A ternary mixture of diethylphthalate, ethanol and an aqueous dispersion of silica nanoparticles ($r = 22$ nm) is prepared at such a composition as to induce spinodal decomposition when exposed to a reservoir of aqueous phase. Another advantage to this method is the ability to produce bijel samples continuously and with a larger variety of immiscible liquid combinations, as opposed to the binary liquid batch-type methodology used so far. However, the versatile nature of the process also allows the creation of bijel 'particles', similar to the polymer monoliths derived from W/L bijels [54], along with fibers and membranes. Like binary liquid bijels, the characteristic domain size scales inversely with particle volume fraction, and in the case of the fibers can even be hierarchical.

In a similar fashion, solvent evaporation can be used in a system of polystyrene (PS) and poly(methyl-methacrylate) (PMMA) along with sterically-stabilized Janus particles to stabilize bicontinuous morphologies with 74 nm $< L <$ 1000 nm for particle volume fractions of 8% to 40% [81]. Other polymeric systems can also be stabilized by colloids into bicontinuous structures [82], including food-based polymer systems [83–85]. For more on polymeric systems the reader is directed to Refs. [82, 86].

1.6.2 Post-processing, rheology and monogel formation

Once the experimental protocols were established for preparing bijels in the laboratory, the next step was to try to turn the bijel structure into something potentially useful. In this endeavour, it was found that exposing a W/L bijel to a reservoir of an appropriate cross-linkable monomer allows the polymerization of one of the fluid phases [54]. A mixture composed of an acrylate based monomer and photo-initiator was chosen based on its preferable miscibility with the lutidine-rich phase, and was allowed to diffuse through the lutidine-rich channel. Subsequent polymerization using UV radiation rendered the lutidine-rich phase solid, and draining away the other fluid phase leaves behind a macroporous material with the bicontinuity maintained. Bicontinuous macroporous materials can impart advanced transport, mechanical and electrochemical properties for many applications [22, 25–28, 56, 87]. Since the porosity of the bijel can be tuned

via the volume fraction and/or size of the colloids, so can the porosity of the resultant polymer monolith. Varying the density of the cross linking polymer can impart micro- or nano-porosity to the polymerized channel, which would be advantageous for applications including chemical sensing and gas storage. Such hierarchically porous structures have been realized as silver [88] and gold [89] monoliths.

The NM/ED system can also be polymerized by the monomer diffusion/UV irradiation method, but is much more difficult to achieve and hence has a drastically lower success rate. The monomer/photo-iniator mixture has to be diluted with nitromethane, and takes a prohibitive length of time to diffuse through and fill the NM-rich channel. Direct application of the procedures developed for W/L to NM/ED results in the catastrophic failure of the bijel structure. To investigate the cause of the difference, the rheological properties of both W/L and NM/ED bijels were studied [90]. As expected, both systems exhibit elastic behaviour after bijel formation, however the elastic modulus for W/L bijels was an order of magnitude greater. The W/L elastic modulus also increased over a short time immediately after bijel formation, whereas the NM/ED modulus was relatively static. This measurement complements the experimental observation that a W/L bijel must be left for a short period of time before exposure to the monomer mixture, otherwise the structure fails [54].

The increase in elastic modulus of the W/L bijel also coincides with the following observation. If the bijel is left for this short time and then the liquids are allowed to remix by cooling to room temperature, the colloidal skeleton remains intact. This 'monogel' continues to exhibit elastic behaviour, albeit at smaller magnitudes, and is likely to be the crucial factor in the post-processability of the W/L bijel [54, 90, 91]. This behaviour is also found in a polystyrene/polybutadiene mixture [92], with an increase in elastic modulus over time correlating with the formation of a monogel. It is still unclear exactly what kind of particle-particle interactions are capable of stabilizing a monogel, but it was suggested that it might be a combination of short-ranged attractive and long-ranged repulsive forces [91]. A deep primary energy minimum (in the DLVO potential, see section 2.1.4) can be reached if a large barrier is overcome, and since the attractive capillary forces have the same order of magnitude as the maximum repulsive forces of the particles, it is not inconceivable that a monogel could form via this mechanism. However, the question still remains as to why monogel formation in the NM/ED system is non-apparent – the difference in

silica surface chemistry is a possibility.

1.7 Open questions

The experimentally realized bijels occupy a range of pore sizes and material properties which could lend them to certain applications. The W/L bijel is promising in terms of post-processing for said applications, because of its ability to produce highly homogenous samples (as opposed to the continuous STRIPS process of Haase *et al.* [80] which can create samples in large quantities but with a higher degree of heterogeneity). For some uses, e.g. catalyst supports [27, 28], the pore size of the W/L bijel needs to be reduced, perhaps down to the scale that was originally envisaged by the simulations [5] (i.e. $r \approx 5$ nm, $L \approx 10$s of nm). Pore size has a lower limit for any particular size r of particles, since the maximum volume fraction achievable for hard spheres is 74%. The lower limit is, in practice, much higher than that prescribed for $\phi = 74\%$ because adding colloidal particles above a certain amount (say, $\phi = 10\%$) to a binary liquid will affect the phase diagram by increasing the likelihood of heterogenous nucleation [43]. Such medium - large volume fractions of dispersed particles are also prone to forming unwanted gels in the bulk [12]. Hence, to produce progressively smaller pore sizes it is necessary to use smaller particles. Although simulations have provided strong indications that such a small-pore bijel would be stable, this is yet to be experimentally verified. Moreover, it is not known if this is achievable with currently devised experimental protocols.

Monogel formation is yet to be fully understood, but is likely coupled to the complex chemical behaviour of the water/lutidine/silica system. This crucial aspect of the W/L bijel's applicability to post processing techniques renders it an important area of research. Also, it may be advantageous to find a way to induce monogel formation in a system which otherwise wouldn't exhibit this behaviour, for example deliberately cross-linking the particles at the interface.

One fundamental difference between bijels in experiments and bijels in simulations is the finite temperature quench rate. This will always exist in experiments but has yet to be included in simulations. It is not entirely clear what difference this makes to the mechanics of bijel formation and the resultant structures. This concern has been briefly addressed experimentally [75, 93] and theoretically [25, 76, 94], suggesting that the quench rate might control the coarsening rate via

the dependence of interfacial tension on quench depth, and hence – during a temperature change at a finite rate – time.

This thesis aims to address these open questions. First, we adapt experimental protocols to create W/L bijels with smaller particles and uncover several advantages of smaller particles over the larger particles used previously (Chapter 3), paving the way for polymerized pore sizes of less than 10 μm. We also look at the effect of the finite quench rate on the formation kinetics. We then characterize the bijel in a way which allows us to see, in a quantitative fashion, the effect of the finite quench rate, the choice of particle size and sample age on the resultant structures (Chapter 4). Monogel mechanisms and bijel dynamics in general are probed by diffusing wave spectroscopy in Chapter 5, allowing us to measure the interfacial particle dynamics. Finally, in Chapter 6, we stabilize bijels with particles of two principle sizes and study the competitive mechanisms at play to complement the findings of previous Chapters.

Chapter 2

Materials and methods

2.1 Particle synthesis and characterization

2.1.1 Stöber synthesis of colloidal silica

Materials

Tetraethyl orthosilicate (TEOS, $\geq$ 99%, Aldrich), 35% ammonia solution (aqueous, reagent grade, Fisher Scientific), ethanol absolute (VWR Chemicals), fluorescein isothiocynate (FITC, 90% isomer 1, Aldrich), rhodamine B isothiocyanate (RITC, mixed isomers, Aldrich) and (3-aminopropyl)triethoxysilane (APTES, 99%, Aldrich) were used as received.

Method

The Stöber process [65] allows the preparation of monodisperse ($<$ 15% polydispersity) dispersions of colloidal silica with controllable and quantifiable surface chemistries. As a one-pot synthesis, it is relatively easy to carry out multiple times in the laboratory. To prepare particles of different (principal) sizes, we used temperature as a control parameter, with lower temperatures resulting in larger particles, essentially because higher temperatures result in a larger number of particle nuclei [95]. To make the particles fluorescent, allowing us to see the particles' locations within samples, we follow a procedure similar to that used by

Van Blaaderen and Vrij [96, 97]. The procedure incorporates a fluorescent dye (e.g. FITC) in to the silica matrix with the aid of a linking molecule APTES.

The general procedure for the preparation of our fluorescent Stöber silica particles was as follows. A dye mixture of APTES and either FITC or RITC was prepared by first measuring out the desired quantity of dye powder then mixing it with a quantity of APTES, so that APTES would be in molar excess of 9:1. The mixing was performed with a magnetic stirrer bar at 1000rpm for several hours (overnight). The vial containing the mixture was covered in tin foil to reduce the exposure of the dye to light. Once sufficiently mixed, 4.5 ml ethanol was added and mixed for a further hour. Separately, quantities of TEOS, (35%) ammonia solution and ethanol were measured out using measuring cylinders and an empty glass flask was washed thoroughly with ethanol and left to dry. The ingredients were added to the flask in the following order: ethanol, ammonia, TEOS, dye mixture. For a bench-top reaction the flask was left on the lab bench for c. 24 hours. For a controlled temperature reaction, the flask was wrapped in tin foil and placed in a pre-warmed oven at the desired temperature for c. 24 hours.

Batch	**Dye, (mg)**	**AP(mg)**	**E(ml)**	**Am(ml)**	**TE(ml)**	**T(°C)**
ASSi47	FITC, 35.7	182.7	434*	1.21	55.67	RT
ASSi92	FITC, 107.1	548.1	1500	186	60	10
ASSi81	FITC, 107.1	548.1	1500	186	60	10
ASSi72	FITC, 107.1	548.1	330	20.2	13.33	RT
ASSi76	FITC, 107.1	548.1	330	20.2	13.33	RT
MRSi01	FITC, 107.1	548.1	330	20.2	13.33	RT
MRSi02	RITC, 78.0	548.8	330	20.2	13.33	35
MRSi03	RITC, 78.0	549.5	330	20.2	13.33	45
MRSi04	RITC, 91.7	648.1	439.2	26.89	17.74	RT

Table 2.1: The quantities of chemicals used in the Stöber reactions to produce the particles used in this thesis. AP = (3-aminopropyl)triethoxysilane (APTES), E = ethanol, Am = 35% aqueous ammonia solution, TE = tetraethylorthosilicate (TEOS), T = reaction temperature, RT = room temperature (about 20°C). The two dyes used were fluorescein isothiocynate (FITC) and rhodamine B isothiocynate (RITC). * Methanol used instead of ethanol to achieve a particle size of $r = 5$ nm.

Table 2.1 shows the range of conditions used to produce the particles used in this thesis. The largest particles (300 nm $< r <$ 400 nm) resulted from the reactions being carried out in a refrigerator with a temperature of 10°C, with an increase in temperature resulting in a decrease in particle size (see next section).

After the completion of the reaction the newly formed particles were washed twice in ethanol and 8 times in de-ionized water, with an hour of sonication (VWR sonication bath) after each redispersion. This was sufficient to remove excess dye and unreacted chemicals. Before use, the particles were left overnight in a fume hood until the particles formed a 'cake', which were subsequently ground up using a mortar and pestle.

Batch ASSi47 was of size $r = 5$ nm, too small to exist safely in powder form in the lab. Therefore, to isolate the particles from the reaction mixture, a dialysis method was used. The dialysis tubing was boiled in preparation ten times over in fresh distilled water. First, to remove the ammonia, the mixture was dialysed in ethanol twice. Then to remove the ethanol, the mixture was dialysed in distilled water five times.

2.1.2 Particle sizing with TEM and DLS

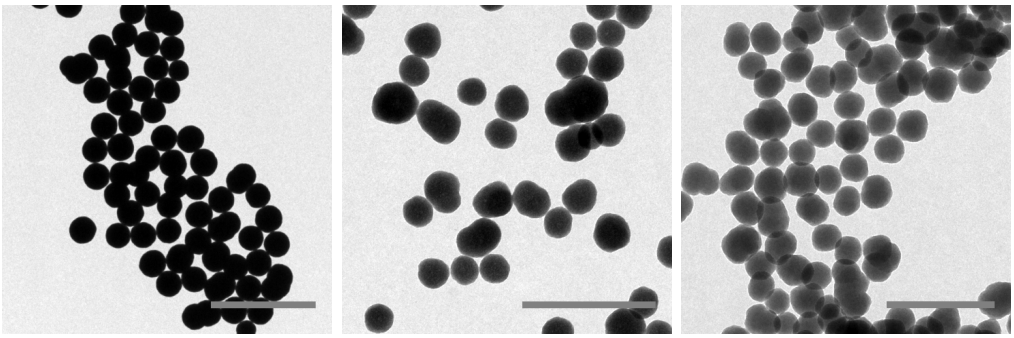

(a) **(b)** **(c)**

Figure 2.1: Transmission electron microscopy images of some of the particles made for use in this thesis. (a) ASSi92 (r = 367 nm, scale bar 3 μm); (b) ASSi72 (r = 63 nm, scale bar 0.5 μm); (c) MRSi03 (r = 21 nm, scale bar 0.3 μm).

In some cases, dynamic light scattering (DLS) was used to size the particles. A laser of wavelength $\lambda = 633$ nm was used along with a ALV/LSE-5004 digital correlator. The laser and detector were separated by an angle θ of 90°. An average correlation function was constructed using the individual correlation functions obtained from 10 separate acquisitions 30 seconds in length. Particle size was calculated by fitting an exponential function to the correlation function g:

$$g = exp(-\Gamma\tau)\Gamma = q^2 D \tag{2.1}$$

where $q = \frac{4\pi n_0}{\lambda}\sin\theta/2$ and D is the particle diffusion coefficient, equal to $\frac{k_b T}{6\phi\eta r}$ where η is the fluid viscosity and r is the particle radius [98]. DLS was also used to verify that the sonication procedure resulted in a fully dispersed suspension with little aggregation.

Transmission electron microscopy (TEM) was also used to size (most of) the particles, specifically a Philips CM120 with a Gatan Orius CCD camera. The accelerating voltage was 80 or 100 kV, zoom level 1150× for the largest particles and up to 20,000 × for the smallest. A small amount ($\approx$ 0.5%) of particles was dispersed in ethanol by sonication (VWR sonication bath) and subsequently transferred to a TEM grid. TEM micrographs were obtained and image analysis performed using ImageJ [99] to size the particles. Figure 2.1 shows some typical images for the range of particle sizes studied.

To begin the analysis, images were binarized by choosing an appropriate threshold value. Then the watershed algorithm was applied to separate particles close to one another. Regions obviously not representing spherical particles were deselected for the analysis by hand, and the remaining regions were analyzed in terms of area. The area values were converted to radius values by applying the circle formula $r = \sqrt{A/\pi}$. Then the average radius value μ was calculated and a polydispersity (PD) calculated as

$$\text{PD} = (\sigma/\mu) \times 100\% \tag{2.2}$$

where σ is the standard deviation of the range of radius values for any one batch.

Batch	**Temperature (°C)**	**μ (nm)**	**PD (%)**	**No. particles**
ASSi47	RT	5 (DLS)	-	-
ASSi92	10	367	5.5	794
ASSi81	10	348	6.6	223
ASSi72	RT	63/80 (DLS)	15/-	375
ASSi76	RT	65	15	735
MRSi01	RT	62	9	72
MRSi02	35	44	12	336
MRSi03	45	21	13	285
MRSi04	RT	48	15	1298

Table 2.2: Average radii (μ) and polydispersity (PD) of the particles synthesized for use in this thesis. PD is calculated according to Equation 2.2.

Table 2.2 shows the particle sizes and polydispersities as measured by TEM and the image analysis protocol given above, and Figure 2.2 shows the corresponding

size distribution histograms. ASSi81 and ASSi72 were also analyzed with DLS, returning particle radii of 355 nm and 80 nm respectively, close to the values measured by TEM and confirming the presence of a single particle dispersion. The particles are prone to shrinkage in the TEM because the suspending solvent is evaporated off, explaining the smaller values. The larger relative discrepancy in the case of the 80/63 nm particles is also explained by the shrinkage – for the same reduction in volume, the radii of smaller particles must reduce more. The radii values we will quote in this thesis will be the TEM results because we want to be able to quantitatively explore the effect of particle size – this can only be achieved by comparing sizes from the same characterization technique. Also, we will drop the μ notation and simply use r to symbolize the average radius, i.e. particle size. The particles with $r = 367$ & 348 nm are denoted microparticles (MPs) and the rest are denoted nanoparticles (NPs).

Note that one potentially important difference between particles of different sizes is their apparent surface roughness – the NPs (Figure 2.1(b,c)) appear more 'boulder' like than the MPs (Figure 2.1(a)) which appear more spherical. This type of surface heterogeneity can lead to capillary forces between ostensibly spherical particles on a flat interface [60, 100, 101], and more complex capillary behaviour when residing at curved interfaces [102]. The capillary forces are in some cases even used to direct the assembly of particles at the interface [103, 104]. This feature may become important when interpreting some of the results in the following chapters (see for example 3.4.3, 3.4.4 and 4.4.4).

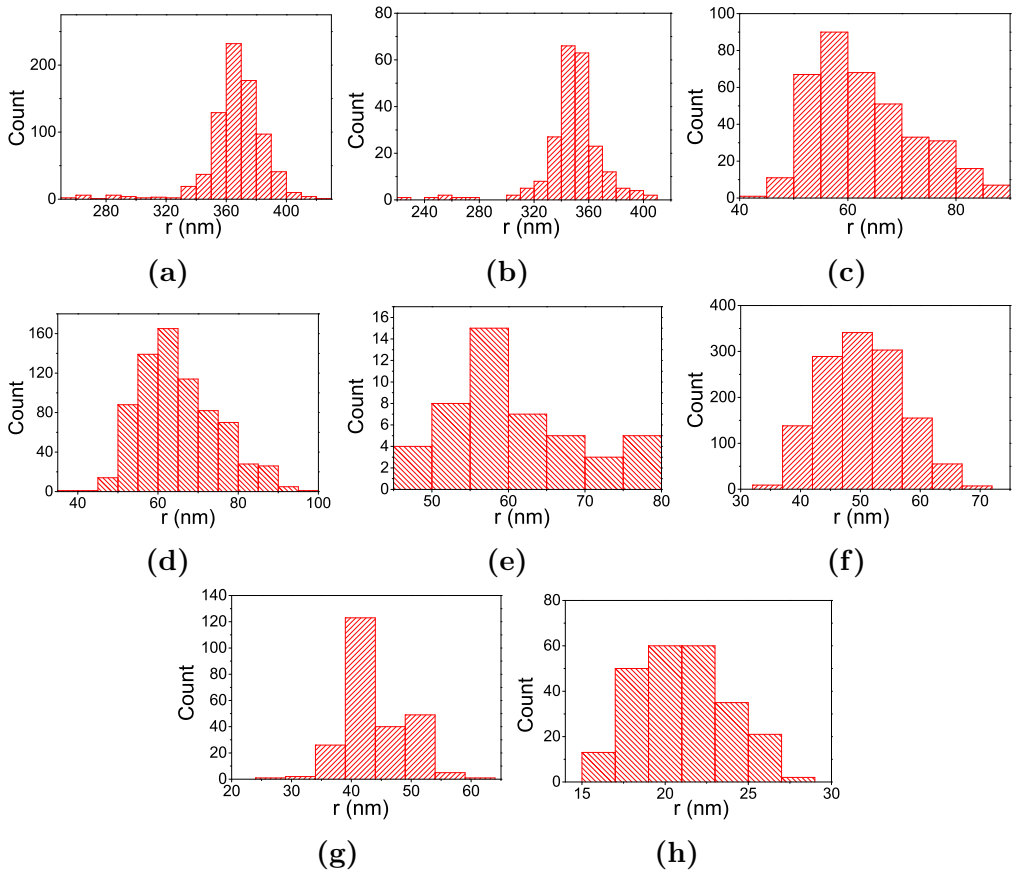

Figure 2.2: The size distribution histograms for the particle batches measured using TEM in order of decreasing size: (a) ASSi92, (b) ASSi81, (c) ASSi72, (d) ASSi76, (e) MRSi01, (f) MRSi04, (g) MRSi02, (h) MRSi03.

2.1.3 Particle densities

In order to convert the mass of particles added to a sample into a particle volume fraction, we need to know the particle density. Typical amorphous silica density is reported as about 2 g/ml in the literature [105], however the density of Stöber silica particles similar to the ones prepared here are lower at around 1.5 g/ml [96, 97]. To measure the density of the particles, we use a density meter and prepare multiple samples at various mass fractions of particles in water (ASSi81 MPs, $r = 348$ nm) or ethanol (ASSi72 NPs, $r = 63$ nm) dispersed with sonication (VWR sonication bath). The following scheme is used to calculate the particle densities from the measured sample densities.

Assuming no penetration of the solvent to the inside of the particles, volume is conserved, i.e. $V_{\mathrm{TOT}} = V_{\mathrm{P}} + V_{\mathrm{S}}$ where P stands for particle and S stands for

solvent. Replacing the volumes with M/ρ where M is mass and ρ is density and rearranging we arrive at

$$\frac{1}{\rho_{\mathrm{TOT}}} = \frac{\phi_{\mathrm{P}}}{\rho_{\mathrm{P}}} + \frac{\phi_{\mathrm{S}}}{\rho_{\mathrm{S}}} \tag{2.3}$$

where ϕ is the mass fraction M/M_{TOT}. For a system consisting solely of solvent and particles, $\phi_{\mathrm{S}} = 1 - \phi_{\mathrm{P}}$. Substituting this in and rearranging we finally arrive at

$$\frac{1}{\rho_{\mathrm{TOT}}} = \phi_{\mathrm{M}} \left(\frac{1}{\rho_{\mathrm{P}}} - \frac{1}{\rho_{\mathrm{S}}} \right) + \frac{1}{\rho_{\mathrm{S}}} \tag{2.4}$$

Plotting $\frac{1}{\rho_{\mathrm{TOT}}}$ against ϕ_{M} gives a straight line with gradient $(\frac{1}{\rho_{\mathrm{P}}} - \frac{1}{\rho_{\mathrm{S}}})$ and intercept $\frac{1}{\rho_{\mathrm{S}}}$.

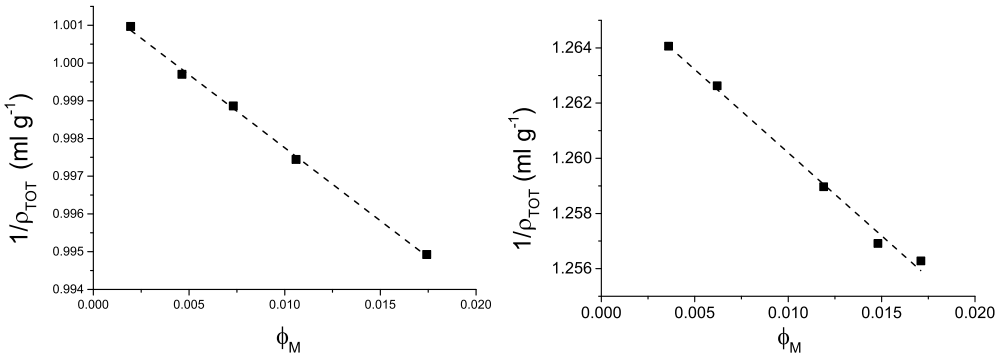

(a) **(b)**

Figure 2.3: Plots of inverse total density ρ_{TOT} against particle mass fraction ϕ_{M} for ASSi81 (a) and ASSi72 (b), yielding densities of 1.63(3) and 1.51(6) g/ml respectively. The y-intercepts correspond to the solvent densities, giving 1.27 g/ml for ethanol (a) and 1.00 g/ml for water.

Figure 2.3 shows the measurements of (inverse) total density ρ_{TOT} against particle mass fraction ϕ_{M} for two particle batches, ASSi81 (r = 348 nm) and ASSi72 (r = 63 nm), yielding densities of 1.63(3) and 1.51(6) g/ml respectively. The y-intercepts give the solvent densities as 0.998 g/ml for water and 0.790 g/ml for ethanol, matching with literature values [42]. The difference in density between the MPs and NPs is caused, presumably, by the the higher dye concentration by volume [97], which could also lead to enhanced shrinkage in the vacuum of the TEM [106], thereby partly explaining the difference between particle size from DLS and TEM. These densities were used when preparing samples – for MPs the value of 1.63 g/ml was used and for NPs the value of 1.51 g/ml was used.

2.1.4 Particle surface chemistry

Charge stabilization

According to the DLVO theory of colloidal stability, a dispersion of silica will be stable if the surfaces of the particles are sufficiently charged and repel each other to withstand their attractive van der Waals potential, given by

$$U(R_1, R_2, h) = -\frac{AR_1R_2}{(R_1 + R_2)6h} \tag{2.5}$$

where U is the potential, h the particle separation A the Hamaker constant and R_1 and R_2 the particle radii [12]. Note that Eq. 2.5 is only valid in the limit of closest approach, where $h \ll R_1$ or R_2. A depends on the electrostatic properties of the suspending medium and the dispersed material and is usually of the order 10^{-19} J. In general, larger particles attract each other more strongly [12]. When silica is dispersed in a polar solvent like water (as we do in this thesis), the surface silanol (SiOH) groups become dissociated, with the positively-charged hydrogen ion leaving behind a negatively-charged SiO moiety [72]. The overall surface charge of a silica particle can be changed by many factors, including the polarity of the solvent, ionic strength and pH [107], the association of other molecules [108] and the concentration of silanol groups and/or other dissociable groups on the surface. For example, the organosilica particles used in this thesis not only possess silanol surface groups but also amine groups (NH_2) which may accept hydrogen ions to become a positively charged moiety.

With the silica surfaces charged, free ions in solution will form a double layer around the particle surfaces effectively screening the charge (see Figure 2.4), resulting in a repulsive potential energy well between neighbouring particles with a depth of

$$V_{\text{repulsion}} = 2\pi\epsilon a\zeta^2 e^{-\kappa D} \tag{2.6}$$

where ϵ is the solvent permittivity, ζ the zeta potential, a the radius of the particle and κ is a function of the ionic composition. If the potentials involved are small, the Debye-Huckel approximation is used to arrive at an expression for κ;

$$\kappa = \left(\frac{2e^2 n_0 z^2}{\epsilon\epsilon_0 k_B T}\right)^{1/2} \tag{2.7}$$

where e is the elementary charge, z the ion valency and n_0 the number density

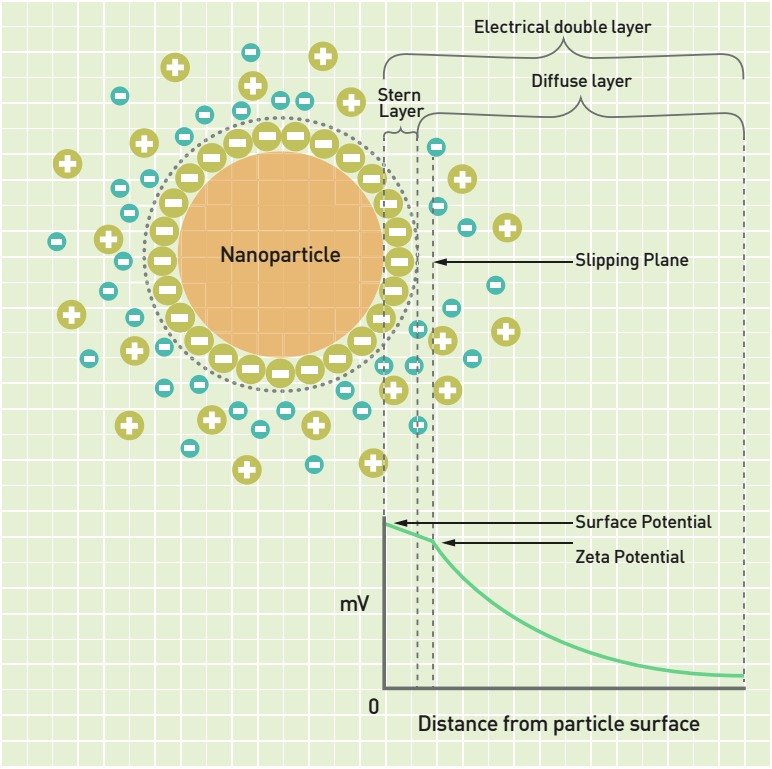

Figure 2.4: A schematic of the electrical double layer which forms around a charged particle in an electrolyte solution. The Zeta potential is the electrostatic potential at the edge of the slip layer which is the effective charge seen by neighbouring particles and provides stabilization against flocculation and coagulation. Image taken from Malvern Zetasizer Nano Z manual [7].

of ions. κ^{-1} is the Debye screening length, the distance over which the potential decreases by 1/e. The Zeta potential is the electrostatic potential at the edge of the slipping plane, which is effectively the charge which is 'seen' by neighbouring particles and provides the electrostatic stabilization against flocculation and coagulation.

Controlling wettability by modified drying

In order for the silica particles to attach to a liquid-liquid interface with the (roughly) 90° contact angle required for bijel stabilization, the surface chemistry must show equal affinity for both liquid phases [4–6, 109]. To date this has been achieved by two routes - chemically modifying the particles with the hydrophobic agent hexamethyldisilazane (HMDS) or by baking the particles under vacuum at elevated temperature ($\approx$ 170°C). The former method is used for preparing

particles for use in the nitromethane/ethanediol bijel system [36], whereas the latter is used in the water/lutidine (W/L) system [6, 68].

The interaction of W/L mixtures and silica surfaces is complex [69]. Native silica particles are hydrophilic [72], but on approach to spinodal decomposition they are pre-wetted by the lutidine and become, in effect, hydrophobic [70]. This renders them unable to stabilize W/L bijels, as they will simply partition to the lutidine-rich phase. This behaviour is not seen with the fluorescently dyed particles and is likely due to the linking molecule APTES which is added in excess, leaving many amine groups exposed on the surface [68]. This, combined with the surface silanols (Si-OH), provides an interesting interplay between protonation and deprotonation sites when the particles are dispersed in a solvent.

After we prepared a new particle batch, or wanted to use a batch which had been stored for over a month, we had to ascertain the drying time required for the particles to be sufficiently neutrally-wetting. To do this, small amounts ($\approx$ 50 mg) were measured out in 7 ml vials and baked in a vacuum oven (Binder VD23) at a pressure of 20 mBar and a temperature of 170°C. The oven was warmed to this temperature prior to the baking and allowed to equilibrate at this temperature for at least 30 minutes before particles were inserted. To find the right drying time for bijel formation, we began by scanning a large range e.g. 1, 2, and 3 hours, and then attempted to use the particles to make bijels. By inspecting the results, and comparing to previous studies [68], we decided where the desired drying time was and refined. Using particles which were not dried for long enough resulted in a lutidine-in-water emulsion, whereas using particles which were dried too long resulted in a water-in-lutidine emulsion, although this only happened if the particles were dried for a several hours [68]. This may be due to the saturation of the baking-induced mechanisms for modifying the wettability [68] and/or the phase asymmetry of the W/L phase diagram which heavily favours the water-rich phase to be continuous [45, 68, 110].

Zeta potentials as function of drying time

To explore the physico-chemical changes which take place on the particle surfaces during the baking, we performed Zeta potential measurements as a function of drying time. Note that although we wish to probe changes in the particle *surface* chemistry, we are limited by the Zeta potential technique to probing the electrostatic potential at the edge of the *slip layer*, which makes a statement of

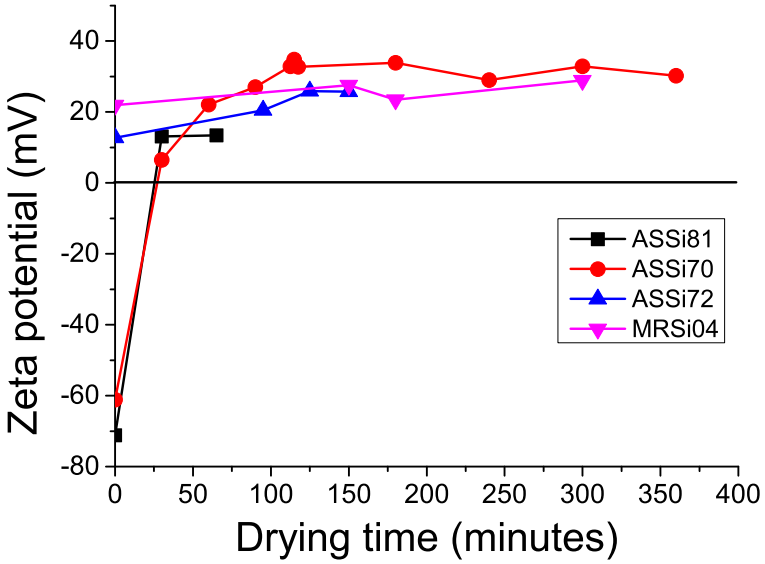

Figure 2.5: The zeta potentials of some of the particles used in this thesis as a function of drying time. ASSi81 and ASSi70 (of which ASSi81 is a repeat batch) are microparticles ($r \approx 350$ nm), ASSi72 are FITC-labelled nanoparticles ($r = 63$ nm) and MRSi04 are RITC-labelled nanoparticles ($r = 48$ nm).

the potential at the particle surface only an inference. Nonetheless, this method remains the most applicable one for studying the particle surface chemistry in situ and allows us to establish trends even if the absolute values are to be treated with caution.

To measure Zeta potential, we used a Malvern Zetasizer Nano Z. A small amount of particles (volume fraction $\approx 0.5\%$) was dispersed in deionized water using a sonication bath (VWR). Usually, a salt is added to dispersion to decrease the Debye length and prevent particle interactions, but we want to know the charge properties of the particles in unsalted water since this is what's used in the bijel mixtures. The dispersion was then transferred to a folded capillary zeta cell (model DTS1060, Malvern) and placed carefully inside the Zetasizer. The sample was equilibrated to 25°C before beginning the measurement. By applying a voltage of 50 V a.c. to the sample cell and measuring the movement of the dispersed particles by laser doppler micro-electrophoresis, the Zetasizer measures the electrophoretic mobility M given by

$$M = \frac{2\epsilon\zeta f(Ka)}{3\eta} \tag{2.8}$$

where ϵ is the dielectric constant (units Fm^{-1}) and $f(Ka)$ is Henry's function,

which is approximated to either 1.5 (Smoluchowski) or 1.0 (Huckel). The Smoluchowski approximation was used given its validity in the case of aqueous dispersions.

The procedure was repeated (from sonication through to Zeta measurement) three times and an average of the results taken for a range of drying times. A transfer standard (DTS1230, Malvern) was used in between measurements to ensure consistency.

Figure 2.5 shows the results of the Zeta potential measurements for four particle batches. ASSi81 and ASSi70 are FITC-labelled $r \approx 350$ nm MPs, ASSi72 are FITC-labelled $r = 63$ nm NPs and MRSi04 are RITC-labelled $r = 50$ nm NPs. What the Zeta potential measurements show is that the chemical modification of the surface (with APTES and FITC/RITC) coupled with the drying procedure create positively charged particles, which is also a necessary (but not sufficient) prerequisite for bijel formation. Also, drying for longer results in more positively charged particles generally. Note that the reason the MPs begin with a large negative potential is due to the undried particles retaining a significant amount of ammonia from the reaction solution, which is evaporated off after 30 mins of drying. The small particles do not have this problem, presumably due to their lower density allowing water to penetrate the porous particle matrix to remove the excess ammonia during the cleaning process. Also, since the particles are smaller, the pathlength for water molecules to the centre of the particles is smaller.

Empirically, it was found that the zeta potential of the particles must be around +20 mV before it is possible to find a drying time which results in bijel formation. The precise drying time for each batch tended to be different but similar to other batches of the same particle size. For example, MPs tended to need upwards of 4 hours drying, whereas the NPs ($r = 63$ nm) needed between 2.5-3 hours and the smaller NPs less than 2.5 hours. The results also reaffirm the importance of the APTES in providing the positive charge groups on the silica surface resulting in an overall positively charged surface [111–113], without which bijel formation is not possible [68].

2.2 Bijel preparation

2.2.1 Water/lutidine

Materials

Distilled water was deionized using a Milli-Q (Millipore) filtration system at a resistivity of at least 12 MΩ cm. Lutidine (2,6-dimethylpyridine, ≥99% Aldrich) was used as received. Nile Red or Nile Blue (Aldrich) were used as received.

Method

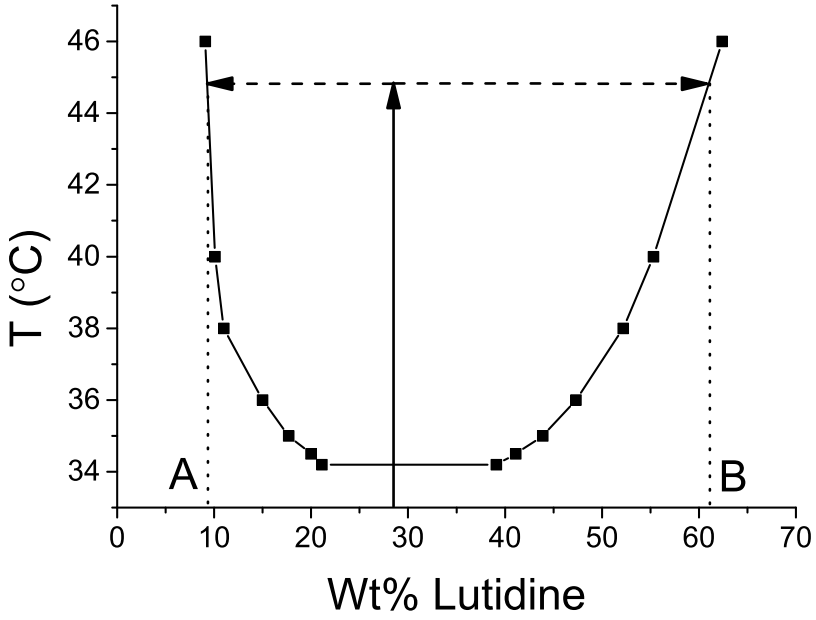

Figure 2.6: Water/lutidine phase diagram, plotting existing data measured by Grattoni *et al.*[8] Samples are prepared in the single-phase regime (i.e. below the critical temperature of 34.1°C) at a critical weight fraction of 28% lutidine and are subsequently quenched to 45°C (or sometimes 50°C). Coexisting phases of lutidine-poor (composition marked A) and lutidine-rich (composition marked B) are created.

Unless otherwise stated in a Chapter's Methods section, bijels were prepared by the following standard protocol. To make bijels, the suitably-dried colloidal particles were dispersed in deionized water using an ultrasonic probe (Sonics Vibracell). The MPs were sonicated for (2 × 2) minutes at 8W power, with 10 seconds of vortex mixing after each sonication step. The NPs were sonicated for

an extra 10 minutes at 8W with an extra 10 seconds of vortex mixing, to ensure proper redispersion. Subsequently, lutidine was added along with Nile Red dye (or Nile Blue when RITC labelled particles were dispersed) at a concentration of around 10 μM, to give a mixture with mass ratio of W:L = 72:28. We investigated a range of dye concentrations and found no significant effect on bijel formation in the range 1 - 10 μM, as also found for the alternative rhodamine B [68]. This particular mass ratio was used to prepare the system at its critical composition [8] (see Figure 2.6) so that spinodal decomposition would be (at least initially) the preferred phase separation mechanism [6]. Mixtures were transferred to a glass cuvette (1mm path length, Starna Scientific) ready for quenching.

The compositions of the coexisting phases are given by the tie lines which intersect the x-axis at points A and B, e.g. the lutidine-poor phase is composed of about 9 wt% lutidine and 91 wt% water. The weight fractions of the coexisting phases are calculated from the phase diagram using the Lever rule [12];

$$X_{\mathrm{W}} = \frac{B - C_0}{B - A} \tag{2.9}$$

$$X_{\mathrm{L}} = \frac{C_0 - A}{B - A} \tag{2.10}$$

where X_{W} is the weight fraction of the water-rich phase, X_{L} is the weight fraction of the lutidine-rich phase and C_0 is the concentration of lutidine in the entire sample (i.e. 28 wt%). This gives weight fractions of 64% (W) and 36% (L) at 50°C. By using measurements of the densities of the coexisting phases [8], the weight fractions can be converted to volume fractions, giving 63% (W) and 37% (L) at 50°C, as the lutidine-rich phase is slightly less dense than the water-rich phase. The relative volume fractions of the coexisting phases depends on temperature as per Figure 2.7. Note that these relative volumes are close to the 5:9 limit for bicontinuous structures seen in simulations when the contact angle of the particles is 90° [45].

The mixtures were quenched from room temperature up to 45 or 50°C (the vertical line in Figure 2.6) in various ways depending on the desired rate. A rate of 1 - 5°C/min was achieved by first inserting the cuvette inside an aluminium block and placing it in a temperature stage (Instec mK1000), then programming the stage to ramp the temperature. A rate of 17°C/min was achieved by pre-warming the metal block to 45°C before the insertion of the cuvette. A rate of 350°C/min was achieved by placing the cuvette on top of a small cardboard box inside a

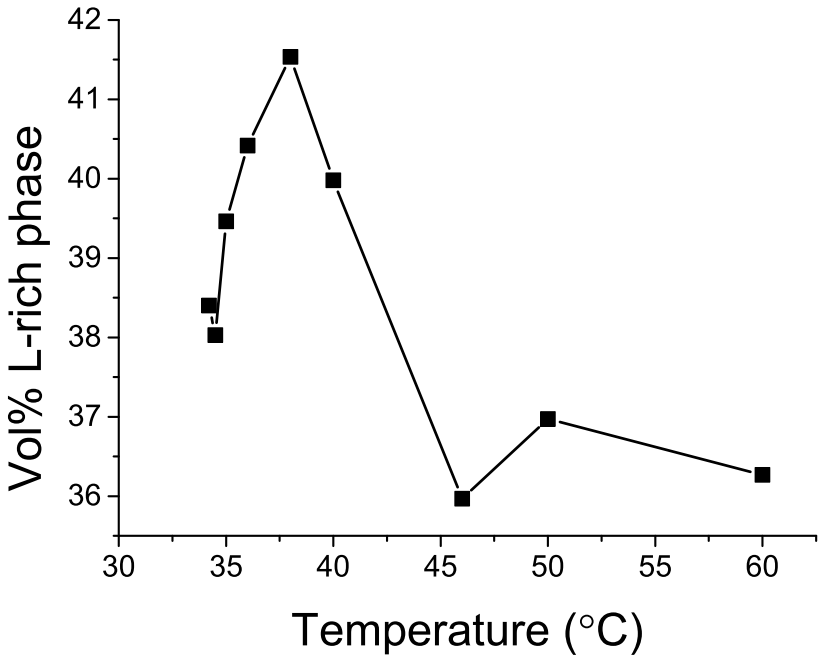

Figure 2.7: The volume fraction of the Lutidine-rich (L-rich) phase as a function of temperature for a initial composition of lutidine of 28 wt%.

microwave (DeLonghi, P80D20EL-T5A/H, 800W), set to 'auto-defrost' for 5 or 6 seconds. In all cases, when the temperature exceeded 34.1°C the mixture phase separated via spinodal decomposition, resulting in the particles attaching to the liquid-liquid interface and ultimately arresting the bicontinuous structure, with coexisting phase compositions given by the positions A & B in Figure 2.6.

Temperature gradients

To account for the potential impact of temperature gradients, we have carefully characterized our quenching procedures. For slow quenches, i.e. between 1 and 5°C/min, we have verified using a thermocouple that the sample temperature doesn't lag the stage temperature. For the fastest quenches (350°C/min), the microwave heating should heat the sample homogeneously. For the medium quench rate of 17°C/min, there could be significant temperature gradients in the sample cell, but they are minimized by encasing the cell completely in an aluminium block. In Ref. [69], these gradients result in the confocal microscopy images showing one part of the sample at a later stage of spinodal decomposition than another part. We have not seen this when performing the work reported in this thesis. For example, confocal microscopy time series of the phase separation

show homogenous phase separation, as we report in Chapter 3 and Ref. [1]. We also scan samples to analyse homogeneity and find no significant variation in structure (at least when the bijels made are deemed to be acceptable quality), implying non-significant temperature gradients due to our quenching procedures (see Chapter 3).

2.2.2 Nitromethane/ethanediol

Materials

Ethanediol (Aldrich, 99.8%), nitromethane (Acros Organics, 99%, stored under nitrogen gas) and fluorescein (BDH) were used as received.

Method

Nitromethane/ethanediol bijels were prepared by Katherine Rumble according to the following procedure. HMDS-modified silica particles with $r = 290$ nm were added to nitromethane, and ethanediol doped with fluorescein was added to give a critical concentration (by mass) of NM:ED 64:36 [36]. Note that this system has an upper critical solution temperature, the opposite of the water/lutidine system, and hence requires cooling for the initiation of phase separation. The particles were dispersed by first heating the mixture in a water bath at a temperature of between 40 - 50 °C and then placing it in a hot ultrasonic bath (VWR). The mixture was then transferred to a 1mm path length cuvette (Starna Scientific) and returned to room temperature using a stirred water bath. This temperature quench resulted in spinodal decomposition of the liquids and ultimately a bijel as the particles attached and jammed at the liquid-liquid interface.

2.3 Fluorescence Confocal Microscopy

2.3.1 Principles

Here we explain the main principles underlying fluorescence confocal microscopy, which we used to image our bijel samples. Detailed overviews are contained in Refs. [114, 115]. We then outline the specific method and settings used for imaging.

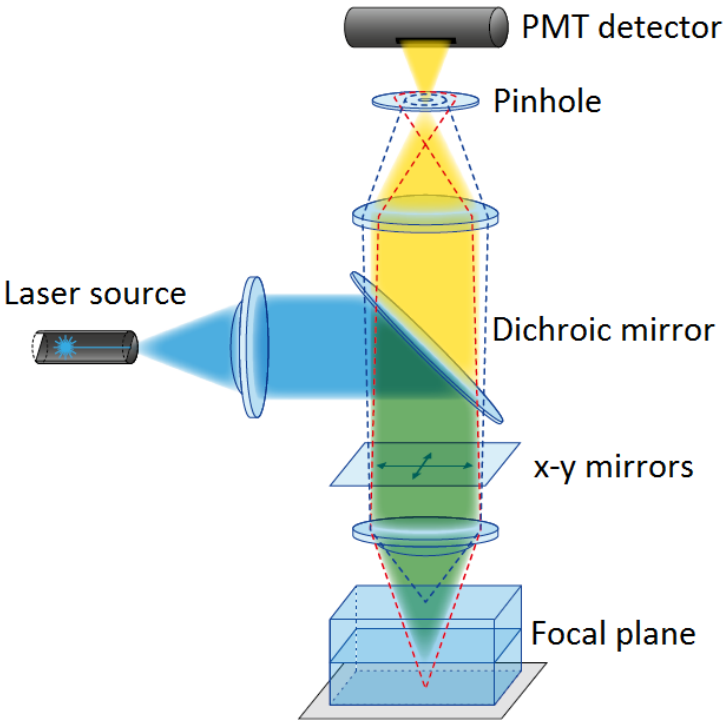

Figure 2.8: A ray diagram representing the confocal principle (taken from the Zeiss LSM 700 manual [9]). A coherent beam of light is directed on to the sample via a dichroic mirror and a set of x-y scanning mirrors, focussed by a lens, which excites the fluorescent species. The fluorescence emission then passes through the dichroic mirror, is focussed on to a pinhole, and the light from the focal point is allowed through the pinhole and on to a PMT detector.

Fluorescence confocal microscopy is a development of traditional microscopy techniques for magnifying and imaging fluorescent specimens, the signal from which would otherwise be swamped from outside the region of interest if it wasn't for the use of a pinhole in front of the detector. By using said pinhole to exclude

light not originating from the focal point, lateral and axial resolution is improved over widefield techniques. However, the improved image quality from confocal microscopy is primarily due to the optical sectioning capability (thanks to the improved axial resolution) rather than the increase in lateral resolution.

Figure 2.8 shows a diagram illustrating the confocal method. As can be seen, most of the light originating from outside the focal point does not make it through the pinhole and on to the photo-multiplier tube (PMT) detector. Scanning mirrors are used to move the focal point across the sample in a line by line raster to build up the image, and the dichroic mirror is used to direct the excitation laser beam at the sample while allowing the emitted radiation through to the detector. Filter sets can be used with multiple PMTs to look at different wavelengths of radiation simultaneously.

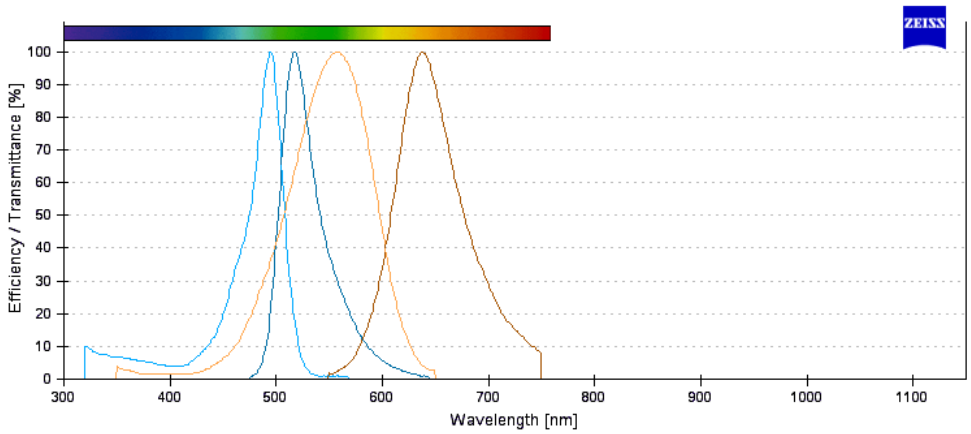

(a)

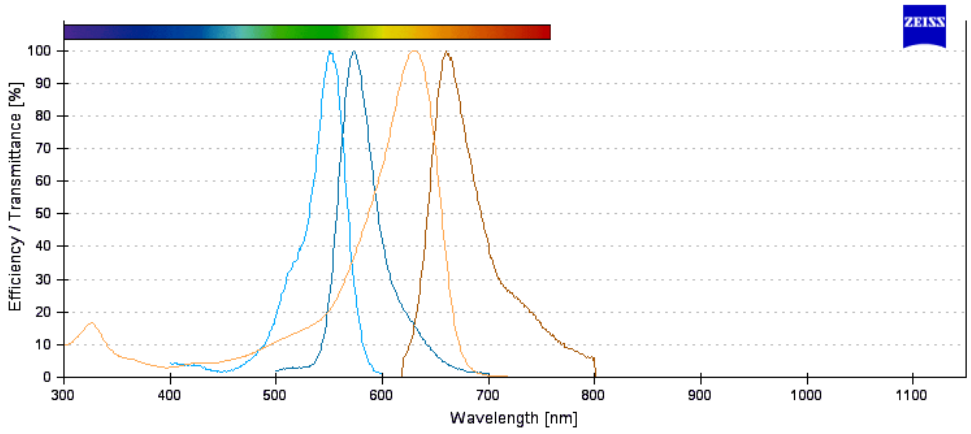

(b)

Figure 2.9: Illustrative Fluorescence spectra for (a) FITC (blue) and Nile Red (brown) in water and (b) RITC (blue) and Nile Blue (brown) in ethanol, with the light shades corresponding to excitation and the dark shades corresponding to emission. Data taken from the online Zeiss fluorescent dye database [10].

As mentioned in previous sections we are using several dyes to image the bijel system – FITC or RITC for imaging the particle locations and Nile Red/Blue or fluorescein to provide a contrast between the coexisting liquid phases e.g. water-rich and lutidine-rich. To image the particle locations and the contrasting phases simultaneously, we use FITC/Nile Red and RITC/Nile Blue combinations, the fluorescence spectra of which are shown in Figure 2.9. The lighter curves correspond to excitation whereas the darker curves correspond to emission. Note that these spectra serve as an illustration only because they may be modified by our choice of solvent. By using an appropriate filter set the FITC/RITC emission can be sent to PMT-1 and the Nile red/blue can be sent to PMT-2. This not only allows us to image the particles and the phases simultaneously, but also allows us to check if we have selected the correct wavelengths. To perform this check, we turn off e.g. the 555 nm laser and look for signal bleeding from e.g. FITC in to PMT-2. We adjust the position of the bandpass filter until an acceptably small amount of bleeding is observed. Bleeding is also minimised by reducing the power of the 488 nm laser (and increasing the gain on PMT-1) while increasing the power of the 555 nm laser (requiring less gain on PMT-2).

For a fluorescent point source, the lateral resolution is given by the radius of the central Airy disk in the diffraction image [115], given by

$$r_{airy} = 0.42\frac{\lambda_0}{NA} \tag{2.11}$$

where λ_0 is the excitation wavelength and NA is the numerical aperture of the objective lens. The numerical aperture is an effective collection angle for the lens, given by $NA = n\sin\theta$, where θ is half-angle of a cone focussed on the sample making the largest angle with the objective. The axial resolution is given by the full-width at half maximum of the point spread function, which is

$$FWHM = \frac{1.4n\lambda_0}{NA^2} \tag{2.12}$$

where n is the refractive index of the immersion medium (1 for air, or ≈ 1.4 for immersion oil).

The use of the pinhole in confocal microscopy means that only one point can be focussed on at a time, but with the inclusion of a scanning apparatus images can be formed by performing a line by line raster over an area of interest of the sample, which can be repeated at different z positions allowing a 3D scanning of the sample. Signal to noise ratio in the image acquisition can be improved

by averaging over many passes of the same area, as long as the sample is relatively stationary (otherwise the image will be blurred) and is not prone to photobleaching.

2.3.2 Method

All samples were imaged using a Zeiss Observer.Z1 inverted microscope with a Zeiss LSM700 confocal scanning unit. Two sets of settings were used depending on the combination of dyes, i.e. Nile Red and FITC or Nile Blue and RITC. Fluorescence excitation was provided by a 488 nm laser (for FITC), a 555 nm laser (for Nile Red or RITC), and a 639 nm laser (for Nile Blue). Emission filters were used as appropriate. Either a 10× (Zeiss EC-Plan NEOFLUAR, NA = 0.3), 20× or 40× (Zeiss LD-Plan NEOFLUAR, NA = 0.4 or 0.6 respectively) air objective was used to acquire images. Signal to noise was improved by averaging over 4-8 scans of the imaging region. Images were normally taken with the focal plane positioned just above the bottom of the sample cuvette, bypassing wall effects whilst imaging the sample with the least interference due to scattering.

Dye	λ_0	**10× NA 0.3**	**20× NA 0.4**	**40× NA 0.6**
FITC	488 nm	683/7591 nm	512/4270 nm	342/1898 nm
RITC	555 nm	777/8633 nm	583/4856 nm	389/2158 nm
Nile Red	555 nm	777/8633 nm	583/4856 nm	389/2158 nm
Nile Blue	639 nm	895/9940 nm	671/5591 nm	447/2485 nm

Table 2.3: The lateral/axial resolutions achieved by using different dye/objective combinations. λ_0 is the excitation wavelength, i.e. the wavelength of laser light used to excite the fluorescence of the dye and NA = numerical aperture. The resolution values are calculated using Eqs. 2.11 and 2.12.

We can estimate the lateral and axial resolutions of our imaging setup using Eqs. 2.11 and 2.12 to see what we can resolve in the bijel system. Table 2.3 shows the lateral and axial resolutions resulting from the use of different dye and objective combinations. In terms of the lengthscales in the bijel system, we are unable to resolve the particles (arguably we can resolve only the MPs, with the help of a deconvolution step) but can easily resolve the coexisting liquid domains (which have a size of between 10 and 100 μm) by choosing an appropriate magnification and numerical aperture.

2.4 Image analysis

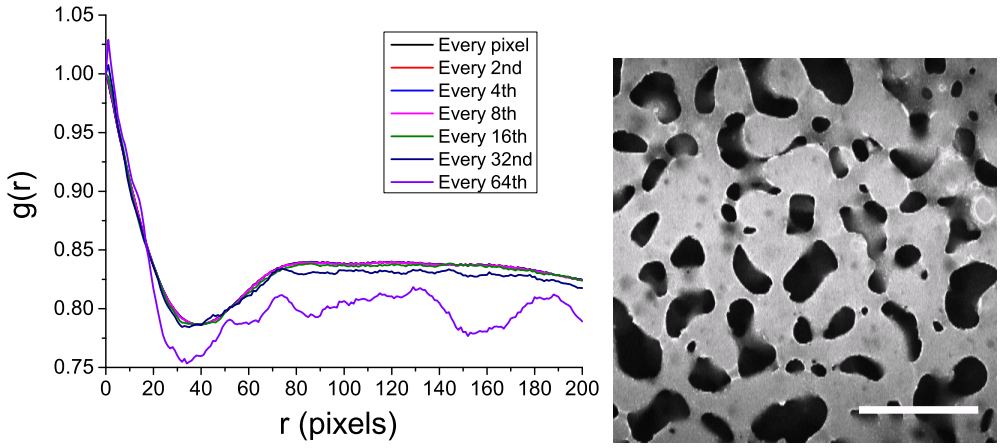

(a) (b)

Figure 2.10: (a) The radial distribution functions produced by the Matlab script labelled by the sampling frequency. (b) The confocal image of a nanoparticle stabilized water/lutidine bijel (r = 63 nm and ϕ = 0.6% quenched at 17°C/min) analysed by the Matlab script to produce the radial distribution functions shown in (a). The signal comes from Nile Red which resides in the lutidine-rich phase. Scale bar 200 μm.

To extract the average bijel channel width L, a pixel-based radial distribution function $g(r)$ was generated using a Matlab script. The script calculated the average magnitude of multiplied pairs (i, j) of pixel intensities separated by a distance r:

$$g(r) = \frac{\langle I_i(0) I_j(r) \rangle_{ij}}{\langle I_i(0)^2 \rangle_i} \tag{2.13}$$

To reduce the script's runtime to a reasonable length, the calculations were only performed on every second pixel – this was found not to affect the measured $g(r)$ which remains the same as long as the sampling frequency is larger than L (e.g. if L = 20 pixels, the $g(r)$ curves are pretty much identical as long as the script is sampling at least one in every 20 pixels).

Figure 2.10(a) shows an example of the radial distribution functions resulting from the analysis of a typical bijel image (b), and the effect of changing the sampling frequency. The characteristic lengthscale L is the location of the first minimum in the $g(r)$ [116], i.e. the average distance over which the pixel intensities are correlated. As mentioned above, the $g(r)$ remains the same up to a sampling rate of every 16th pixel, after which it becomes noisy and unreliable because the

rate approaches the position of the minimum ($\approx$ 40 pixels). Ideally, the $g(r)$ would oscillate regularly (with decreasing amplitude) with a wavelength equal to $2L$. However, several factors prevent this from happening. Due to noise in the fluorescence signal and/or the presence of droplets and/or the presence of a tilt in the sample geometry relative to the focal plane, the shape of the $g(r)$ beyond the first minimum is not ideal, and only the first minimum should be used to calculate L. This measurement procedure can be repeated with multiple images (at different random locations) of the same sample to arrive at an average value and an estimate of the uncertainty in the measurement e.g. the standard deviation.

To check the image analysis accuracy, we can manually measure the channel widths using ImageJ. After measuring 50 lengths on the image presented in Figure 2.10(b), we arrive at a lengthscale of 29 pixels with a standard deviation of 14 pixels (i.e. within one standard deviation of the value derived from the $g(r)$). The discrepancy in the mean value (40 vs 29) is likely due to the arbitrary choice, in the manual case, of what constitutes a channel and the orientation of the measurement, whereas the automated method averages the lengths of the channels over all orientations. Nonetheless, the radial distribution function calculation provides us with a standard method of measuring bijel lengthscale which can be applied to all of our samples, allowing us to compare bijels prepared with different parameters (e.g. particle size, quench rate – see Chapter 3).

2.5 Summary

In this Chapter we have outlined the experimental methods used in this thesis with accompanying theoretical descriptions where appropriate. To summarize, we have prepared Stöber silica particles of different sizes by using temperature as a control parameter. We have maintained (similar) surface chemistries by modifying the concentrations of dye in the reaction mixtures. The particles are dried at high temperature and under vacuum to modify their wettability sufficiently to stabilize bijels. Their surface chemistries were shown by Zeta potential measurements to be similar. We mainly study water/lutidine bijels but occasionally perform measurements on nitromethane/ethanediol bijels for comparison purposes. Temperature quench rates are controlled by either using a microwave or an aluminium block, and sample temperature is maintained by using a temperature stage. We image our samples with fluorescence confocal

microscopy, which allows us to both see the location of the particles (although we cannot resolve individual particles) and the structure of the co-existing liquid domains. Images are analysed using a Matlab script to extract the characteristic lengthscale of the structures.

Chapter 3

Nanoparticle stabilized bijels

3.1 Abstract

Water/lutidine (W/L) bijels can be prepared with a controllable characteristic domain size L, by choosing the size (r) and volume fraction (ϕ) of particles included in the fluid mixture ($L \propto r/\phi$). Reported L values in the literature are roughly between 10 & 100 μm for the simple (un-bridged [75]) bijel when using particles of size $r = 290$ nm [6]. ϕ in practice is limited to about 10%, so to access a smaller range of domain sizes, and hence make the bijel suitable for applications which need L <10 μm, r must be reduced. To this end, we have synthesized Stöber silica nanoparticles (NPs, $r = 63$ nm, 44 nm and 21 nm) with similar surface chemistries to their microparticle (MPs, $r \approx 300$ nm) counterparts, and used them to make W/L bijels. We demonstrate that these NPs pave the way for $L < 10$ μm and that they make bijel formation less sensitive to the choice of quench rate. However, a smaller fraction (vs MPs) of the added NPs adsorb to the liquid-liquid interface. We analyze the formation kinetics and find that the bijel 'failure' mechanism is due to the facilitation of domain pinch-off by MPs. We polymerize NP-stabilized bijels to demonstrate that the reduction in L for the bijel can be translated into an equivalent reduction in L for functional bicontinuous polymer monoliths. We also develop a new theoretical framework for understanding bijel formation and discover a practical limit on r at 44 nm, below which no reduction in L at constant volume fraction is achieved. Hence, to reduce particle size below 44 nm a new fabrication paradigm, which doesn't rely on charge stabilization, is required.

3.2 Introduction

Bicontinuous interfacially-jammed emulsion gels (bijels) are a relatively new and versatile class of soft materials with a number of possible technological applications. Initiating the spinodal decomposition of a binary liquid mixture in the presence of neutrally-wetting colloidal particles results in a non-equilibrium structure consisting of two tortuous interlocking channels, stabilized by a jammed layer of interfacial particles [64, 82] (see Chapter 1 for a detailed overview and Figure 3.1 for a schematic).

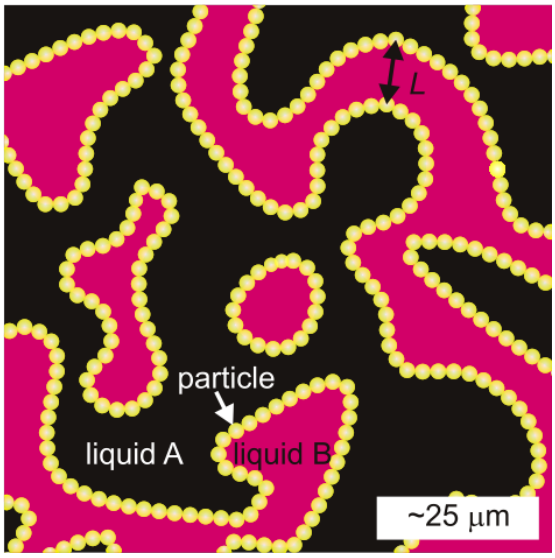

Figure 3.1: Schematic of a 2D slice through a 3D bijel: two tortuous interlocking liquid channels (water in black and lutidine in magenta), stabilized by a jammed layer of interfacial particles (yellow). The black arrow is the characteristic bijel length scale L, i.e. the average channel width or pore size. Adapted from Ref. [1].

The bicontinuous domains have a characteristic lengthscale (cross sectional width) L which scales as $L \propto \frac{r}{\phi}$, where r is the radius of the particles and ϕ is the volume fraction of the particles in the mixture [5]. Since the initial bijel simulations in 2005 [5] which considered nanoparticles (NPs, $r \approx 5$ nm) and an instantaneous quench into the two-phase region of the binary liquid phase diagram, the experimental realization of bijels has involved the use of much larger microparticles (MPs, $r \approx 300$ nm) and non-instantaneous quench rates above 17° C/min. Successful binary liquid combinations include nitromethane/ethanediol (NM/ED) [36, 75], and water/lutidine (W/L) [6].

The W/L bijel has been shown to be 'post-processable' – that is, by selectively

polymerizing one of the fluid channels, a three dimensional bicontinuous porous composite can be fabricated [54], with the NM/ED system proving inefficient or completely ineffective with respect to this process [90]. With W/L bijels, polymer composites with L values between 10 μm and 100 μm for $0.01 < \phi < 0.1$ [54] can be made. For applications such as catalysis, L values (or 'pore' sizes) of less than 10 μm, or even sub-micron (< 1 μm) would be desirable. Reducing L can be achieved by increasing ϕ at constant r, but the value of ϕ required to achieve sub-micron pores with MPs exceeds the random-close-packed value of 64%, rendering this approach unfeasible. The only other option is to reduce r, i.e. to use smaller particles. Another motivation for using smaller particles is to work towards answering the open questions regarding the long-term stability of bijels stabilized by the size of particles ($r \approx 5$ nm) envisaged by the initial [5] and subsequent [11, 45, 46, 58] simulations.

To begin to answer these questions and explore the possibility of using NPs to stabilize bijels, we use Stöber silica [65] NPs of radius $r = 63$ nm to stabilize a W/L bijel, which represents roughly a threefold reduction in r compared to previous studies [6]. To compare to said studies, we measure the characteristic lengthscale dependence on volume fraction of particles, and show the expected scaling relationship ($L \propto \frac{r}{\phi}$) but with a larger prefactor compared with MP-stabilized bijels, which suggests a lower particle uptake to the interface. We also investigate the kinetics of the bijel formation and report the ability of NPs to stabilize bijels under much slower quenching conditions (which provides a distinct materials synthesis advantage), which we explain by appealing to the concepts of interfacial bending moments and spontaneous curvatures. Finally, we show that the NP stabilized bijels can be post-processed into polymer monoliths, and observe reduced sensitivity to processing parameters (e.g. quench rate) which has resulted in a more robust material synthesis procedure. Hence, we have increased the range of pore sizes available for the robust synthesis of bicontinuous materials from bijels, thereby paving the way for an expansion of the range of possible bijel applications.

3.3 Methods

3.3.1 Particles

The particles used here were synthesized by the procedures outlined in Chapter 2.1; we repeat the relevant aspects for the benefit of the reader. Stöber silica particles, labeled with fluorescein (or rhodamine) isothiocyanate (FITC or RITC) were synthesized with different radii by controlling the reaction temperature. The sizes of particles (determined by TEM analysis) used in this chapter are $r = 63$, 44 and 21 nm (NPs) and $r = 348$ and 367 nm (MPs), and were prepared to have similar surface chemistries (see Chapter 2.1). To achieve neutral wetting conditions, small amounts of the particles were dried at 20 mBar and 170°C in an oven (Binder VD23) [68, 69]. This is thought to remove surface-bound water and may cause moderate dehydroxylation of the silica surface [72]. The exact drying time was determined by visual inspection of the resulting emulsions – bijels will only be stabilized by (sufficiently) neutrally-wetting particles.

3.3.2 Bijel preparation

Bijel preparation was performed as outlined in Chapter 2.2.1, with the NPs sonicated for longer than the MPs to ensure a good dispersion – both by 2 × 2 mins at 8W plus an extra 10 mins 8W for the NPs, with vortex mixing in between sonication steps. Nile Red or Nile Blue was used to dye the lutidine-rich phase, depending on the particle dye (FITC and RITC respectively). A range of quench rates were used as outlined in Chapter 2.2.1 – slow (1-5°C/min performed with a temperature stage ramp), medium (17°C/min inserting cold cuvette into pre-warmed aluminium block) and fast (350°C/min inside a microwave).

3.3.3 Imaging

Quenched bijels were imaged using fluorescence confocal microscopy as explained in Chapter 2.3. Fluorescence excitation was provided by a 488 nm laser (for FITC), a 555 nm laser (for Nile Red or RITC) and a 639 nm laser for Nile Blue; emission filters were used as appropriate. The two liquid domains could be distinguished by detecting the fluorescence of the Nile Red or Blue which

preferentially resides in the lutidine-rich phase, while the location of the particles could be determined by detecting the fluorescence of the FITC or RITC.

3.3.4 Image analysis

Characteristic lengthscales were extracted from 2D confocal images by the method outlined in Chapter 2.4. The process was repeated on at least three separate images of the same bijel sample, an average taken and the standard deviation used as an error estimate.

3.4 Results and discussion

3.4.1 Scaling behaviour

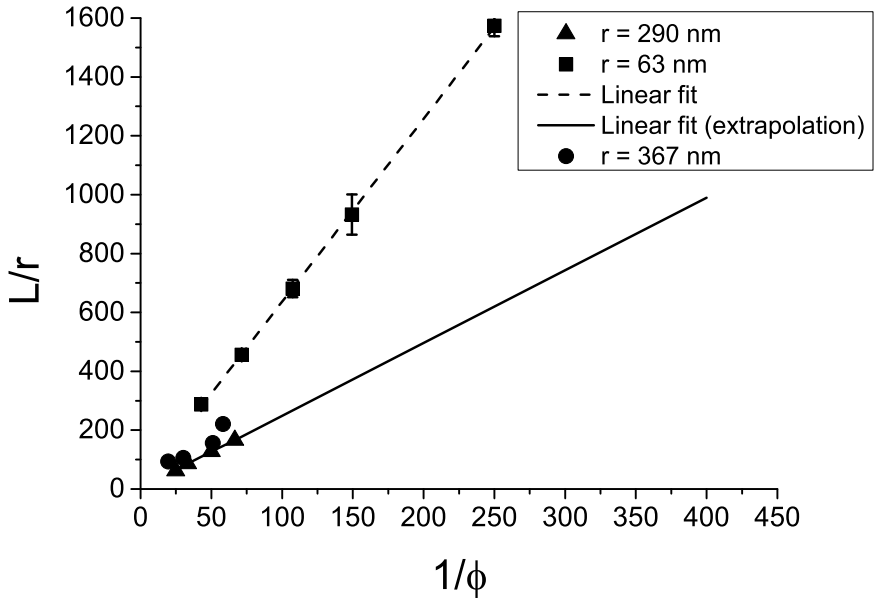

Figure 3.2: The characteristic lengthscale normalized by particle radius (L/r) as a function of the inverse volume fraction of particles ($1/\phi$). Squares: data gathered during the present work using 63 nm radius nanoparticles (NPs). Triangles: data presented in a previous study using 290nm radius microparticles (MPs) [6]. Circles: data gathered during present work with 367 nm radius MPs. Note the different gradients for the two sets of data - the larger gradient obtained from the NP particle data suggests that fewer particles have become attached to the interface (see text).

To begin the study of NP stabilized bijels, and quantitatively compare to similar studies in the literature, samples were prepared at various volume fractions (ϕ) in order to investigate the proposed scaling relationship $L \propto r/\phi$ [5], which has already been confirmed for MPs [6]. Figure 3.2 shows the bijel lengthscale normalized by particle radius (L/r) vs the inverse particle volume fraction $1/\phi$ for $r = 63$ nm (the NPs, squares), with data for $r = 290$ nm (the MPs, triangles) shown for comparison [6]. We also include our own MP data, using ASSi92 ($r = 367$ nm, circles). Our MP data is similar to the data presented in Ref. [6], apart from the last data point which deviates from the linear pattern of the previous three. But since our particles are about 27 % bigger, at the same low volume fraction we are probing the upper limit of 'normal' bijel stabilization at around 100 μm (as opposed to droplet-reinforced bijels [75] which can have $L = 450$ μm), above which bijel formation will fail because the fluid domains depercolate before the interfacial particle layer jams (we explain this in 3.4.3 and 3.5). Hence, the deviation should not be of major concern.

The linear relationship in the case of the NP data confirms the predicted scaling behaviour, but clearly the slope of the NP data is larger than that of the MP data: 6.22(5) compared to 2.47(8). This means that L increases faster with decreasing volume fraction of NPs than it does with MPs. Absolute values of L achieved with the NPs were between 18 and 99 μm for volume fractions between 2.3% and 0.4% respectively.

In order to explain the differences in slope between the NP and MP data, we derive here an expression for the prefactor in terms of bijel system parameters. The total liquid-liquid (L-L) interfacial area stabilized by the NPs (assuming neutral-wetting) is given by

$$A = \frac{\pi r^2 N_{int}}{\phi_{2D}} \tag{3.1}$$

where N_{int} is the number of particles attached at the interface and ϕ_{2D} is the 2D packing fraction of the interfacial particle layer. The number of particles at the interface is given by

$$N_{int} = \alpha N \tag{3.2}$$

in which α is the fraction ($0 < \alpha < 1$) of particles added to the sample which end up attached to the interface, and N is the total number of particles added to the sample,

$$N = \frac{\phi V_{tot}}{\frac{4}{3}\pi r^3} \tag{3.3}$$

where ϕ is the volume fraction of particles and V_{tot} is the total sample volume. Combining these expressions gives

$$A = \frac{3\phi V_{tot}\alpha}{4\phi_{2D} r} \tag{3.4}$$

$$L \propto \frac{C\phi_{2D}}{\alpha}\frac{r}{\phi} \tag{3.5}$$

where C is a geometrical prefactor. This derivation demonstrates that the magnitude of the slopes in Figure 3.2 are directly related to the magnitude of the prefactor $C\phi_{2D}/\alpha$. The larger slope resulting from the use of NPs implies a higher 2D packing fraction, a lower particle uptake, or both (assuming a constant geometrical factor). If we take the range of possible 2D packing fractions for the arrested interfacial structure to be between the random-close-packed (RCP) value of ≈ 0.83 and the hexagonal close packed value of ≈ 0.91 and note that the prefactor has roughly doubled in magnitude, we must attribute at least the majority of this increase to a decreased particle uptake (smaller α for the NPs), as the 2D packing fraction only varies by $\approx 10\%$.

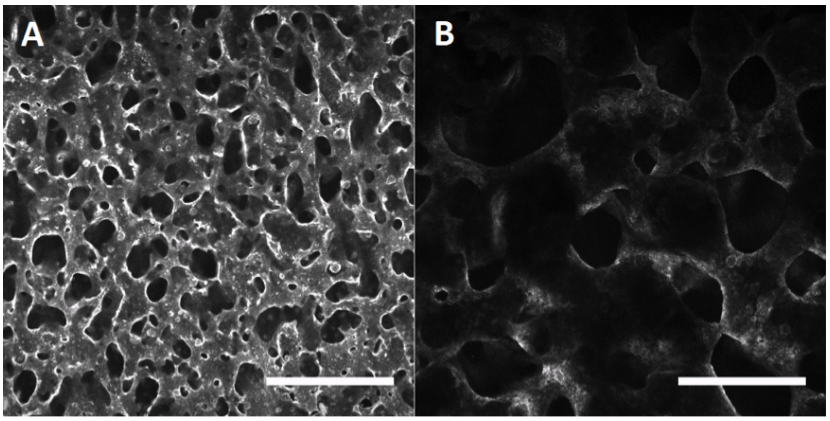

Figure 3.3: Fluorescence confocal microscopy images showing the signal from the FITC-labelled particles, indicating the presence of NPs (A) and MPs (B). Scale bars 200 μm. The NP-stabilized bijel image (A) shows greater signal from non-interfacial areas than the MP-stabilized bijel image (B), supporting the assertion that the interfacial uptake of NPs is less than that of MPs.

To provide direct evidence that the majority of the increased prefactor indeed derives from a lower particle uptake of NPs vs MPs, we compare typical examples of confocal micrographs only showing the fluorescence signal from the FITC-labeled MPs and NPs (Figure 3.3). This comparison at least agrees with a larger

fraction of NPs (compared to MPs) not having attached to the L-L interface, i.e. it is easier to distinguish channels in Figure 3.3A than it is in Figure 3.3B. The original simulations involving NPs of radius $r \approx 5$ nm also showed unattached (free) particles, so this is not an unexpected phenomenon [5], although simulations have so far not investigated how particle size affects the number of free particles. In addition, the interfacial attachment energy [4] ($E \propto \gamma r^2$) is an order of magnitude smaller for NPs, which means that irreversible particle attachment will begin at a later stage in the quench. In other words, NPs will begin attaching to the liquid-liquid interface with a larger separation (L) than MPs [117]. Hence, for the NPs, $L >> r$ (also evident from Figure 3.2), meaning that there will be a significant amount of particles residing between interfaces which never get picked up by it as the system phase-separates. In short, the larger gradient of the NP data presented in Figure 3.2 can be explained by a lower NP uptake due to a smaller attachment energy scale.

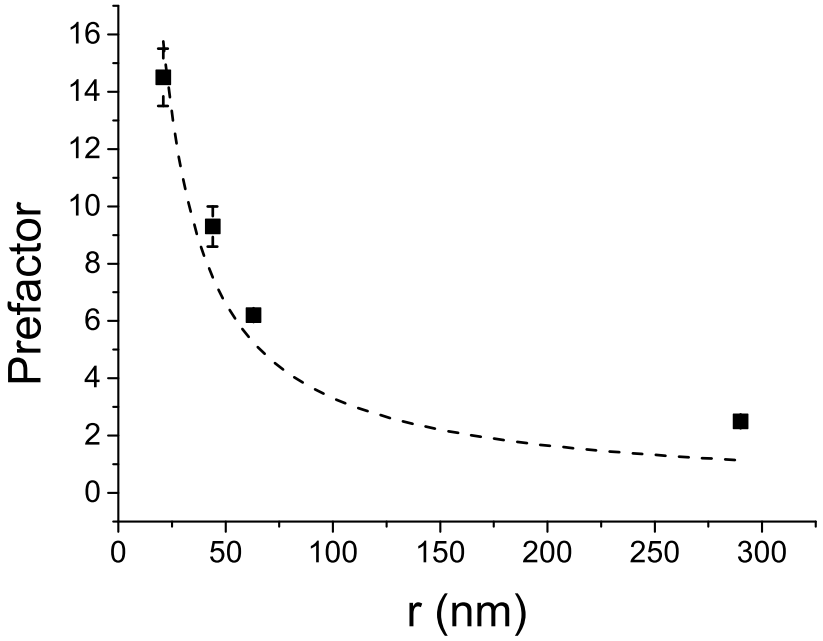

Figure 3.4: The prefactors in the scaling relationship $L/r \propto 1/\phi$ as a function of particle size. The dashed line is a fit to the data using a function of $y = 331/x$ (empirical line of best fit). The inverse relationship, obvious for $r = 63$ nm and below, essentially negates any potential reduction in L (at constant volume fraction) upon reducing r.

This thermodynamic argument suggests that if we reduce particle size even further, we might reach a point where the lengthscale reduction offered by the reduction in r is offset by the change in uptake fraction α. To test this, we prepared smaller Stöber silica particles of radius $r = 44$ nm and 21 nm and used

them to make W/L bijels using the same procedures. We then measured the lengthscale and calculated the value of the prefactor in the scaling relationship (i.e. prefactor = $L\phi/r$). Figure 3.4 shows how the prefactors vary as a function of particle size. The prefactors for the 290 nm and 63 nm particles are the ones derived from the analysis presented earlier in Figure 3.2. The dashed line in Figure 3.4 is a fit to the data using the function $y = 331/x$, demonstrating the inverse relationship between the prefactor and the particle size, more obvious from $r = 63$ nm and below. In the ideal case for stabilizing bijels, the data would be a flat line showing no change in prefactor with particle size. What this result demonstrates is that there is an effective limit on the size of particles we can use with these experimental protocols to reduce L even further, as predicted by our thermodynamic argument.

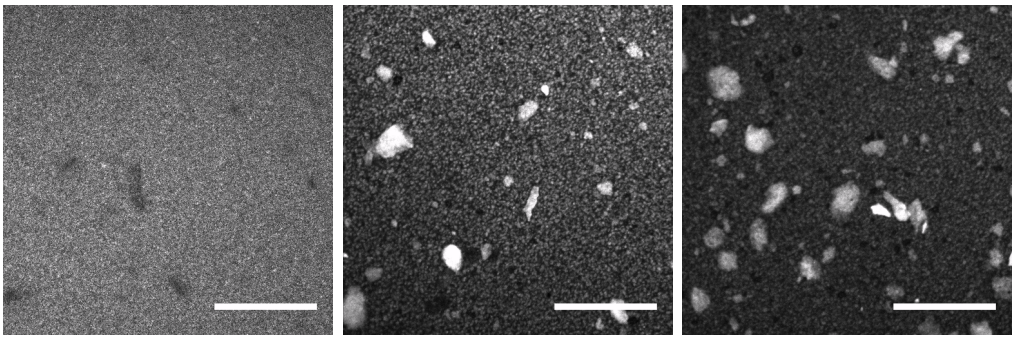

(a) **(b)** **(c)**

Figure 3.5: Confocal images of colloidal dispersions made with r = (a) 63 nm, (b) 44 nm and (c) 21 nm particles and identical sonication procedures (see Chapter 2). The signal is due to the fluorescence of FITC (63 nm) and RITC (44 nm and 21 nm). The 44 nm and 21 nm particles form large aggregates which are difficult to disperse, which may explain the lower fraction of interfacial attachment.

To illustrate, consider the following. By swapping 290 nm particles for 63 nm particles at constant volume fraction, we would expect L to be reduced by a factor of $290/63 = 4.6$. However, because the uptake fraction of the 63 nm particles is smaller, and hence the prefactor is double that of the 290 nm particles, the lengthscale is only reduced by a factor of about 1.8. So, we achieve a reduction of L at constant volume fraction, but a smaller reduction than that predicted by the simple scaling relationship $L \propto r/\phi$. Now, if we replaced the 44 nm particles with 21 nm particles at constant volume fraction, we would expect L to be reduced by a factor of $44/21 = 2.1$, but again because of a concomitant change in the prefactor we only reduce L by a factor of 1.3. A similar scenario arises when swapping 63 nm for 44 nm.

Although these results confirm the prediction of the thermodynamic argument, the origin of the reduction in α may not be completely due to thermodynamics. Figure 3.5 shows confocal images of the colloidal dispersions before they were quenched, with r = (a) 63 nm, (b) 44 nm and (c) 21 nm. The dispersion quality reduces with particle size. Hence, some of the reduced interfacial uptake could be because the particles aren't completely dispersed, as some of them are present in the mixture as large aggregates, as shown in Figure 3.5 (b) and (c).

The largest volume fraction of 63 nm NPs reported here is 2.3%, resulting in $L = 18$ μm. This is the L value achieved with 4% of 290 nm MPs in Ref. [6] – hence, we have demonstrated that NPs can be used in smaller amounts to stabilize bijels with the same pore size (an advantage in itself). In principle, if we increased the volume fraction of 63 nm NPs to 10%, this would achieve a pore size of ≈ 5 μm. Attempts were made to increase the volume fraction above 2.3%, but increased sonication time was needed to ensure proper redispersion, which also changed the particle wettability during the fabrication procedure, requiring a retuning of drying times. Due to time constraints, volume fractions greater than 2.3% were not realized, though volume fractions up to 10% are likely possible given work with NM/ED bijels [36] (although theses samples cannot be feasibly polymerized). It is our opinion that this would be possible, after further rational modification of existing protocols. Note that for the remainder of this chapter we focus on bijels stabilized with NPs of $r = 63$ nm and MPs of $r = 348/367$ nm.

3.4.2 Bijel stabilization: MPs vs NPs

To further demonstrate the difference between NPs and MPs in bijel formation, we first prepared W/L mixtures containing either NPs or MPs, designed to yield similar characteristic lengthscales L, and quenched the samples at different rates. Figure 3.6 presents a confocal microscopy overview of the structures obtained for three different quench rates. In all panels, FITC labeled particles (yellow) appear at the liquid-liquid interface between the water-rich phase (black) and the Nile Red labeled lutidine-rich phase (magenta). Samples prepared with MPs only show the tortuous structures for fast quenches (Figure 3.6E and F), whereas slow quenches result in (deformed) droplets (Figure 3.6D). In contrast, all quenches with NPs yield a percolating interface with changes in the direction of curvature, which is an imperative characteristic of a bijel, with the slower quenches resulting in a relatively higher number of thin necks.

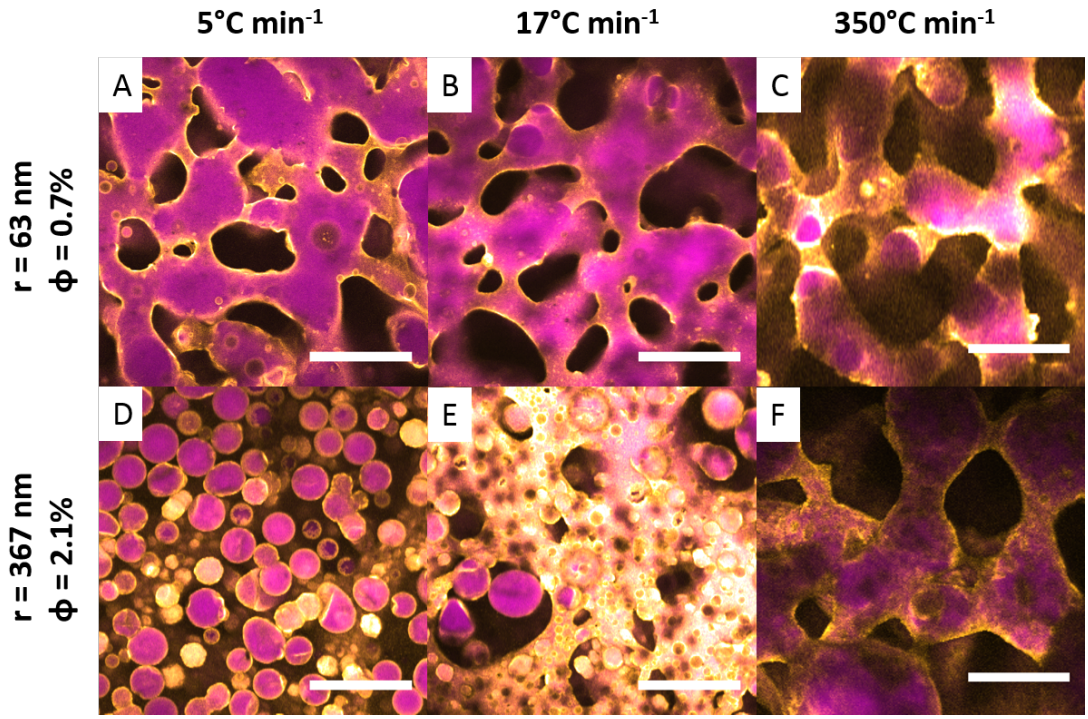

Figure 3.6: Fluorescence confocal microscopy images of the structures obtained when water-lutidine (W-L) mixtures are quenched at various rates in the presence of neutrally-wetting Stöber silica nanoparticles (NPs) of radius 63 nm (A, B and C) and microparticles (MPs) of radius 367 nm (D, E and F). Note the loss of tortuousity for the slow quench and MP combination in D. Scale bars: 100 μm. Yellow: particles labeled with the fluorescent dye FITC. Magenta: L-rich phase labeled with the fluorescent dye Nile Red.

In addition, we scanned the quickly quenched (350°C/min) samples to analyse their homogeneity, in case temperature gradients and/or heterogeneities in the bijel structure could explain the observed differences. Figure 3.7 shows confocal microscopy images from three randomly chosen locations on the samples of a MP stabilized bijel (a) - (c) and a NP stabilized bijel (d) - (f). Magenta identifies the signal from the L-rich phase, and yellow identifies the signal from the particles. Figure 3.8 shows the corresponding radial distributions functions (g(r)). There are both slight qualitative and quantitative differences across the samples, but none big enough to account for the differences observed in Figure 3.6. Note the definite change in shape (especially after the first minimum) in the g(r)s between the MP and NP samples, which suggests some difference in shape not characterized by L – we explore this more in Chapter 4 by measuring distributions of interfacial curvatures.

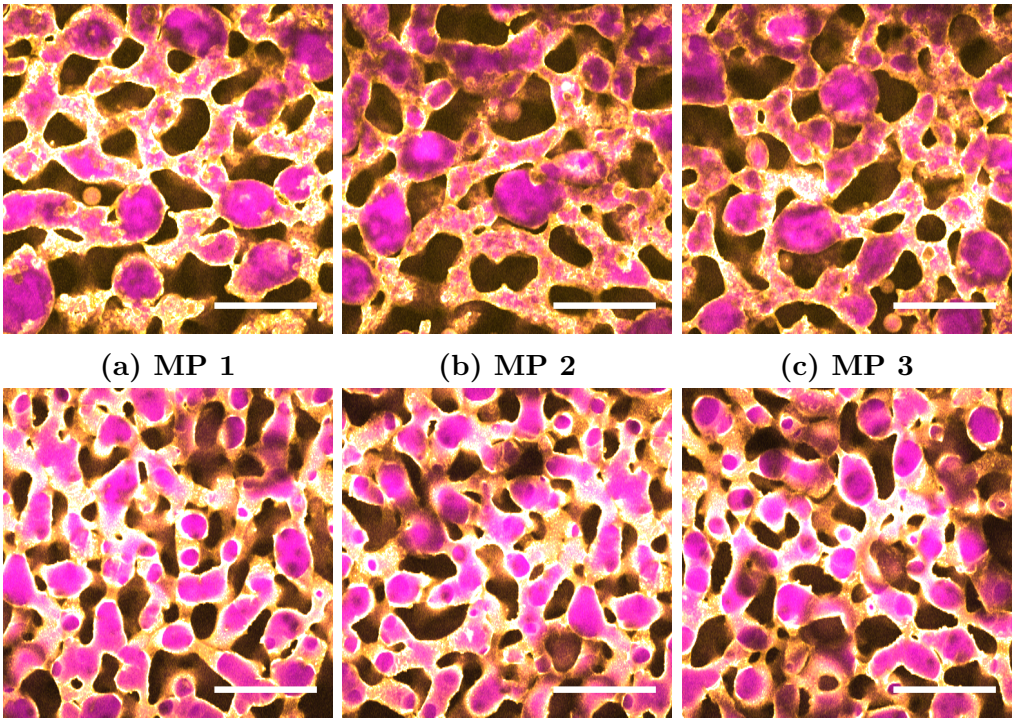

(a) MP 1 (b) MP 2 (c) MP 3

(d) NP 1 (e) NP 2 (f) NP 3

Figure 3.7: Fluorescence confocal microscopy images of water/lutidine (W/L) bijels (lutidine-rich phase is magenta) stabilized by nearly neutrally wetting particles (yellow), quenched at 350°C/min using the microwave method. Images are of a microparticle (MP) (a-c) and nanoparticle (NP) (d-f) stabilized bijel at three different positions (randomly chosen). Particle volume fractions are (a-c) 2.6% and (d-f) 0.7%. Scale bars 200 μm.

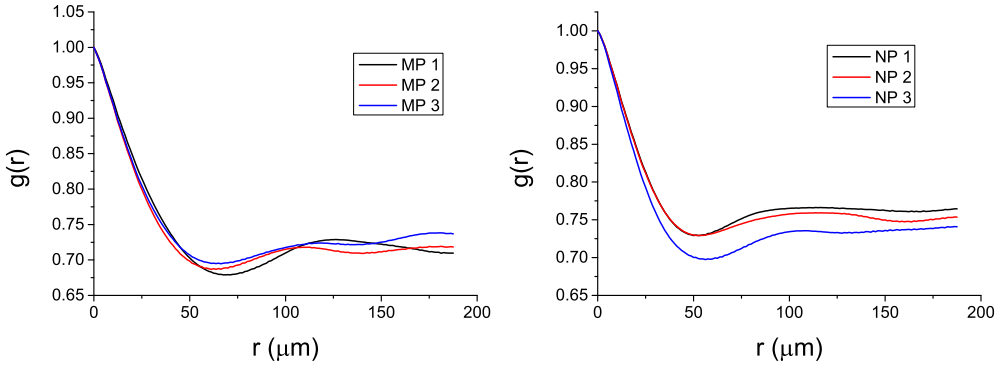

(a) MP (b) NP

Figure 3.8: The radial distribution functions of the confocal images shown in Figure 3.7

3.4.3 Kinetics

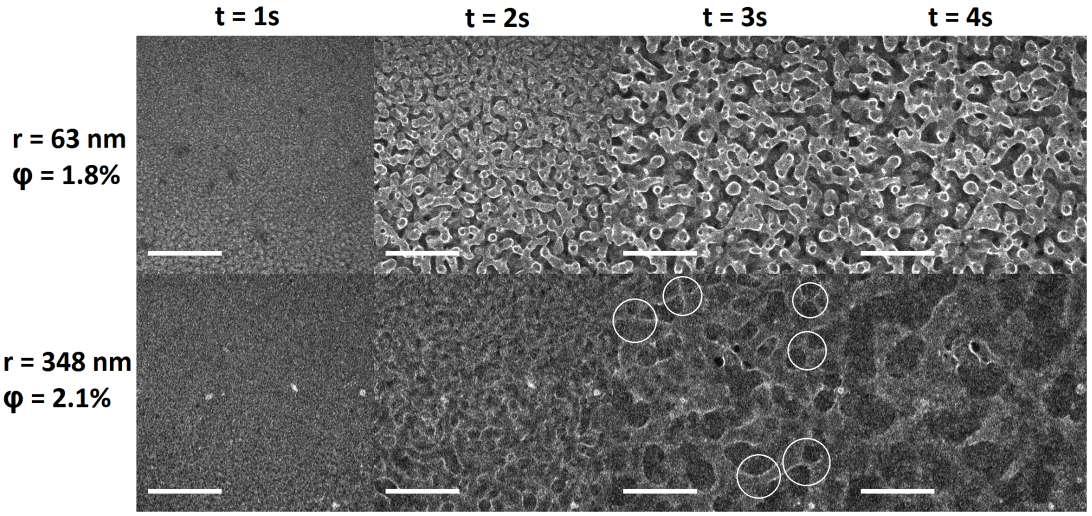

Figure 3.9: Fluorescence confocal microscopy images of the time evolution of water/lutidine mixtures containing nanoparticles (NPs, top row) and micro-particles (MPs, bottom row) under a slow 1°C/min quench. Note the formation of a bijel in the top row and the formation of a droplet emulsion in the bottom row, suggesting that particle size has an important effect on phase-separation kinetics. White: FITC-labelled particles. Scale bars: 100 μm

Now we compare the kinetics of bijel formation by MPs and by NPs, in an attempt to explain the discrepancy in the structures obtained after slow quenches (Figure 3.6). Figure 3.9 shows selected confocal micrographs from time-series of slow quenches (1°C/min) in the presence of NPs (top row) vs MPs (bottom row). Using NPs has clearly modified the phase separation kinetics. In the MP case, the inter-connected domains present at t = 2 s have pinched off by $t = 4$ s, resulting in a droplet emulsion rather than a bijel. We have identified six occurrences of pinch-off using the circles in the $t = 3$s, $r = 348$ nm panel. When using NPs, the connectivity is maintained throughout the quench up and until the structure is arrested. Note that quenching faster (17°C/min) yields inter-connected structures in both systems (Figure 3.6). What this has revealed is that MPs fail to produce bijels at slow quench rates because fluid necks are pinched-off before the interfacial particles can jam and lock-in the structure.

Note that the volume fractions used to produce Figure 3.9 theoretically result in different final lengthscales (i.e. the ratio r/ϕ is not the same); to discount the possible effect of the final lengthscale on the kinetics, we prepared a NP sample with $\phi = 0.7\%$ at 1°C/min which should give a similar L as MP $\phi = 2.1\%$ [1].

This sample resulted in a bijel, revealing that it is unlikely that the cause of the NP success vs the MP failure is not due to the smaller r/ϕ ratio.

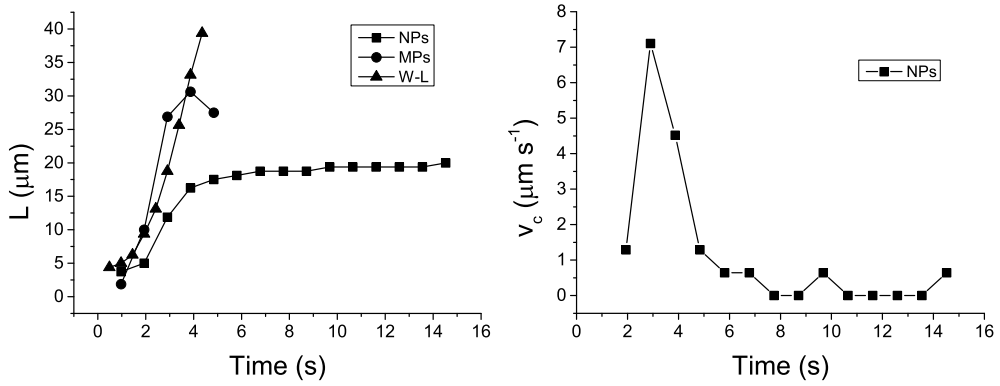

(a) **(b)**

Figure 3.10: (a) The characteristic lengthscale L as a function of time from the onset of the phase separation, for 1°C/min quench of water/lutidine without particles, and with MPs and NPs. (b) the phase separation speed v_c as a function of time from the onset of phase separation in the case of NPs.

To quantitatively compare the coarsening behaviour, the image analysis method was applied to each frame in the MP and NP timeseries along with a timeseries of only the W/L mixture, to produce the data shown in Figure 3.10(a). We also define a phase separation speed

$$v_c = \frac{L_{t_i} - L_{t_{i-1}}}{t_i - t_{i-1}} \tag{3.6}$$

which is shown or the NP system in Figure 3.10(b).

The MP coarsening largely follows that of the W/L mixture without particles until about t = 5s, by which time the bicontinuous structure has broken down and particle-stabilized droplets are formed. The NP coarsening also largely follows the W/L coarsening, but levels off after about 4s. Note that v_c has a maximum at $t \approx 3$ s and slows to zero after $t \approx 7$ s. We will discuss this result in section 3.5 and refer to this time interval as the jamming time Δt_j.

3.4.4 Post-processing and monogelation

To demonstrate the potential of our approach for fabricating bicontinuous polymer composites with sub-micron pores, we post-processed the NP-stabilized

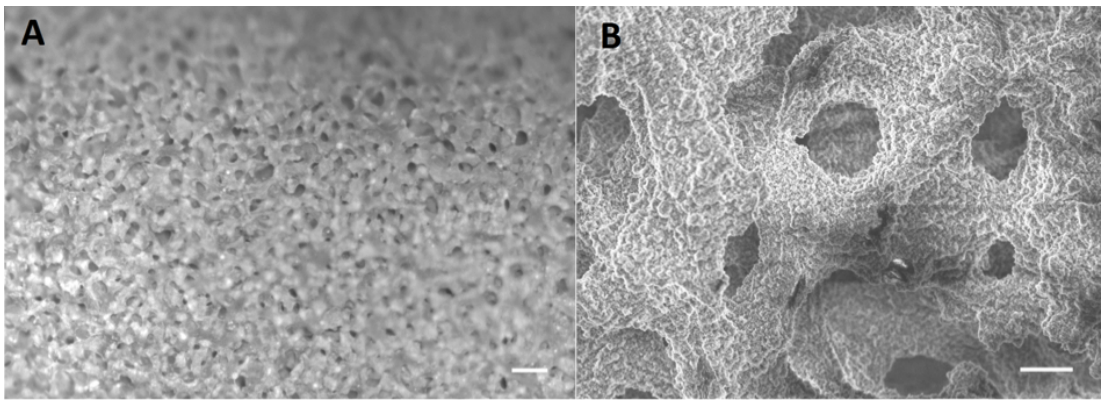

Figure 3.11: (A) Optical microscopy image of a polymer monolith fabricated from a NP-stabilized bijel template. Note the network of tortuous pores and sample homogeneity. (B) Electron micrograph of a polymerized bijel. Scale bar: (A) 100 μm and (B) 10 μm.

bijels following a similar procedure to that already reported for MP-stabilized bijels [54]. Figure 3.11 shows an optical and an electron micrograph of a polymerized bijel. The NP-stabilized bijels allowed us to produce polymer monoliths of higher quality (i.e. increased homogeneity over a larger volume of sample) and were found to be less sensitive to processing parameters like quench rate and temperature gradients.

Another advantage of NP-bijels is that there was a significantly shorter waiting period between the bijel formation and the formation of a colloidal gel ('monogel') at the L-L interface [91], which has been shown to be crucial in allowing the interfacial structure to withstand the mechanical stresses of the monomer diffusion, prior to the polymerization reaction which results in the polymer monolith [90]. In the MP-bijel case this can take as long as forty minutes, whereas in the case of NP-bijels, we observe it to occur much quicker, < 1 minute.

To provide evidence for this, Figure 3.12 shows confocal images of an MP-bijel and NP-bijel post-quench (a,c) and post-cooling to room temperature after a 5 minute waiting period (b,d). In the MP case, the particles largely redisperse, as indicated by the flooding of the image by the yellow signal (arising from the FITC-labelled particles). In the NP case, the particle network remains practically unperturbed, with the magenta signal flooding the image, indicating the removal of the L-L interface and the return of the system to a single (mixed) phase (see Figure 2.6). Although the quench rates used are slightly different and the bijel lengthscale is much smaller in the NP-bijel case, these results are typical of our experience with W/L bijels at large – an incubation period of 30-40 minutes is

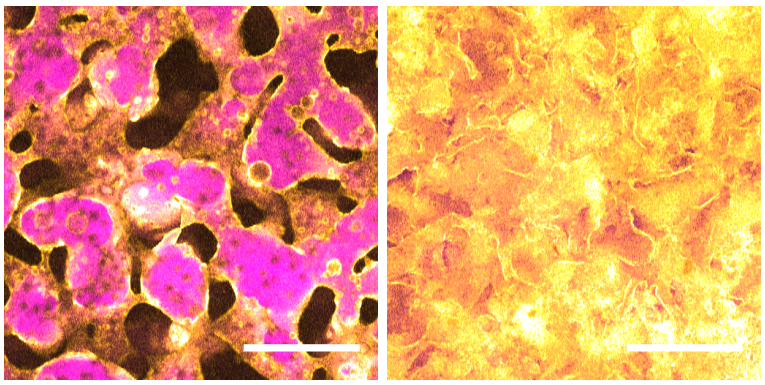

(a) MP 17°C/min (b) RT after 5 minutes

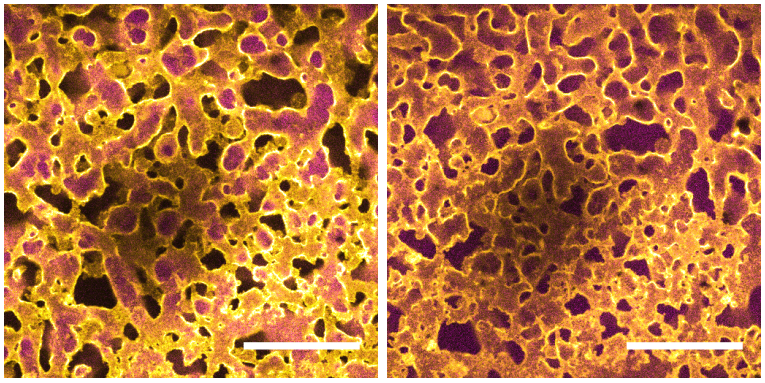

(c) NP 5°C/min (d) RT after 5 minutes

Figure 3.12: Confocal images of a microparticle (MP, $r = 348$ nm, $\phi = 2.2\%$) bijel quenched at 17°C/min (a) and a nanoparticle (NP, $r = 63$ nm, $\phi = 1.4\%$) bijel quenched at 5°C/min (c). Yellow denotes particles and magenta the lutidine-rich phase, or single mixed phase in (d). (b) and (d) are images of the system after cooling to room temperature (RT) when the interface is dissolved. Scale bars 200 μm (a,b) and 100 μm (c,d).

required for monogel formation in a MP-bijel, and a NP-bijel will have formed a monogel in the time it takes to quench and immediately cool to room temperature.

Our finding that the NP-bijels form a monogel quicker and are less sensitive to the quench rate has important implications. Scaling up the polymerization technique is now in principle an easier task, since we have improved the robustness against temperature gradients by using NPs instead of MPs. In addition, we have increased the range of accessible L values (pore sizes), and should be able to achieve about 1 mum pores with the current system, although NP re-dispersion may become a challenge at considerably lower length scales (i.e. higher ϕ).

3.4.5 5nm particles

Here we discuss our attempts to stabilize bijels with $r = 5$ nm silica particles and the modifications to the fabrication procedures required for particles of that size. These results are preliminary in nature but we include them here for completeness and to inform future work.

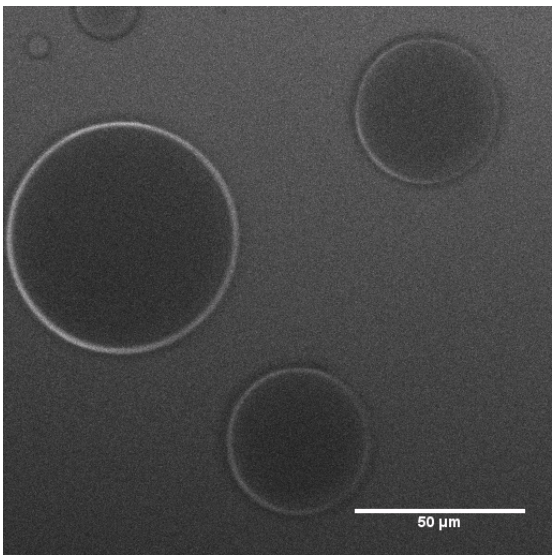

Figure 3.13: Confocal image of a lutidine and water emulsion stabilized by slightly hydrophobized Stöber silica particles with $r = 5$ nm. Note that the type of emulsion (W/L or L/W) is not known because only the particles are dyed. Lutidine was added to a concentration of 28wt%, with the other 72wt% being made up of the silica dispersion in water, i.e. not pure water as in the normal bijel preparation (see Chapter 2). Scale bar 50 μm.

5 nm silica, when dried, is practically impossible to redisperse in the same manner as larger particles due to irreversible aggregation [118]. Hence, we kept the particles in the reaction solution, and removed excess reactants (ethanol and ammonia) via several dialysis steps. Dialysis was performed in ethanol to remove ammonia, then water to remove ethanol. To modify particle wetting, we used hexamethyldisilazane (HMDS) or trimethoxysilane MPPTMS. However, before the appropriate wetting properties could be established, the chemical treatment rendered the colloidal dispersion unstable in water and the particles coagulated. However, we did manage to stabilize W/L and L/W emulsions with the 5 nm particles, treated with a small amount of either HMDS or MPPTMS. The concentrations of the hydrophobizing agents with respect to the particles was hard to ascertain since the volume fraction of particles was not known – in terms

of the mass of particle suspension in water, the amount added was around 0.1%.

Figure 3.13 shows a confocal image of an emulsion formed with 5 nm particles (quenched at 17°C/min), the fluorescence signal arising from the FITC on the particles. The particles appear to be dispersed in both the dispersed and continuous liquid phases, and crucially appear at the droplet interface. The emulsions were stable for c. 15 minutes, indicating either low surface coverage (insufficient for preventing coalescence) or significant particle expulsion/exchange with the bulk fluid (not unreasonable considering the particle size and associated interfacial attachment energy scale [4]). Although spinodal decomposition was not arrested, the resultant emulsion with some stability is encouraging, and suggests that bijel formation could be possible with further modification.

Hence, to realize bijels with 5 nm particles a method of surface treatment is needed which provides both colloidal stability and the correct wetting properties (i.e. $\theta = 90°$) [5]. This could in principle be achieved by using two different steric hairs simultaneously, one hydrophilic and the other hydrophobic. The wetting could be controlled by the relative amounts of these on the surface of the particles. We discuss this further in Chapter 7.

3.5 New theoretical framework

In light of the experimental results (bijels stabilized by NPs or MPs, not the 5 nm particles), a new theoretical framework for understanding bijel formation/failure has been developed in conjunction with colleagues and has been published in Ref. [1]. We repeat here a version of the theory for completeness.

We begin by discussing how bijel formation can fail and how the non-neutrality of the particle wetting can promote bijel failure. Three-dimensional simulations of spinodal decomposition (without particles) in the viscous hydrodynamic (VH) regime are relevant here, and have shown that the depercolation (evidenced in Figure 3.9) proceeds via the thinning of liquid channels followed by pinch-off events [50]. The spinodal decomposition can be halted by neutrally-wetting particles by attaching to and jamming at the liquid-liquid (L-L) interface [5, 6, 64]. However, non-neutrally wetting particles induce a spontaneous curvature C_0 when attached to L-L interfaces [36, 45, 119, 120]. As the coarsening reduces the L-L area, particles are brought in to contact. The spontaneous curvature is induced

because the particle contacts are not situated at the L-L interface. As the L-L interface in bijels have been shown to possess average mean curvature $\langle H \rangle = 0$ [2, 90], we expect that any $C_0 \neq 0$ will disrupt bijel formation.

Note that the above-mentioned simulations did not observe secondary nucleation, i.e. the formation of new droplets during the spinodal decomposition [5, 45, 50]. This is presumably due to the quench being instantaneous in the case of a simulation, whereas during an experiment the quench rate is always finite [75]. Secondary nucleation has been observed in previous experimental studies but it has not been suggested that secondary nucleation is responsible for bijel failure. Instead, the result is the occurrence of droplets inside channels [6] or even droplet-reinforced channels [75].

Our results show that even when MPs and NPs are designed to have similar wetting properties, under slow heating bijel formation only succeeds with the NPs. One (simple) possible explanation is that the contact angle of the NPs are closer to 90° than the MPs. However, this explanation does not fit with our observation that NPs can form bijels over a wider range of drying times than MPs, which is expected to correspond to a wider range of contact angles [68]. The fluorescence confocal timeseries suggest that the bijel failure with MPs is due to depercolation via pinch-off events. These pinch-off events may also occur with NPs as observed in simulations of successful bijel formation [5]. However, we argue that the pinch-off events are sufficiently suppressed by the NPs to allow successful bijel formation.

In order to proceed, we consider the particle-size dependence of the driving force F toward a spontaneous curvature C_0 (see Appendix A for the derivation), i.e. away from an average mean curvature $\langle H \rangle = 0$ for bijels [2, 54] (see also Chapter 4). The bending-energy density of the particle-laden interface is

$$w = 2\kappa(H - C_0)^2, \tag{3.7}$$

where κ is the effective bending modulus of the interface [121, 122], so

$$F = \frac{\partial w}{\partial H} = -4\kappa(C_0 - H). \tag{3.8}$$

Dimensional analysis suggests that $C_0 \propto -1/r$ and $\kappa \propto \gamma_{\mathrm{WL}} r^2$, which is supported by analytical calculations for spheres on a spherical cap [119]. As in the present

case we have $L_f \gg r$ so $|H| \sim 1/L_f \ll |C_0|$, we approximate Equation 3.8 as

$$F \approx -4\kappa C - 0 \propto \gamma_{WL} r. \tag{3.9}$$

Thus, NPs demand a more strongly curved interface ($C_0 \propto -1/r$) but the driving force towards that curvature is smaller ($F \propto r$).

To assess how this smaller driving force can facilitate bijel formation, we compare the disruption time Δt_d to the jamming time Δt_j. For bijel formation to succeed, $\Delta t_j < \Delta t_d$. For the NPs, we can estimate the jamming time from Figure 3.10(b). We define the jamming time $\Delta t_j = t_f - t_{in}$, where t_{in} is the time at which the jamming starts to cause a decrease in the coarsening speed (i.e. the peak in Figure 3.10(b)) and t_f is the time just before the coarsening speed drops to zero. For a quench rate of 1°C/min, this gives $\Delta t_{j,NP} \approx 4$ s.

Obtaining the jamming time directly for the MPs is not possible at this quench rate since bijel formation fails (i.e. the system never jams). However, we expect the jamming dynamics to be determined predominantly by the instantaneous area-fraction of interfacial particles, which is independent of particle radius as long as the final lengthscale L_f is fixed (Appendix A). As L_f (MP) > L_f (NP) in Figure 3.9 i.e. ϕ_{NP} is 1.8% vs 0.7% in Figure 3.6 and $L_f \propto r/\phi$ [3], we expect $\Delta t_{j,MP} > \Delta t_{j,NP}$.

However, what we can estimate for the MPs is the disruption time, $\Delta t_{d,MP} \approx 2$ s from the occurrence of pinch-off in confocal images (Figure 3.9). Although we cannot directly estimate $\Delta t_{d,NP}$, since bijel formation succeeds here, we can predict the scaling of Δt_d with particle radius by balancing the driving and viscous-drag forces to give

$$\Delta t_d \propto \frac{\eta \lambda^2}{\gamma_{WL} r}, \tag{3.10}$$

where η is the bulk fluid viscosity and $\lambda \gg r$ is the typical lengthscale of the disruption, which is independent of particle radius (appendix). Given that the MPs are 4.5× larger than the NPs and assuming that the effects of particle polydispersity and roughness are negligible, the inverse scaling of Δt_d with radius implies that $\Delta t_{d,NP} \approx 9$ s.

These timescale estimates help to explain the observed patterns of bijel failure, i.e. they explain why $\Delta t_{j,NP} < \Delta t_{d,NP}$ but $\Delta t_{j,MP} > \Delta t_{d,MP}$. It is worth noting here that based on the scaling proposed in Equation 3.9, we expect bijel formation with MPs to be successful at 5°C/min, due to it succeeding at similar L_f with

NPs at 1°C/min (and the NPs are about 5× smaller than the MPs). As bijel formation is only barely successful at higher rates of 17°C/min, this suggests that some other mechanisms might be in play, which could be elucidated by future simulations and experiments. Nonetheless, this theoretical framework is able to explain why bijel formation is more robust when using NPs rather than MPs.

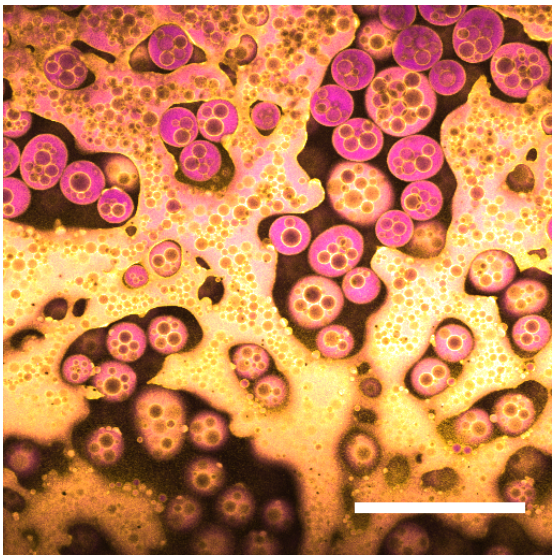

Figure 3.14: Confocal image of a microparticle (MP, $r = 348$ nm) stabilized emulsion ($\phi = 4.5\%$) formed by quenching at 1°C/min. Some tortuousity remains at this high volume fraction, but not enough for the sample to be considered a bijel. Scale bar 200 μm.

One potential route to preparing MP stabilized bijels with slow quenches is to increase ϕ, thereby decreasing the jamming time $\Delta t_{\mathrm{j,MP}}$ because the particles are able to take up a larger area of L-L interface. Figure 3.14 shows a confocal image of a MP stabilized emulsion with $r = 348$ nm, $\phi = 4.5\%$ and a quench rate of 1°C/min. Some tortuousity from the spinodal pattern is retained, however the sample is clearly not a bijel. Increasing ϕ further to 10% may result in a sample with greater resemblance to a bijel, but it is clear that preparing bijels with slow quenches using MPs is not practical and would result in only a small range of lengthscales being accessible. However, this high volume fraction test demonstrates the effect of the jamming time on bijel formation success or failure.

3.6 Conclusions

In this Chapter, we have demonstrated that the formation of water/lutidine (W/L) bijels is more robust when using nanoparticles (NPs, $r = 63$ nm) as

opposed to microparticles ($r \approx 300$ nm), because they are less sensitive to the temperature quench rate used. The scaling behaviour of the characteristic lengthscale L with particle size has been confirmed, albeit with the caveat that the NPs are less efficient stabilizers than MPs which is likely due to a reduced fraction of added particles ending up on the liquid-liquid (L-L) interface. This assertion is corroborated by confocal images showing an increased fluorescence signal from the lutidine-rich channel (where the unattached NPs reside). Nonetheless, the use of NPs paves the way for $L \approx 1$ μm as long as ϕ can be increased towards 10%. Reducing particle size below 63 nm did not result in any substantial reduction in L (at constant volume fraction), due to the uptake fraction α reducing at the same rate as r, which may in turn be due to the difficulty of redispersion. Hence, to reduce particle size further, a new approach is needed, possibly using steric stabilizers.

By analyzing confocal timeseries of the L-L phase separation in the presence of MPs or NPs, we have seen that when they are quenched slowly (1°C/min) the MP system depercolates into droplets whereas the NP system jams and forms a bijel. To take account of this we developed a new theoretical framework based on lipid membranes which characterizes the system in terms of the 'jamming time' Δt_{j} and 'disruption time' Δt_{d} – as long as $\Delta t_{\mathrm{j}} < \Delta t_{\mathrm{d}}$ then bijel formation will be successful.

We have attempted to use particles of radius $r = 5$ nm by keeping them in solution and modifying their wetting properties using chemical agents. However, increasing the hydrophobicity of the particles leads to irreversible aggregation. The future use of 5 nm silica particles is therefore dependent on finding a method of providing colloidal stability while simultaneously controlling the wetting properties.

Finally, we have demonstrated that the reduced lower bound on L in this system can be transferred to the polymerized bijel, expanding the applicability of this system for the fabrication of functional materials. Notably, the insensitivity to quench rate, and the fast rate of monogelation provides a distinct materials synthesis advantage of NP-stabilized over MP-stabilized bijels.

Chapter 4

Bijel interfacial curvatures

4.1 Abstract

Bicontinuous Pickering emulsions (bijels) are a physically interesting class of soft materials with many potential applications including catalysis, microfluidics and tissue engineering. They are created by arresting the spinodal decomposition of a partially-miscible liquid with a (jammed) layer of interfacial colloids. Porosity L (average interfacial separation) of the bijel is controlled by varying the radius (r) and volume fraction (ϕ) of the colloids ($L \propto r/\phi$). However, to optimize the bijel structure with respect to other parameters, e.g. quench rate, characterizing by L alone is insufficient. Hence, we have used confocal microscopy and X-ray CT to characterize a range of bijels in terms of local and area-averaged interfacial curvatures; we further demonstrate that bijels are bicontinuous using an image-analysis technique known as 'region growing'. In addition, the curvatures of bijels have been monitored as a function of time, which has revealed an intriguing evolution up to 60 minutes after bijel formation, contrary to previous understanding.

4.2 Introduction

Bijels (bicontinuous interfacially-jammed emulsion gels) are a versatile and relatively new class of soft materials, whereby a bicontinuous interlocking structure of two phase-separated liquids is stabilized by a (jammed) layer of

interfacial colloids [3, 5, 64, 79, 80, 85, 92]. As long as the colloids are sufficiently neutrally-wetting, i.e. have no preference for either liquid phase, the bicontinuous pattern formed by the liquid-liquid (L-L) interface during spinodal decomposition can be maintained and eventually locked in (Figure 1). This is because, during the phase separation, the area fraction of particles increases until they jam, at which point the system stops coarsening [6]. Particle rearrangements could lead to residual coarsening [5], but continued macroscopic coarsening is precluded due to the attachment energy E of the interfacial particles, which for particle radius $r \approx 250$ nm and interfacial tension ≈ 0.1 mN·m^{-1}, is of the order 10^3 $k_\mathrm{b}T$.[4] The bijel lends itself to a host of technological applications, including tissue engineering [56], catalysis [27] and microfluidics [25], owing to its morphology and high degree of structural tunability [3, 5].

The water/lutidine (W/L) bijel has been shown to be a particularly promising system for material templating – one of the fluid phases can be selectively polymerized and, on removal of the unpolymerized liquid phase, results in a bicontinuous microporous monolith [54, 90]. To tune the final structure of the material, samples are usually (and simply) characterized by their porosity, or rather their average interfacial separation ('channel width') L (see Figure 1). L is controlled by varying the volume fraction (ϕ) and radius (r) of the colloids ($L \propto r/\phi$) in the initial bijel mixture. L can be measured by constructing a pixel-based radial distribution function (in real space) from a 2D fluorescent confocal microscopy image of a bijel [1], in which one phase is bright and the other dark (owing to the preference of a fluorescent dye for one of the phases). This method is outlined in Chapter 2.4 and used for analyzing the effect of volume fraction on lengthscale in Chapter 3.4.1. Alternatively, the dominant wavevector q^* can be determined by performing a scattering experiment [123] or by taking the Fourier transform of a 2D bijel image [6] – then $L = 2\pi/q^*$. L in the polymerized case can be extracted from X-ray micro-CT data in a similar fashion, where the contrast is provided by the difference in electron density across the solid/air interface.

Measuring L is relatively straightforward, but does not convey information about local geometrical or global topological parameters which might be useful for optimizing the bijel for applications. Indeed, visible changes in the bijel morphology are noticed when different particle sizes and/or quench rates are used in the fabrication which seem not to be quantified purely by L [1] (see Figure 3.5 in Chapter 3.4.2). Moreover, bijel fabrications produce samples which show a sliding scale of quality (as a function of particle size and quench rate),

with complete failure on one end and homogenous 'clean' samples on the other. It would be beneficial to have a quantitative characterization to accompany these qualitative observations, and hence be able to systematically optimize bijel fabrication procedures.

A complimentary way to characterize complex 3D structures such as the bijel is to measure the distributions of interfacial curvatures [54, 124]. At each point on the interface between the coexisting liquid domains, it is possible to define two mutually-orthogonal principle radii of curvature (see Figure 4.1), R_1 & R_2, and two principle curvatures κ_1 & κ_2 ($\kappa_i = \pm 1/R_i$) [125]. In the current study, the curvature is defined to be positive if the interface curves towards the oil phase, and negative if it curves towards the water phase. The structure can then be characterized [126] by computing the area-averaged mean curvature:

$$\langle H \rangle = (1/A) \int_A \frac{1}{2}(\kappa_1 + \kappa_2) \mathrm{d}A \tag{4.1}$$

and Gaussian curvature:

$$\langle K \rangle = (1/A) \int_A \kappa_1 \kappa_2 \mathrm{d}A \tag{4.2}$$

This characterization allows the bijel's topology to be probed, as opposed to simply extracting a characteristic length (L).

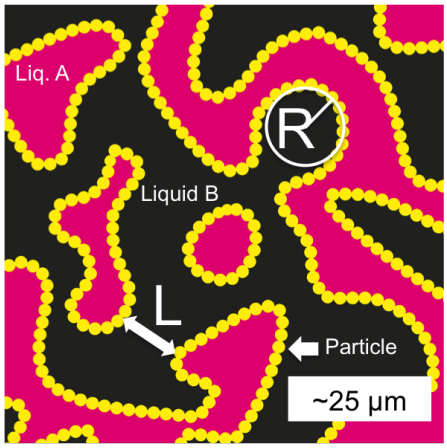

Figure 4.1: A schematic of a 2D slice of a 3D bijel. The liquid phases (A and B) are separated by a jammed layer of particles (yellow) at the interface, with a typical separation L. The principal radius of curvature R at a point on the interface is the radius of a circle which intersects tangentially at that point, with a curvature $\kappa = 1/R$. In 3D a point will have two principal curvatures. Adapted from Ref. [1].

In addition to the practical motivations for the study presented in this Chapter, there are several interesting physics questions to be explored. For example, it is not completely clear whether (neutrally-wetting) particles simply 'lock in' the spinodal pattern of the demixing liquids, or if they perturb it in some way before arresting the phase separation [61]. Any perturbation could also depend on other parameters like particle size and/or contact angle [1, 119]. Moreover, in the W/L system, the interfacial particles are known to form a permanent gel after a certain incubation period [91] – this may or may not have an effect on the morphology. Finally, it is also not known yet if the bijel structure is entirely homogeneous, periodic and/or bicontinuous in three dimensions.

A (small-scale) curvature analysis on a W/L bijel and its polymerized counterpart has already been performed, on one size of particle and one quench rate only, which showed a distribution of mean curvature centred (approximately) on zero, and a negative value for the area-averaged Gaussian curvature, which are similar to the hallmarks of a member of the family of triply-periodic minimal surfaces, the gyroid [54]. This means that the L-L interface is, on average, composed of saddle points, with principal curvatures equal in magnitude but opposite in sign. Bicontinuous systems similar in 3D structure to bijels have also been analyzed in this way. For example, it has been shown that a spinodally-decomposing polymer blend also resembles the gyroid [127]. More recently, a topological analysis has elucidated the mechanisms at play during the phase separation of such polymer blends [128].

In this Chapter, we systematically characterize a range of W/L bijel samples by using 3D confocal microscopy data and a commercially available image analysis package. We benchmark our analysis by using X-ray CT data (with improved statistics over confocal) and computer-generated data representing the two extremes of the range of possible structures in this system (spheres and gyroid); we also compare our results to lattice-Boltzmann simulations of bijel formation. We measure distributions of interfacial curvatures, and then compute area-averaged quantities in order to characterize the topology of the structures as a function of particle size, quench rate, and time after bijel formation. We find that the most hyperbolic samples (i.e. samples with largest negative value of Gaussian curvature) are formed when using the smallest particles and the fastest quench rates, and that in some cases the distribution of local curvatures changes with time, which may be linked to the emergence of a particle-bonded network at the L-L interface.

4.3 Experimental Methods

4.3.1 Particle synthesis

The synthesis procedure for the particles used in this study is contained in Chapter 2. The most relevant aspects are repeated here for the benefit of the reader. Stöber silica particles, labeled with fluorescein (or rhodamine) isothiocyanate (FITC or RITC) were synthesized with different radii by controlling the reaction temperature. Sizes were obtained from dynamic light scattering (DLS) and transmission electron microscopy (TEM) measurements. The three sizes used in this study are $r = 50$ nm (TEM), 80/63 nm (DLS/TEM) and 367 nm (TEM) – polydispersities (in terms of TEM results) were 13.8%, 15.1% and 5.5% respectively. The sizes obtained by TEM will be used in this study to provide a valid comparison. The 367 nm and 63 nm particles were labelled with FITC, and the 50 nm particles were labelled with RITC.

Surface chemistry was designed to be similar by modifying the concentration of dye in the reaction mixture. Neutral wetting conditions were achieved by drying small amounts (≈ 50 mg) at 170°C and 20 mBar pressure [68, 69]. This process is known to remove surface bound water and may also cause moderate dehydroxylation of the silica surface [72]. Wetting properties were maintained across the range of particles used by tuning the drying time and inspecting confocal micrographs of the emulsion structures that they formed. We denote the 50 and 63 nm particles as nanoparticles (NPs) and the 367 nm particles as microparticles (MPs).

4.3.2 Bijel preparation

Bijels were prepared following the standard procedure outlined in Chapter 2. Particle concentrations for the MPs were 2.8%, the 63 nm NPs between 0.6 - 1.8% and the 50 nm NPs 1.4%, producing bijels with lengthscales 21 μm $< L <$ 91 μm. The precise specifications are shown in Table 4.1. The effect of changing the volume fraction is to change the final bijel lengthscale L according to $L \propto r/\phi$ which also changes the range of interfacial curvature values [3]. Where possible, we compare bijels with similar L values. As this is not always possible, we normalize the curvature values with respect to the surface to volume ratio,

Radius (nm)	Vol. frac. (%)	Quench rate (°C/min)
367	2.8	350
367	2.8	350
367	2.8	350
63	0.7	350
63	0.7	350
63	1.0	350
50	1.4	350
63	0.6	17
63	1.0	17
63	2.3	17
50	1.4	17
63	1.8	1

Table 4.1: The specifications of bijel samples prepared for characterization and comparison in this Chapter. The parameter space is such that we can look for the effect of particle size and quench rate on the bijel's curvature distributions (see text).

a quantity with units of inverse length [129]. We also average the results from multiple samples (where possible) to show that the volume fraction does not play a pivotal role in determining the topology of the final structure.

4.3.3 Data acquisition

Experiments

The bijel samples were imaged using fluorescence confocal microscopy, specifically a Zeiss Observer.Z1 inverted microscope with a Zeiss LSM700 confocal scanning unit. Images of dimension 512 × 512 pixels were taken with a 20× or 40× objective (Zeiss LD-Plan NEOFLUAR, NA = 0.4 and 0.6 respectively), giving a pixel size of 1.25 μm or 0.625 μm. Figure 4.2(a) shows an example 2D confocal microscopy image of a bijel. 3D stacks were created by taking up to 60 images in succession with a (nominal) increment in the z-direction of about 1 μm per slice. Signal-to-noise was improved by averaging over 4 to 8 scans of the sample region. The acquisition of a full 3D stack took between 6 and 8 minutes. Fluorescence excitation was provided by a 488 nm laser (for FITC), a 555 nm laser (for Nile Red or RITC), and a 639 nm laser (for Nile Blue). Emission filters were used as appropriate. The two liquid domains could be distinguished by detecting the fluorescence of the Nile Red (or Blue) which preferentially resides in the lutidine-

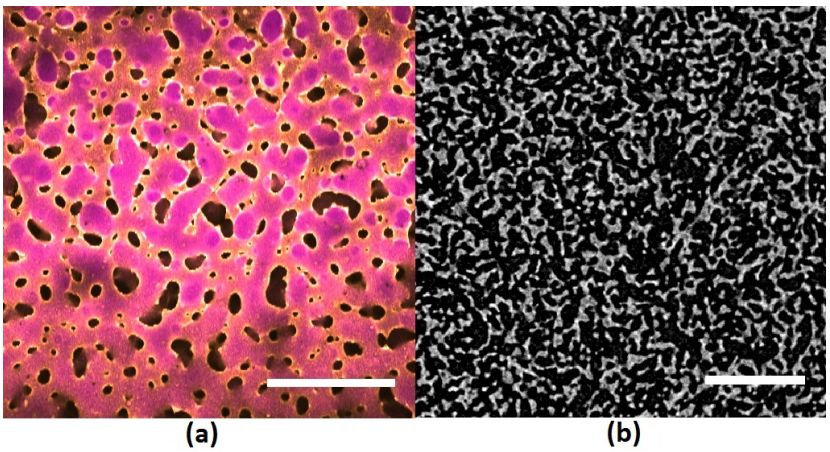

Figure 4.2: (a) Example fluorescence confocal microscopy image of a bijel stabilized by NPs (r = 63 nm), quenched at 17°C/min. Particles are shown in yellow, whereas magenta indicates the lutidine-rich phase. Scale bar 200μm. Z-stacks are compiled by acquiring these 2D (X-Y) images at incrementing Z positions. (b) Example X-ray CT image of a polymerized bijel, where one of the channels is air (black) and the other polymer (white). Scale bar 500μm. Imaging with this method allows a larger sample volume to be probed, providing better statistics than confocal microscopy.

rich phase. To take account of the decrease in image intensity as the focal plane is moved further in to the sample, the histograms of the 3D stacks were equalized (using the stack histogram) in ImageJ version 1.49 [99].

Simulations

Simulations were performed by Dr Kevin Stratford, School of Physics and Astronomy, The University of Edinburgh. Using the same computational machinery as Stratford *et al.* [5], a bijel structure is produced for an idealized case of a pair of fluids with equal density and viscosity. The simulation parameters are matched as closely to the experimental situation as possible for the $r = 63$ nm case and with fluid composition 65:35 by volume. The sample size was approximately $6 \times 6 \times 3$ microns. The simulation was run until the particles jammed at the interface, and the resulting structure was approximately steady. Black and white images with an effective resolution of ≈ 23 nm were generated directly from the simulation data to identify the two fluid phases.

Specifically, we employ a symmetric free energy (e.g., Kendon *et al.* [40]) with

density as a function of composition ϕ is

$$\frac{1}{2}A\phi^2 + \frac{1}{4}B\phi^4 + \frac{1}{2}\kappa(\nabla\phi)^2. \tag{4.3}$$

The parameters A, B, and κ control the fluid-fluid interfacial tension, and also the interfacial thickness. We choose the parameters $A = -B = -0.00025$ and $\kappa = 0.000175$ giving an interfacial tension of $\sigma \approx 1.97\times10^{-4}$ in simulation units. The interfacial width is 1.18 lattice units. Fluid parameters were density $\rho = 1$ and dynamic viscosity $\eta = 0.12$. Neutrally wetting (contact angle 90°) spherical particles with radius $a = 2.3$ lattice units were used. Fluctuating hydrodynamics is used to impart Brownian motion to the particles with effective temperature 2.12×10^{-6} in simulation units. A system size of 256 × 256 × 128 lattice units was used, in which the fluid volume ratio was initialized to 65 : 35 by volume before particles were inserted randomly in the initial condition (32,919 colloids). Spinodal decomposition was initiated via a small-amplitude random noise in the order parameter ϕ.

The simulation parameters – in 'simulation units' – may be matched with the experimental parameters as follows. We assume a simplified experiment with fluids of uniform density 1.0×10^3 kg·m^{-3}, and viscosity 1.0×10^{-3} Pa s, and with an interfacial tension 5.0×10^{-4} N m^{-1} (similar to the water/lutidine system). The characteristic length and time scales for spinodal decomposition are $L_0 = \eta^2/\rho\sigma$ and $T_0 = \eta^3/\rho\sigma^2$. By matching these quantities in experiment and simulation we may equate 1 simulation length unit to 23 nm (a particle radius of 63 nm and system size of 3 μm in the short direction), and 1 simulation time unit to 9×10^{-11} s. Temperature is matched via a dimensionless diffusion constant $6\pi DT_0/L_0^2$: the simulation temperature corresponds to approximately 300 K. The particles were removed from the dataset before analysis.

4.3.4 Image analysis

The 3D data was analyzed using Avizo (FEI Group). An appropriate pixel value threshold was chosen to allow the software to generate an isosurface via the 'Isosurface' module, which represents the interface between the two liquid domains. The isosurface was 'downsampled' (averaged) over a volume of 3 × 3 × 3 pixels to reduce the impact of noise. This produced a more accurate isosurface in terms of its resemblance to the original bijel data (see Figure 4.3), as well

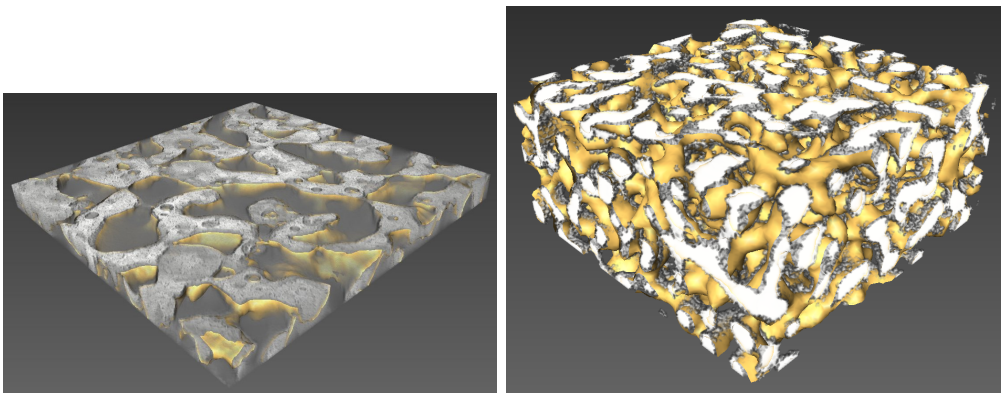

(a) (b)

Figure 4.3: (a) A 3D volume rendering of a microparticle stabilized bijel (greyscale) with the calculated isosurface superimposed (yellow). The isosurface clearly follows the pattern of the raw data, meaning that the curvature analysis performed on the isosurface can be said to represent the curvature values of the raw data, i.e. the bijel. (b) The same for data obtained from a Lattice-Boltzmann bijel simulations with the particles removed.

as reducing the occurrence of surface discontinuities (regions of non-manifold topological structure) on which the measurement of curvature becomes invalid.

The software was then instructed to extract the distribution of mean ($H = \frac{1}{2}(\kappa_1 + \kappa_2)$) and Gaussian ($K = \kappa_1\kappa_2$) curvatures – κ_1 and κ_2 are the principal curvatures ($\kappa_i = \pm 1/R_i$, where R_i are the radii of curvature) at each vertex on the triangulated isosurface. The software achieves this by approximating the isosurface locally (a region spanning 4 orders of connecting vertices in all directions, covering an area of the order 10 μm^2 in a confocal data stack) in quadric form, then computing the eigenvalues and eigenvectors (the eigenvalues being the principal radii of curvature). This function is contained within the 'Compute curvatures' module. The computed curvatures were also averaged over a region spanning 5 orders of adjacent vertices, which reduced the impact of noise further. These specific settings were chosen because they produced the results closest to that expected for our benchmark structure: a simulated gyroid with a similar lengthscale as our bijels in a data volume similar to our confocal stacks - see section 2.6.

Since H and K will naturally vary with the characteristic lengthscale of the structure [126] (smaller lengthscales necessitate larger curvatures) it is necessary to normalize these quantities. This can be done simply by multiplying by the inverse or inverse-square of the surface-to-volume ratio ($\Sigma = A/V$), which can

also be extracted using the software. The reduced dimensionless quantities are therefore $H\Sigma^{-1}$ and $K\Sigma^{-2}$.

To reduce the potential impact of artefacts during the software's reconstruction of the bijel interface (i.e. regions of abnormally large curvature) only curvature values in a certain range were used to calculate the area-averaged quantities. This range was chosen to be around the expected curvatures as derived from the measurement of L, i.e. $|H_{\text{expected}}| \approx 2/L$ and $|K_{\text{expected}}| \approx 4/L^2$. Once the curvature distributions were truncated in this way (resulting in a loss of no more than 5% of the total data), the values were summed to give $\langle H \rangle \Sigma^{-1}$ and $\langle K \rangle \Sigma^{-2}$. Note that this is not the strict calculation of the integral of H or K over the surface required to apply the Gauss-Bonnet theorem [125], but rather the sum of a discrete series of values, without each value being weighted by the area over which the curvature was measured. However, these values still serve as a (scaled) metric to quantify the bijel structure, since it is still sensitive to changes in the distributions. For a bijel, we expect a structure with overall hyperbolic character, $\langle H \rangle \Sigma^{-1} \approx 0$, and $\langle K \rangle \Sigma^{-2} < 0$, although $\langle H \rangle \Sigma^{-1}$ may take a finite value close to zero if the volume ratio between the two phases is not 50:50 [126], as is the case in the W/L system employed here [8] (see Figure 2.6).

An alternative way to probe bicontinuity in our structures, using the same 3D data stacks, relies on an image segmentation method known as 'region growing'. 3D X-ray CT data stacks were opened in ImageJ (version 1.49v) [99], thresholded, and region growing was performed on channel A (high pixel values) using the ImageJ 'Find Connected Regions' plugin, with the following settings: diagonal connections not allowed and start from point selection. This procedure was repeated after inverting the image stack to perform region growing on channel B (originally low pixel values). The number of pixels *not* connected to the grown region was calculated by subtracting the grown region from the thresholded original and extracting the mean grayvalue of the difference stack.

4.3.5 Errors

The threshold value used to create the isosurface most closely resembling the raw data (assessed by visual inspection) was the one which also maximized the area of the isosurface. For comparing curvatures across a range of samples therefore, the threshold value for the maximum area was found, and those curvature values recorded. To take account of sampling error, the entire procedure (from sample

Location	Magnification	$\langle K \rangle \Sigma^{-2}$	$\pm$
A	20×	-0.50	0.06
B	20×	-0.49	0.08
C	40×	-0.50	0.01
D	40×	-0.49	0.01

Table 4.2: The results of a curvature analysis performed on a nanoparticle stabilized bijel quenched at 350°C/min, sampled at four different positions (A-D) and using two different objectives (20× and 40×). Samples showed good internal consistency, with the only effect of changing objective being a reduced thresholding error.

preparation, to data acquisition, to image analysis) was repeated three times, and an average of quantities taken. Note that this also means that our results are unlikely to be significantly affected by small wetting differences between batches of dried particles. Where repeat sampling was not feasible (e.g. not enough identical material being available) the threshold value was varied around that which gave the maximum area, and an average of those curvature values taken. Hence, the error bars on these data points represent the thresholding error in the measurement of one sample. It will made clear in the following sections which data points have been multiply sampled and which have not. Also, the thresholding error was found to decrease when using a 40× objective rather than a 20× objective, but that the absolute curvature values were not affected – see Table 4.2. This can be understood as due to the increased lateral and axial resolutions as explained in Chapter 2.3.2.

Another source of error is due to the 'fishtank' effect, whereby the position of the focal plane moves either more or less than the nominal Z increment depending on the relative refractive indices of the sample medium and the medium surrounding the collection optics. In this case, by using the average refractive index of the water/lutidine mixture [8] ($n_{\mathrm{WL}} \approx 1.4$), and the refractive index of the collection medium (air, $n_A \approx 1$) the correction is calculated to be $n_{\mathrm{WL}}/n_A = 1.4$ times the nominal Z difference [130]. Therefore, the analysis has also been tested on the stretched data, by modifying the voxel sizes specified when loading the data into Avizo. We found that the fishtank effect, while slightly modifying the absolute numbers, did not significantly affect the trends in the data (see Figure 4.5 and Appendix B).

4.3.6 Benchmarking

Simulated spheres and gyroid

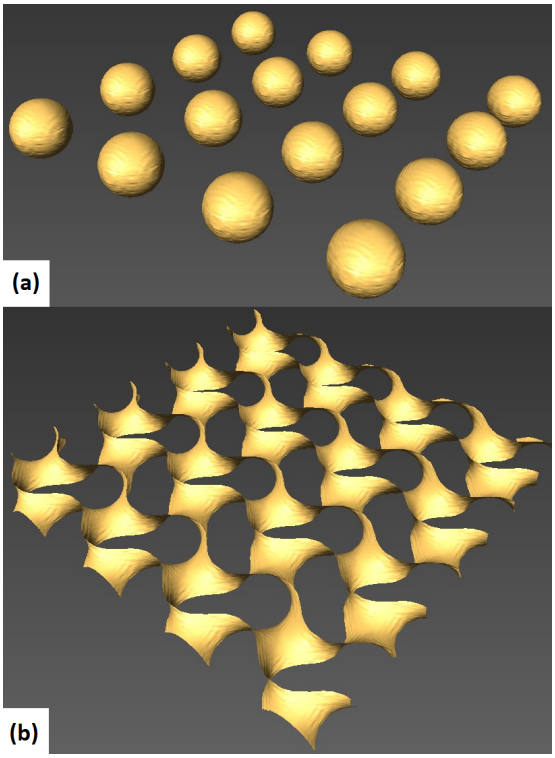

Figure 4.4: Isosurfaces computed for benchmark structures, system of spheres (a) and a gyroid (b). Matlab was used to numerically generate these structures (see text for details).

In order to test the ability of the analysis method to accurately probe the topology of our bicontinuous structures, we generated idealized structures (representing the two possible extremes) with similar pixel sizes, lengthscales and box sizes as the real data. Benchmarking our analysis in this way also provided us with an appropriate scale for our dimensionless area-averaged curvature values. On the one hand, a system of spheres was generated as shown in Figure 4.4(a). On the other hand, a gyroid structure (Figure 4.4(b)) with roughly the same characteristic lengthscale and dimensions as the bijel data was generated by using the following equation [127, 131];

$$f(x,y,z) = \sin\frac{2\pi x}{\lambda}\cos\frac{2\pi y}{\lambda} + \sin\frac{2\pi y}{\lambda}\cos\frac{2\pi z}{\lambda} + \sin\frac{2\pi z}{\lambda}\cos\frac{2\pi x}{\lambda} \qquad (4.4)$$

Here, λ is the characteristic wavelength, which in terms of bijel structure, is twice the interfacial separation L. To create the dividing surface, $f(x,y,z)$ is set to

Test	$\langle H \rangle \Sigma^{-1}$ E/M/Err	$\langle K \rangle \Sigma^{-2}$ E/M/Err
Spheres, $r = 32$ pixels	5.05/4.78/5.3%	25.5/22.9/10%
Gyroid, $\lambda = 128$ pixels	0/0.00/0%	-1.7/-1.66/2.4%

Table 4.3: The results of the analysis test on the benchmark structures shown in Figure 4.4. Expected (E) and measured (M) values are shown, along with a relative error (Err).

zero [129]. To reiterate, we choose these structures because a bijel is expected to have $\langle H \rangle = 0$ and $\langle K \rangle < 0$ (i.e. the same as a gyroid), whereas a system of spheres has $\langle H \rangle > 0$ and $\langle K \rangle > 0$.

Table 4.3 shows the expected (E) and measured (M) values, along with the relative error (Err). We concluded from the test results that we could use our analysis technique to accurately measure bijel topology.

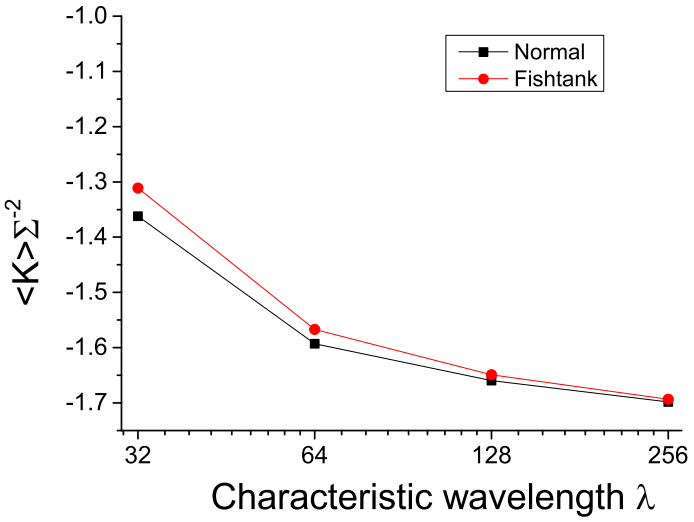

Figure 4.5: The area-averaged Gaussian curvature of a simulated gyroid, in a volume of 512 by 512 by 128 pixels, as a function of the gyroid wavelength (black), and the same after correcting for the fishtank effect (red).

We also explored the possible dependence of the accuracy on λ at fixed box size, while also accounting for the fishtank effect explained in the previous section (Figure 4.5). As the wavelength is reduced, the curvature measurement protocol becomes less accurate, i.e. produces a result further from the theoretical result expected (≈ -1.7). Also, the fishtank effect becomes more prominent as the wavelength is reduced. However, our data lies in the range between λ=128 and λ=256 pixels, where the curvature analysis protocol is hardly affected by taking

into account the fishtank effect.

Data volumes

The limitations of confocal microscopy in this case, namely the reduction in signal to noise (due to scattering) as the focal plane is moved further inside the sample, mean that acquired 3D data is constricted in the Z-direction. The dimensions of the XY plane are 640 $\times$ 640 μm^2, whereas the Z dimension is only about 80 μm. This may reduce the statistics when measuring interfacial curvatures, since there is clearly more information about 2 of the directions (XY) and less about the third (Z). To see what effect this may have, we have acquired larger scale 3D data from polymerized bijels [54] using X-ray computed tomography. The samples were micro-CT scanned (performed by Dr Rob Wallace at the Royal Infirmary of Edinburgh) using a Skyscan 1172 system (Bruker microCT, Kontich, Belgium). Rotating samples in angular steps of 0.4° over a full 360°, shadow-projection images with a pixel size of 4.48 μm were acquired (Hamamatsu 10 Mp camera). The source voltage was 28 kV (Hamamatsu 100/250); no filter was used between source and sample, but a beam-hardening correction of 20% was applied during reconstruction. Image reconstruction into axial slices was performed using the NRecon software package (Skyscan, version 1.5.1.5), yielding 3D data sets much larger than but similar in format to confocal data sets, i.e. Z-stacks of XY-slices. For reconstruction, a random movement of 10 was used, but no frame averaging was required to reduce the signal-to-noise ratio.

A comparison of the analyses of both types of data is presented in section 3.1.

4.4 Results and discussion

4.4.1 Confocal vs X-ray CT

Here we compare the analysis of data obtained from confocal microscopy (of a 63 nm NP stabilized bijel) and that obtained from X-ray CT (of a polymerized 63 nm NP stabilized bijel). Figure 4.6 shows example isosurfaces and distributions of mean and Gaussian curvatures. Since the X-ray method allows the sampling of much larger volumes than confocal, the isosurfaces created are much larger in area (Figure 4.6(a) vs 4.6(b)). This allows the measurement of curvature

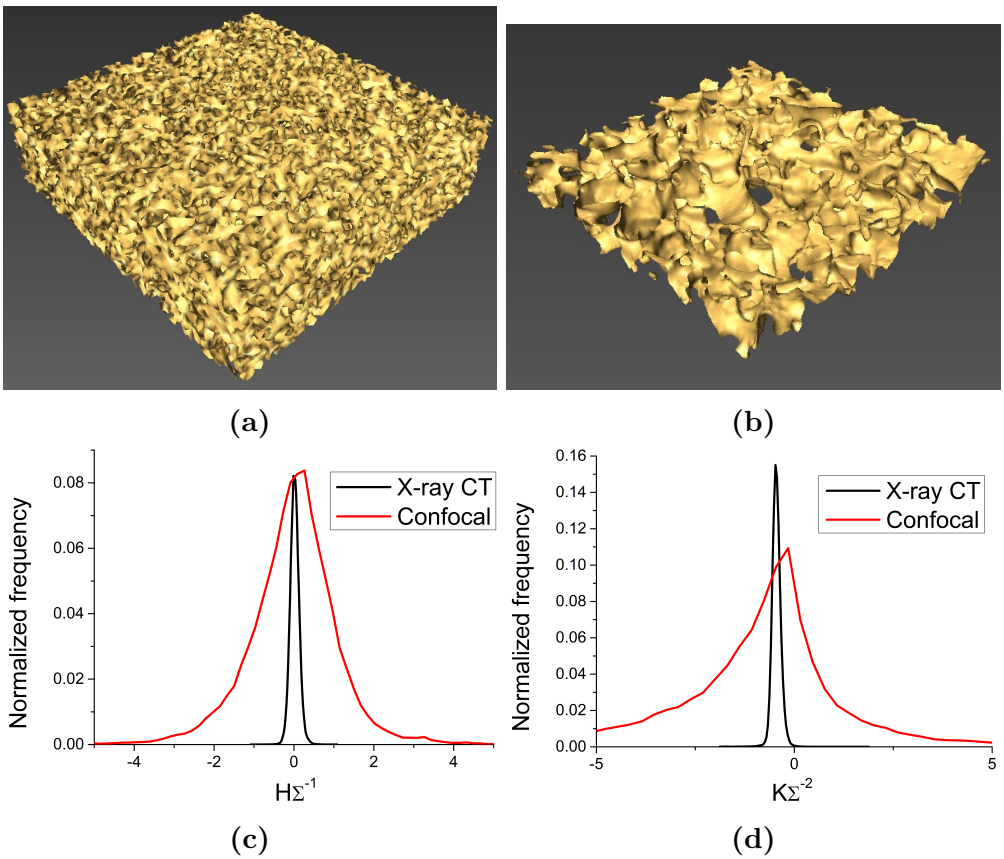

Figure 4.6: Example data used in the curvature analysis. (a) Isosurface created using X-ray CT data. (b) Isosurface created using confocal data. (c) Mean curvature distributions for both isosurfaces. (d) Gaussian curvature distributions for both isosurfaces. The distributions were normalized by dividing the raw counts by total number of counts.

over a larger number of bijel channels, increasing the accuracy. The increased precision, evidenced by the sharper distributions in (c) and (d), is due to the sharper contrast between the channels, as the confocal data suffers the consequences of the point-spread function and multiple scattering, whereas the X-ray data does not. Although the distributions are sharper, the shape and position of the distributions are qualitatively similar, and produce similar quantities: area-averaged mean curvature $\langle H \rangle \Sigma^{-1} = -0.02(1)$ and area-averaged Gaussian curvature $\langle K \rangle \Sigma^{-2} = -0.8(1)$ in the case of the confocal data, and $\langle H \rangle \Sigma^{-1} = 0.002(5)$ and $\langle K \rangle \Sigma^{-2} = -0.45(1)$ in the case of the X-ray data. Note that although the Gaussian curvature distributions appear to be peaked close to zero, most of the area is in the negative region, leading to a significant negative value for the area-averaged quantity. This has been observed in previous studies of polymer blends [124, 132].

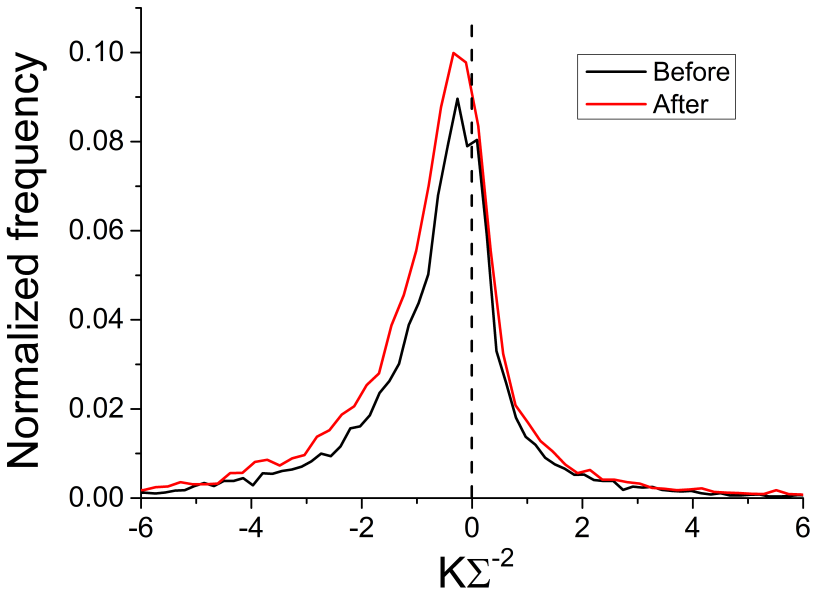

Figure 4.7: The distributions of Gaussian curvature as measured by confocal microscopy and image analysis for a bijel just before (black) and just after (red) polymerization, induced by UV irradiation.

To check what effect of the polymerization process on the bijel structure, we have also measured the curvature distributions of a MP stabilized bijel before and after polymerization using the same method (confocal). Figure 4.7 shows the distributions measured before and after polymerization. In order to minimize scattering, we (partially) matched the polymer refractive index using Dow Corning Fluid 550. The area averaged values are -0.69(17) and -0.60(19) i.e. relatively similar, meaning that the polymerization process itself leaves the structure largely unchanged. Note that these values cannot be compared to the results in subsequent sections for MP stabilized bijels because a slightly different protocol was used here to account for a larger ratio between the size of the channels and the data volume. Polymerizing bijel samples does involve a 4 to 5 hour waiting step, to allow the monomer to distribute throughout the sample, which may have an effect on the area-averaged Gaussian curvature values (see section 4.4.4).

A comparison of the curvature distributions of a bijel and its polymerized counterpart has been made previously by Lee *et al.* [54], showing $\langle H \rangle \approx 0$ in both cases (but with a small broadening in the negative region for the polymer) and $\langle K \rangle < 0$ in both cases (but with a small shift towards less negative values in the polymerized case). The results presented in this study are in broad agreement with the results of Lee *et al.*, with both mean curvatures close to zero and a less

negative value for the Gaussian curvature of the polymerized sample. However, the difference in Gaussian curvature for the polymerized sample in Ref. [54] cannot be unequivocally explained by the polymerization process, as the samples were prepared independently.

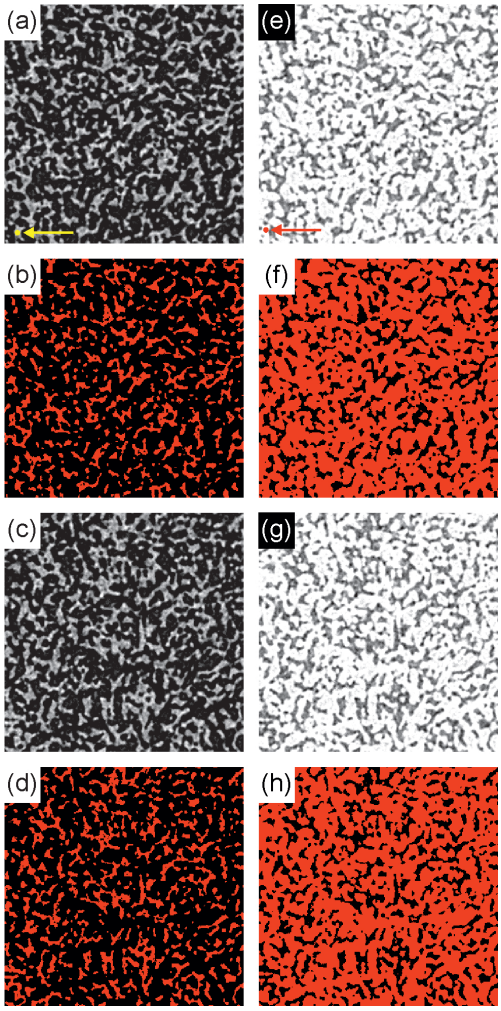

Figure 4.8: 2D slices from a 3D X-ray CT data set: (a-d) direct i.e. channel A is white and (e-h) inverted i.e. channel B is white. (a/e) Bottom slice: the yellow/red arrow points to the initial yellow/red point before region growing of channel A/B. (b/f) Same as (a/e) but after region growing, showing in red all the points above the threshold connected to the initial point in (a/e). (c/g) Top slice and (d/h) same as (c/g) but after region growing, showing in red all the points above the threshold connected to the initial point in (a/e). Adapted from Ref. [2].

Note that these results suggest that the bijel structure (both in liquid and polymerized form) is bicontinuous in three dimensions, given the negative values of area-averaged Gaussian curvature and almost zero values of area-averaged mean curvature. To further demonstrate the bicontinuity of the bijel structure, we have performed a region-growing analysis on the X-ray CT data. Figure 4.8 shows bottom and top slices from a 3D X-ray CT data set, both in direct (channel A white) and inverted (channel B white) grayscale. Selecting a pixel in the white channel in the lower left corner of the bottom slice (see arrows in Fig. 4.8(a/e)), we use 'region growing' to show that it is connected to the pixels in the white channel in the top slice (Fig. 4.8(d/h)). This qualitatively demonstrates that both channel A and channel B are continuous and, thereby confirming that our bijel samples are indeed bicontinuous. As a quantitative measure, the total number of pixels in channel A (in 3D) above the threshold but not connected to the initial point in (a) is only 0.03%.

Notably, the fact that we get acceptably similar results when we use the method with a lower signal-to-noise ratio (confocal) allows us to use this *in-situ* characterization technique to study the effect of particle size and quench rate on bijel topology.

4.4.2 Effect of particle size

We now focus on data obtained from confocal microscopy, and vary the size of the particles used to stabilize the bijel, while keeping the quench rate constant at 350°C/min (microwave method). In this section, the bijel lengthscales were in the range 31 μm $< L <$ 91 μm.

Figure 4.9 shows how the area-averaged curvatures vary with particle size, including a measurement of simulated data (red points) which we address later. The data corresponding to $r = 63$ and 367 nm has been averaged over three uniquely prepared samples, whereas the data for $r = 50$ nm (and the simulated data) has only been sampled once – hence, the error bars for the former indicate one standard deviation, and the error bars for the latter indicate the thresholding uncertainty.

The area-averaged mean curvatures of the (final) bijel structures show a small dependence on particle size, with a significant positive value for the MP bijel and smaller positive values for the NPs. This does not contradict the results of Lee *et*

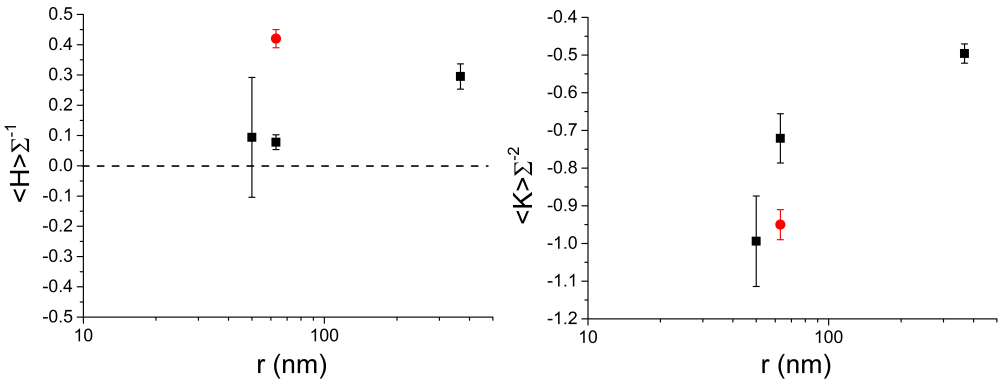

(a) (b)

Figure 4.9: The change in area-averaged mean curvature (a) and Gaussian curvature (b) as a function of particle size. The red data points are measurements performed on simulated data (see text). The error bars for the two right-most black squares indicate one standard deviation of the distribution of 3 separate measurements, whereas for the left-most point (and the red point) the error bars indicate the thresholding error from one unique measurement.

al. since an inspection of the histograms reveals that all distributions are *centred* on zero (see Figure 4.12). These results are indicative of a stronger preferred direction of curvature for the MP bijel and a weaker preferred direction for the NP bijels. Indeed, since this bijel system has unequal phase volumes we would expect a preferred direction of curvature [124].

The area-averaged Gaussian curvatures show a clearer dependence on particle size – the smaller the particle, the more negative the value. In other words, as the size of the stabilizing particles is decreased, the bijel becomes more hyperbolic in character, and more closely resembles the gyroid. Note that the distribution of Gaussian curvatures (Figure 4.12) are centred close to zero similar to the mean curvature distributions, but there is a clear skewing towards the negative region, giving an area-averaged negative value. The mean curvatures on the other hand are more symmetric, resembling a Lorentzian distribution.

We can partly explain the results by considering the following. The batch of particles used in the bijel mixture will have a distribution of contact angles centred close to the desired 90° [133], and the particles with $\theta \neq 90°$ will induce a spontaneous curvature on the L-L interface [119]. Although NPs will induce a larger spontaneous curvature than MPs, the driving force towards this curvature is smaller [1]. Hence, it is expected that NPs are less disruptive to the L-L interface than MPs, and hence more likely to lock-in the spinodal structure of the L-L

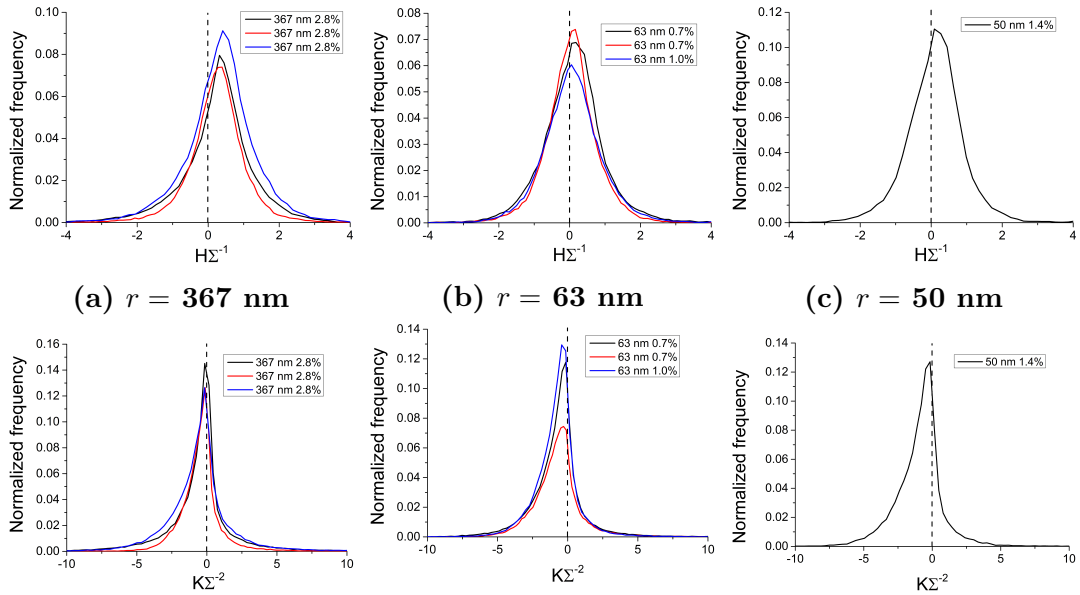

(a) r **= 367 nm** **(b)** r **= 63 nm** **(c)** r **= 50 nm**

(d) r **= 367 nm** **(e)** r **= 63 nm** **(f)** r **= 50 nm**

Figure 4.10: The normalized frequency distributions of mean curvatures $H\Sigma^{-1}$ (a) - (c) and Gaussian curvatures $K\Sigma^{-2}$ (d) - (f) for the three experimental data points shown in Figure 4.9.

phase separation. The data presented here is largely in agreement with this. The relative lack of preferred curvature direction for the NP stabilized bijels is consistent with the picture of the NPs being more successful at preventing pinch-off events, resulting in a larger number of (hyperbolic) fluid necks rather than (parabolic) bulging regions which would exist immediately after pinch-off.

To assess how closely the bijels resemble the L-L interface without particles we refer to previous work on a mixture of polybutadiene and poly(styrene-ran-butadiene) undergoing spinodal decomposition [129]. By using their measured data for the quantities $\Sigma/q_m = 0.5$ (where q_m is the position of the peak in the Fourier intensity spectrum, i.e. after the 3D image data has been transformed into frequency space) and $\langle R\rangle/L = 0.3$ (where $\langle R\rangle$ is the average radius of curvature), we have calculated a value of $\langle K\rangle\Sigma^{-2} \approx -1.13$. Note that this is significantly different from the gyroid, but since the gyroid is a *minimal* surface ($H = 0$ everywhere) it may be better at quantitatively describing *equilibrium* structures rather than the non-equilibrium structures reported here, for which we and others see a distribution of H *centred* on 0 [54, 127]. Also, there are differences between the system studied here and the system studied by Jinnai *et al.* [129], namely the ratio of interfacial tension to viscosity, so the calculated value is only an estimation. However, it can still be concluded that the NPs lock-in structures

with greater hyperbolic character which more closely resemble the L-L spinodal interface.

To assess how closely the bijels resemble simulated spinodal decomposition in the presence of neutrally-wetting particles, we performed our curvature analysis on data obtained from lattice-Boltzmann simulations. The results are shown as the red data points in Figure 4.9. The area-averaged mean curvature has a value of 0.42(3) and the area-averaged Gaussian curvature has a value of -0.95(4). To achieve practical computation times, the simulated particle radius was 63 nm, but the bijel lengthscale $L = 500$ nm was considerably smaller than in experiments ($L/r \approx 10$ as opposed to $\approx 100 - 1000$ in experiments). We attribute the positive mean curvature to the phase volume asymmetry (simulated as 65:35) as we do in the experimental case outlined above. The simulated Gaussian curvature is significantly below the corresponding experimental value but is very close to the experimental value for $r = 50$ nm and only slightly above the estimate for the L-L spinodal interface without particles (-1.13). This discrepancy between the $\langle K \rangle \Sigma^{-2}$ values obtained from experimental and simulated data is likely due to the *distribution* of contact angles (centred on $\approx 90°$) present in the experimental case, which more drastically effects MP stabilized bijels as per our previous discussion (resulting in less negative Gaussian curvature) and suggests that the particles might be making the L-L interface less hyperbolic [1]. Another potential factor is the instantaneous quench used in the simulations which cannot be achieved in experiments. Nonetheless, we can conclude that the use of NPs results in structures of greater hyperbolicity which more closely resemble the expected spinodal pattern of a bijel.

From the point of view of applications, we now have a *quantitative* characterization of bijel topology that allows rational optimization of fabrication parameters. For example, if one wanted to design a symmetric cross-flow microreactor from a bijel, then a hyperbolic rather than a parabolic surface would be desirable (to reduce the occurrence of bottlenecks and/or dead-ends), and our analysis shows that using smaller particles would be beneficial. To further demonstrate this approach to bijel-materials design, we continue by considering two additional bijel fabrication parameters: quench rate and age (i.e. time after bijel formation).

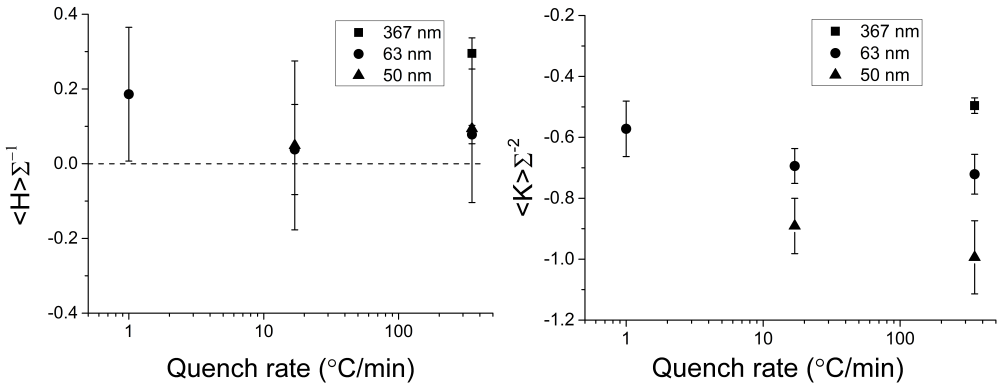

(a) **(b)**

Figure 4.11: The change in area-averaged mean curvature (a), Gaussian curvature (b) as a function of quench rate. The dashed line in (a) indicates the value expected for the gyroid.

4.4.3 Effect of quench rate

Here we continue to focus on confocal microscopy data, but now vary the quench rate used in the fabrication step (see Experimental Methods). Note that in the bijel literature, the term 'quench' can refer to either cooling (in the case of an upper critical solution temperature, UCST) or heating (in the current case of a lower critical solution temperature, LCST). Figure 4.11 shows how the area-averaged curvatures vary with quench rate, with the 350°C/min data points being the same as shown in Figure 4.9 but on new axes. The 50 nm data and the 1°C/min data has only been sampled once here. In this section, the bijel lengthscales were in the range 21 μm $< L <$ 91 μm.

The area-averaged mean curvatures in the case of NP bijels remain constant upon the decrease to 17°C/min, but rise upon a further decrease to 1°C/min. The preferred direction indicated by this data point could either be due to the presence of droplets (of a size similar to the channel width) in slowly-quenched samples due to secondary nucleation [75], or due to the same mechanism which results in the preferred direction in (fast quenched) MP bijels. The area-averaged Gaussian curvatures show a slight variation with quench rate, becoming less hyperbolic as the quench rate is reduced. Interestingly, it appears that quenching the 63 nm particle bijel at 1°C/min yields a structure similar to a 367 nm particle bijel, quenched at 350°C/min.

Figure 4.12 shows the corresponding distributions of mean (a) - (c) and Gaussian (d) - (f) curvatures for the 1°C/min and 17°C/min data shown in Figure 4.11.

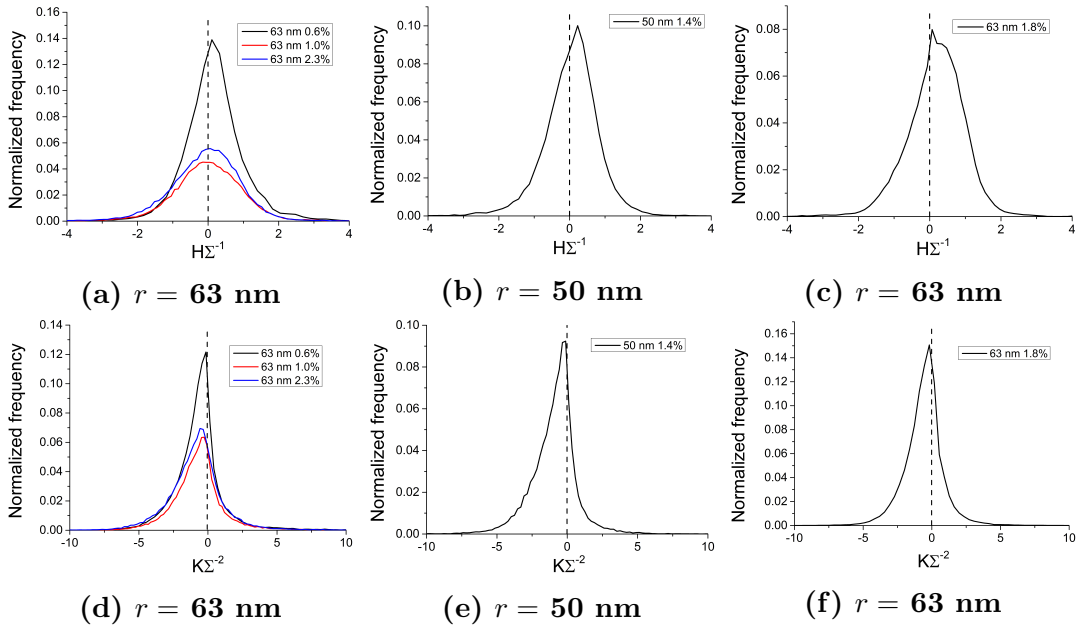

(a) $r = 63$ **nm** **(b)** $r = 50$ **nm** **(c)** $r = 63$ **nm**

(d) $r = 63$ **nm** **(e)** $r = 50$ **nm** **(f)** $r = 63$ **nm**

Figure 4.12: The normalized frequency distributions of mean curvatures $H\Sigma^{-1}$ (a) - (c) and Gaussian curvatures $K\Sigma^{-2}$ (d) - (f) for the three additional experimental data points shown in Figure 4.11; 17°C/min (a,b,d,e) and 1°C/min (c,f).

Again, the mean curvature distributions are symmetric and centred on zero (within a half-width at half maximum interval), whereas the Gaussian curvature distributions are skewed towards the negative region and peaked just to the left of zero.

To explore the origin of the small dependence of area-averaged Gaussian curvature on quench rate, we explain the effect of the quench rate on the phase separation dynamics. In the current case of spinodal decomposition, we assume that the relevant phase-separation regime is the 'viscous hydrodynamic' (VH) one, based on the following estimate of the crossover time between the diffusive and viscous hydrodynamic regimes [50]. The diffusive regime lasts for a time $\tau = \zeta^2/D$ [134] where ζ is the correlation length and D is the molecular diffusivity. To calculate τ we use data from Ref. [135], giving $\zeta = 2\epsilon^{-0.61} \times 10^{-10}$ m and $D = 0.29\epsilon^{0.554} \times 10^{-9}$ m^{2}s^{-1} where ϵ is the reduced temperature $(T - T_c)/T_c$, in terms of critical temperature T_c and sample temperature T. At 45°C, $\tau \approx 1$ ns. However, this is likely to be an underestimate, since the phase separation begins as soon as the phase boundary is crossed at 34.1°C. By taking a quench depth of 0.1°C, τ becomes 4 μs. The exact time taken to reach the VH regime will in practice depend on the quench rate, but since our smallest unit of time in the laboratory frame is about 0.5s (the time it takes to acquire a single image using the confocal

microscope), we can safely assume that we are observing the phase separation and particle attachment in the VH regime.

In the VH regime, the characteristic lengthscale of the structure scales with time according to $L \propto \frac{\gamma}{\eta}t$, where γ is the interfacial tension and η the fluid viscosity; γ scales with the quench depth as $\Delta T^{0.88}$, which itself scales with time according to the quench rate used ($\Delta T = \beta t$, where β is the quench rate, and t = 0 when the temperature reaches 34.1°C). η shows some variation in the relevant temperature range but for the purposes of this illustration can be approximated as constant [8]. Hence, varying the quench rate changes the prefactor in the growth law, which is akin to saying that it changes the phase separation 'speed', with faster quenches resulting in higher speeds, which may help in two ways. Firstly, the particles will have less time to accumulate a wetting layer of lutidine, which can affect their contact angle [69]. Secondly, the system spends less time in a state where the particles on the interface can interact, because the interfacial particles reach a jammed state quicker, and this may well allow the particles to better lock in the spinodal structure [1].

Previous work with the W/L bijel has shown that only certain particle size and quench rate combinations successfully produce bijels [1] – the fastest rates are required to form bijels with MPs, but NPs can form bijels at any rate in the range 1 to 350°C/min. If we conclude that reducing the quench rate results in a final bijel structure of reduced hyperbolic character, then by applying that reasoning to the 367 nm data point in Figure 4.11(b) we can further illustrate why successful bijel formation with MPs at slower rates is unlikely. When the area-averaged Gaussian curvature gets closer to the region $\langle K \rangle \Sigma^{-2} \geq 0$, it becomes more and more like a standard Pickering emulsion with increasing amounts of interfacial area curved in the same direction (i.e. droplet morphology), which has been observed previously. Hence, we can argue that bijel formation will succeed only when the combination of particle size and quench rate results in a (final) structure with sufficiently negative area-averaged Gaussian curvature, and we now know (approximately) what the sufficient value is, and what the range of required parameters is.

4.4.4 Curvature change with time

Figure 4.13 shows the area-averaged Gaussian curvatures as a function of time from the onset of phase separation, for three uniquely-prepared (by quenching

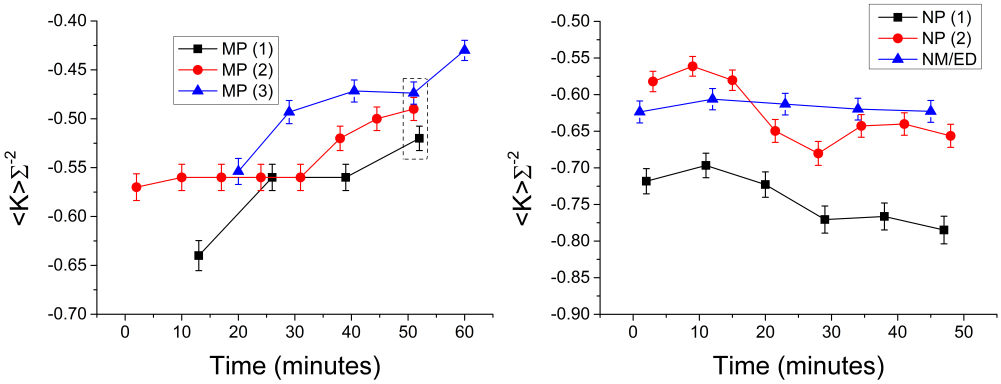

Figure 4.13: (a) The change in area-averaged Gaussian curvature as a function of time for three separately prepared MP bijels (black, red and blue, $\phi = 2.8\%$). The data points in the dashed box are the ones used to generate the MP 350°C/min data point in Figures 4.9 and 4.11. (b) The change in area-averaged Gaussian curvature as a function of time for 2 NP bijels (black and red, $\phi = 0.7\%$ and 1.0% respectively) and a MP nitromethane/ethanediol bijel (blue, see text for details). Error bars are $\pm 2.4\%$, the error derived from the analysis test in section 2.6.

at 350°C/min) samples of (a) MP stabilized bijels and (b) (two unique) NP stabilized bijels along with one sample of a bijel made with a different liquid-liquid combination (and MPs of radius $r = 290$ nm), nitromethane/ethanediol (NM/ED).[36] The data points in the dashed box in (a) were the ones averaged to create the 367 nm 350°C/min data point shown in Figures 4.9(b) and 4.11(b), as these were the points closest together on the time axis. In all cases, the values plotted are obtained from the maximum-isosurface area reconstructions, and the error bars are $\pm 2.4\%$.

In the MP W/L case (Figure 4.13(a)), there is a marked upward movement of the Gaussian curvature in each timeseries, with the final points in all timeseries at least a full error bar above the initial points. In the NP W/L or the MP NM/ED case however (Figure 4.13(b)), there is no such upward trend, and arguably a downward trend in the case of the NP W/L bijels (red and black). Note that the black and red NP data represent different concentrations of particles and have different absolute values of $\langle K \rangle \Sigma^{-2}$, but this is most likely due to experimental variation given the spread in absolute values shown in Figure 4.13(a) for three identical repeats. It is also interesting to note that the MP bijels begin their 'life' with a structure not too dissimilar from the NP bijels, but mutate over the course of about an hour to end up with a less hyperbolic, sub-optimal structure, which may also explain the less negative $\langle K \rangle \Sigma^{-2}$ from X-ray CT data in section 3.1 (as

polymerizing samples requires a 4 to 5 h waiting period).

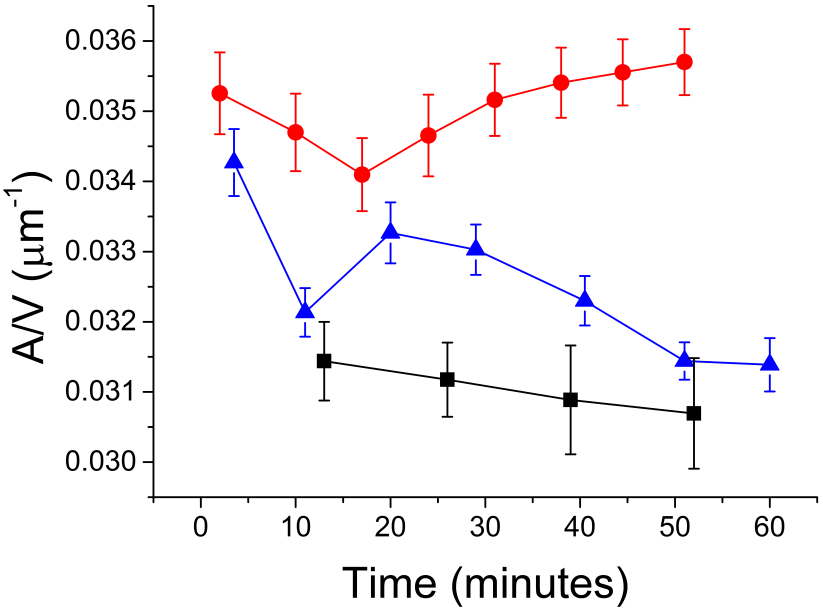

Figure 4.14: The change in the surface to volume ratio (A/V) over time for the 3 microparticle (MP) stabilized bijels shown in Figure 4.13(a) – MP 1 black squares, MP 2 red circles, MP 3 blue triangles.

This phenomena is quite unexpected as all of these samples are considered to be in their 'jammed' state. Figure 4.14 shows the surface to volume ratio as a function of time for the three MP stabilized bijels studied in Figure 4.13(a). Two of the three bijels show slight coarsening behaviour, i.e. a reduction in A/V over time (MP 1 black squares & MP 3 blue triangles). But since the area-averaged Gaussian curvature values in Figure 4.13 have been normalized with respect to the surface-to-volume ratio (A/V), the upward trend cannot be attributed to any such coarsening. Nor can it be related to a change in genus (the number of holes in the surface), and therefore pinch-off events (due to the inability to invoke the Gauss-Bonnet theorem – see Experimental Methods). Therefore, the movement in Gaussian curvature towards zero indicates a change in the curvature distributions, which we call *mutation*.

The movement in Gaussian curvature in the case of MPs can be related with the time over which the elastic modulus of the W/L bijel has been measured to increase [90], which can further be associated with the phenomenon of monogelation – the emergence of a permanently-bonded particle network which can survive the remixing of the liquids [91]. We observe that a NP-bijel also forms a monogel, but crucially, only requires an incubation period of < 1 min (as described in Chapter 3.4.4). The NM/ED bijel does not form a monogel [90].

Hence, it is possible that the process of gelation of particles at the L-L interface leads to a mutation of the bijel structure.

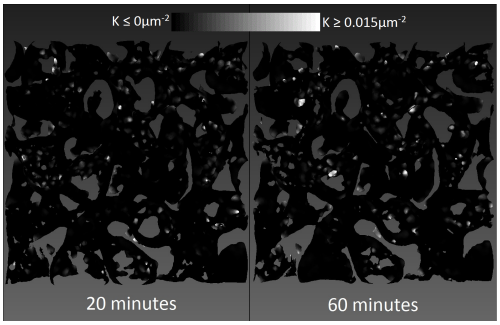

Figure 4.15: A comparison of the isosurfaces (top-down view) representing a 20 minute old bijel and a 60 minute old bijel, stabilized by MPs. The black areas have Gaussian curvature values less than zero, whereas the bright areas have positive Gaussian curvature, to varying degrees indicated by the brightness.

In an attempt to ascertain whether the mutation is a global (happens equally everywhere) or local (happens at only specific locations) phenomenon, we have mapped the Gaussian curvature values onto the reconstructed isosurface and compared the 20 min and 60 min-old bijels from the blue timeseries in Figure 4.13(a), shown in Figure 4.15. We have thresholded the values so that only positive values appear bright (with varying degrees of brightness), while the black spots are at zero or less.

What we see in Figure 4.15 are subtle differences in the locations of positive Gaussian curvature, and larger bright spots in the 60 min old sample compared to the 20 min old sample. The changes are so small that it is difficult to say whether there are specific regions which change more than others.

To investigate further, we compare the curvature distributions at the beginning and end of the mutation process. Figure 4.16 shows the change in the distributions for the three MP bijel data sets shown in Figure 4.13(a). The largest changes take place around the $K\Sigma^{-2} = 0$ line, implying that points of small negative Gaussian curvature mutate into points of small positive Gaussian curvature. The entirety of these small changes in the curvature distributions is what changes the metric $\langle K \rangle \Sigma^{-2}$. The precise mechanism behind the mutation will need to be confirmed by further study.

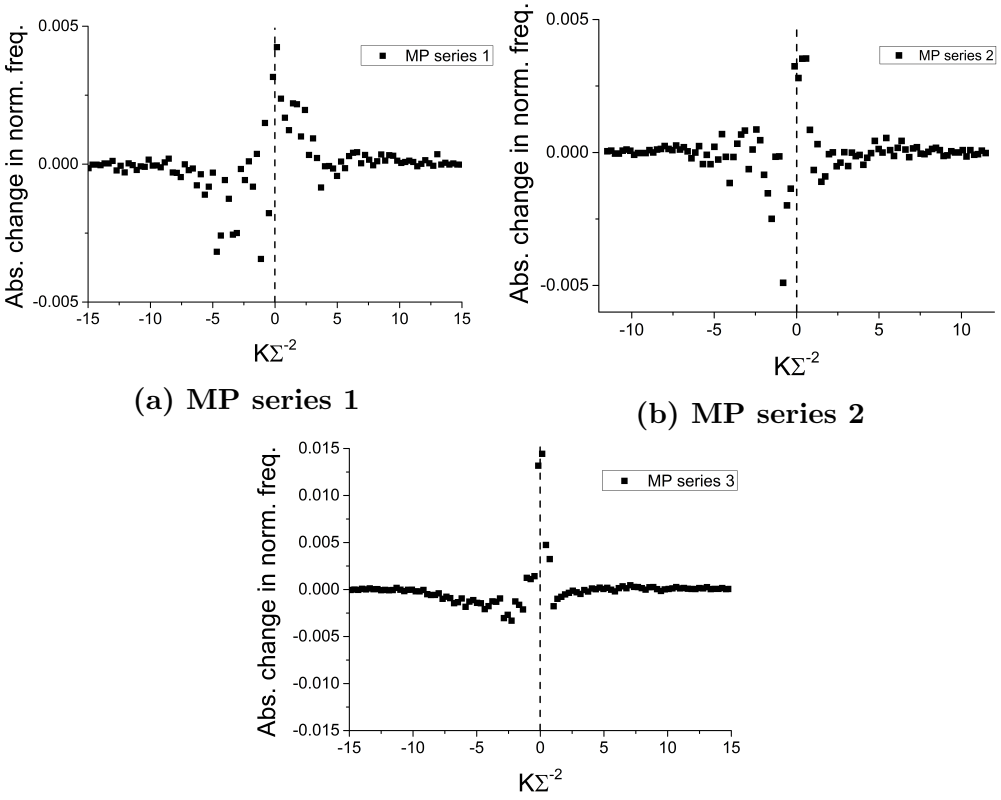

(a) MP series 1

(b) MP series 2

(c) MP series 3

Figure 4.16: The absolute change in the area-averaged Gaussian curvature distributions between the first and last time point in the three timeseries presented in Figure 4.13(a).

4.5 Conclusions

In this chapter, we have performed an extensive characterization of the topology of bijels produced using different particle sizes and quench rates, and monitored the structures over time. In addition, we have demonstrated that bijels are bicontinuous using an image-analysis technique known as 'region growing'. Optimally hyperbolic (large negative Gaussian curvature) structures are obtained when smaller particles and faster quench rates are used. Nanospheres appear to be better than microspheres at locking in the spinodal pattern of the L-L interface during demixing. Microparticle stabilized bijels appear to mutate away from an optimal structure, which may be related to the monogelation phenomenon [91]. Nanoparticle stabilized bijels, which form a monogel on much shorter timescales, become marginally more optimal over time, and a non-monogelling system (nitromethane/ethanediol) shows no such mutation. In practical terms, we now have a characterization which enables us to systematically optimize

the morphology of (final-state) bijels, which will assist in its development for applications.

Chapter 5

Bijel Dynamics Probed by Diffusing-Wave Spectroscopy

5.1 Abstract

Bijels consist of a jammed layer of interfacial colloids which separate two tortuous liquid domains. The jammed interfacial particle layer has kinetically arrested the liquid-liquid (L-L) phase separation and is out-of-equilibrium, so the structure may not be stable on long timescales. Although the structure is known to be sufficiently solid in some cases for post-processing, the microscopic dynamics have not yet been probed experimentally, and may provide an insight into the observed onset of particle-bonding in the case of water/lutidine (W/L) bijels, as well as an insight in to the system's (potential) relaxation towards equilibrium. Here we use multispeckle diffusing-wave spectroscopy (MS-DWS) to study the microscopic particle dynamics in bijels. We find that bijels exhibit (previously unreported) aging behaviour dependent on particle size and liquid-liquid combination – the dynamics slow down at different rates, and the correlation functions do not fall onto a single master curve, making the bijel's behaviour difficult to interpret in terms of universal aging. We compare the bijel dynamics to the dynamics of colloidal gels formed by diffusion-limited cluster aggregation (DLCA) which do exhibit universal aging features applicable to a wider range of soft jammed materials, including concentrated emulsions and micellar polycrystals.

5.2 Introduction

Bijels are formed by arresting the spinodal decomposition of a binary fluid mixture by a (jammed) interfacial layer of (approximately) neutrally-wetting colloids [3]. The structures formed in this way are out of equilibrium – the thermodynamically driven phase separation is kinetically arrested by the jammed layer of interfacial colloids [5]. The bijel is part of a larger group of jammed, out-of-equilibrium systems, but is unique in that the structure is comprised of a locally planar (2D) arrangement of colloids which spans a 3D network, held in place initially by interfacial forces, which in some cases subsequently develops interparticle attractions [91]. Hence, it differs somewhat from other types of jammed matter, e.g. colloidal gels formed by diffusion-limited cluster aggregation (DLCA) [136], or colloidal glasses resulting from caging effects at high volume fraction [137]. In a bijel, the interfacial particles undergo a jamming transition as they are pushed together by the shrinking interfacial area and end up as a dense 2D layer spanning a 3D space (with a low overall volume fraction), whereas in DLCA gels the particles form a 3D network of dense 3D clusters formed by diffusion. In a colloidal glass, the particles (at high volume fraction) are constricted in three dimensions by other particles, whereas in a bijel they are restricted along the interface in two dimensions by other particles but by the interface in the third dimension. Unlike the DLCA gels and colloidal glasses, microscopic bijel dynamics have not yet been probed experimentally, although simulations [5, 11], rheological measurements [90] and measurements of interfacial curvatures (Chapter 4) have suggested that the macroscopic aging of the bijel structure (at least in some cases) does not completely cease.

Experiments have shown that bijels can remain jammed/stable for months [6, 69], in that the bijel structure doesn't appear to change significantly and the characteristic lengthscale L doesn't appear to change (outwith the sensitivity of microscopy measurements). This provides ample time for converting into other useful materials like porous polymer monoliths in the case of the water/lutidine (W/L) bijel [6, 54]. A crucial aspect of the suitability of the W/L bijel for post-processing techniques is the formation of a permanent particle gel (monogel) network at the liquid-liquid interface which relies on some form of interparticle bonding rather than the interfacial forces present in the initial jammed state [90, 91]. The monogel (which forms in the W/L system with dried silica particles [91] and not in the NM/ED system with HMDS treated silica [36]) provides

sufficient mechanical rigidity to withstand the post-processing [90] (we have also observed that a monogel does not form in the W/L system when HMDS treated particles are used). Depending on the size of the particles, the monogelation can take place in under a minute (in the case of radius $r \approx 63$ nm) or over a period of about 40 minutes (in the case of $r \approx 367$ nm), as outlined in Chapter 3. It has been proposed that the monogelation can take place by thermal fluctuations (over time) pushing neighbouring particles over their electrostatic repulsive barrier predicted by DLVO theory and into their primary van der Waals attractive minimum [91], although this has not been verified experimentally. Time-dependent behaviour in bijel systems, over a similar timeframe to that of the monogelation process, has been investigated via the measurement of interfacial curvatures but the underlying mechanism has not been unequivocally established [2] (see Chapter 4.4.4). Presumably, there should be a change in local particle dynamics accompanying the onset of interparticle bonding, and perhaps a further influence on any dynamical modes of the 3D gel network, which could be measured during a light scattering experiment.

In addition, the question of a bijel's ultimate fate is still an open one, with simulations unable to rule out complete phase separation caused by particle expulsion [5, 11, 45, 49], although particle expulsion is observed in some cases [5, 11, 49]. Note that the particle size used in simulations is drastically smaller ($r \approx 5$ nm as opposed to $r \approx 250$ nm in experiments) which makes particle expulsion in the experimental case less likely. The lack of particle expulsion in simulations can also be due to limited simulation timescales or the exclusion of particle thermal motion [45]. Experiments have so far only been able to demonstrate cessation of coarsening on lengthscales larger than the measurement techniques (i.e. roughly 1 μm) [1, 6, 36, 75, 92], leaving open the possibility of continuous changes in L of less than this, although a solid-like character has been shown via rheological measurements [90]. Probing the interfacial particle dynamics could assist in answering the question of the bijel's ultimate fate.

The dynamics of similarly jammed systems, e.g. DLCA gels and colloidal glasses, have been studied with various light scattering and rheology techniques, for example diffusing-wave spectroscopy (DWS) [138, 139], dynamic light scattering (DLS) [140, 141], static light scattering (SLS) [142] and rheology [143] revealing interesting properties. Correlation functions constructed from light scattering experiments representing time and lengthscale dependent structure factors show moderate early-time decays which are attributed to thermally activated motion

of the elastic modes of the gels. Secondary decays (in the intermediate and late times) are attributed to the relaxation of (local) dynamical heterogeneities formed by syneresis [140]. More generally, for other soft jammed materials the secondary decay is attributed to the relaxation of randomly-distributed internal stresses which could arise for reasons other than syneresis [144]. It would be interesting to see if these behaviours are observed in this related but distinct jammed system.

To probe the particle dynamics in a bijel, we use light scattering instead of more extensive microscopy (as in Chapter 4) because real-space studies require large sample volumes for adequate statistics and the temporal resolution is limited by the relatively slow data acquisition rate of the confocal set up (however it may be possible to use a fast confocal setup in future to achieve the same results). We use a light scattering technique particularly appropriate for our samples (due to the opacity of the system) which is DWS. DWS has been developed to extend DLS to the multiple scattering limit, making it applicable here [145]. DWS is also suitable because it probes particle motion on much smaller lengthscales than DLS, and we expect the displacement of interfacial particles to be small (less than the particle radius). The bijel's non-ergodicity is accounted for by using the multispeckle (MS) technique, allowing for spatial (instead of time) averaging for the generation of the correlation function [146] (see theory section below for an explanation).

We design our study around three systems in order to investigate the dependence of the dynamics on particle size and monogel formation – W/L bijels stabilized by both microparticles (r = 367 nm) and nanoparticles (r = 63 nm), and the NM/ED bijel stabilized by microparticles (r = 290 nm). We find that bijel dynamics show a two step decay in a qualitatively similar fashion to DLCA gels. The bijel dynamics slow down with sample age in a similar fashion to DLCA gels and other soft jammed materials. In this respect the behaviours are separated depending on the monogelling nature of the system, with the monogelling systems (W/L) showing accelerated aging over the non-monogelling system (NM/ED). We compare the results to those reported for DLCA gels which show universal aging features and propose possible microscopic mechanisms responsible for the bijel dynamics and aging behaviour.

The rest of the chapter is organized as follows. In section 5.3 we describe the sample preparation, DWS theory and method. In section 5.4.1 we begin by presenting and comparing the measured correlation functions for the three systems, which all show aging behaviour. We then quantitatively characterize the

aging behaviour, present rescaled correlation functions and discuss the differences in section 5.4.2. In section 5.4.3 we extract the mean-squared displacement of the particles and discuss the nature of the particle motion as the samples age.

5.3 Materials and methods

5.3.1 Materials

The materials (with associated purities and suppliers) used for the preparation of water/lutidine/silica bijels and nitromethane/ethanediol/silica bijels are given in Chapter 2.

5.3.2 Particles

The particles used to stabilize water/lutidine bijels were synthesized following the procedures outlined in Chapter 2. The two sizes of particles used here were $r = 63$ nm (nanoparticles, NPs) and $r = 367$ nm (microparticles, MP_1s), both labelled wth FITC, with polydispersities of 15% and 5.5% respectively (TEM sizing in both cases). Neutral wetting was achieved by drying small amounts of the particles ($\approx$ 50 mg) at 170°C at 20mBar pressure [68], and checked by inspecting confocal micrographs of bijels made with the particles.

The particles used to stabilize nitromethane/ethanediol bijels were synthesized in a similar fashion – the Stöber method was used with the addition of RITC for labelling. This produced particles with $r = 290$ nm (MP_2s).

5.3.3 Bijel preparation

Water/lutidine bijels

Water/lutidine (W/L) bijels were prepared by the standard method outlined in Chapter 2. MP_1 samples were inserted into cuvettes of 1mm path length, whereas NP samples were inserted into cuvettes of 5mm pathlength (Starna Scientific). The extra pathlength in the case of NPs was required because of the weaker scattering of NPs vs MPs, and the requirement that the photon mean free path

l^* be several times smaller than the sample thickness. Samples were quenched for 6 seconds (MP_1s) or 10 seconds (NPs, due to the larger sample volume) in a microwave (DeLonghi, P80D20EL-T5A/H, 800W) to produce phase separation and bijel formation. Immediately after quenching, the samples were placed inside an aluminium block which had been preheated to 50°C by encasing it in a copper ring and using a thermostat (Lakeshore model 332) to control the temperature.

Nitromethane/ethanediol bijels

Nitromethane/ethanediol bijels were prepared by first adding MP_2s to nitromethane, and ethanediol doped with fluorescein was added to give a critical concentration (by mass) of NM:ED 64:36. The volume fraction of particles was 5%. Note that this system has an upper critical solution temperature, the opposite of the water/lutidine system, and hence requires cooling for the initiation of phase separation. The particles were dispersed by first heating the mixture on a hot plate and then placing it in a hot ultrasonic bath. The mixture was then transferred to a 1mm path length cuvette (Starna Scientific) and returned to room temperature using a stirred water bath. This temperature quench resulted in spinodal decomposition of the liquids and ultimately a bijel as the particles attached and jammed at the liquid-liquid interface.

5.3.4 Principles of multispeckle diffusing-wave spectroscopy

Diffusing-wave spectroscopy (DWS) is an extension of dynamic light scattering (DLS) to the multiple scattering limit [145]. By using a diffusion approximation to model the path of photons through a concentrated sample of strong scatterers, the temporal fluctuations of the transmitted light intensity can be related to the motion of the scatterers. However, the diffusion approximation is only valid if the transport mean free path l^* (defined as $l^* = n_0 l$ where n_0 is the number of scattering events required for the randomization of direction and l is the distance travelled between scattering events) is much smaller than the sample dimensions [145].

DWS probes motion on much smaller lengthscales than DLS. In DLS, the lengthscale is set by the inverse of the scattering wavevector $q^{-1} \sim \lambda$ (where $q = (4\pi/\lambda)\sin(\theta/2)$, λ is the wavelength of light and θ is the scattering angle), whereas in DWS the decay of the correlation function is due to the cumulative

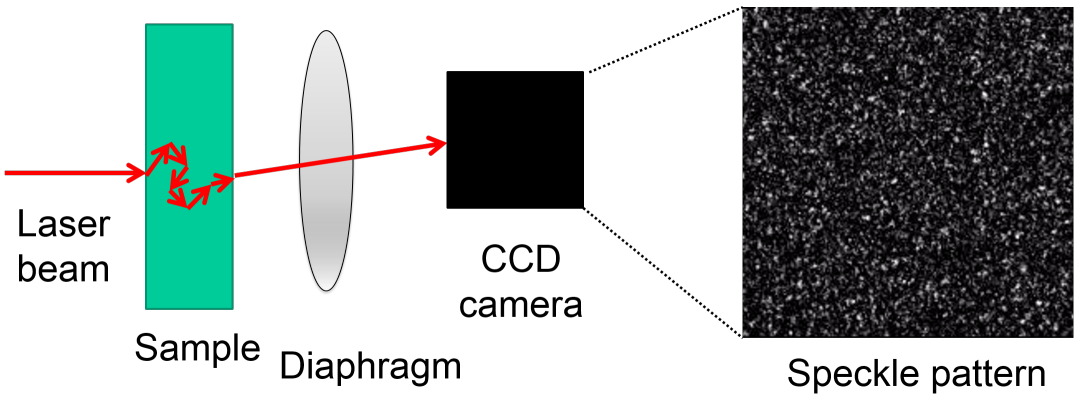

Figure 5.1: A schematic of the diffusing wave spectroscopy (DWS) setup. A laser beam is directed at the sample with the multiply-scattered light collected by a fast CCD camera. The camera records a time-varying speckle pattern – an example (still) frame of the pattern is shown on the right.

effect of multiple scattering events from particle motion on lengthscales much smaller than λ. This makes DWS much more sensitive to particle motion than DLS, with the drawback that any angle-dependent (and hence lengthscale dependent) information has been lost due to the multiple scattering.

When performing a DWS experiment, the ergodicity of the sample must be considered. For ergodic samples, the time-average is equal to the ensemble average, and so a single speckle experiment with time averaging of the correlation function provides the required result. For non-ergodic samples, e.g. bijels, the time average will not equal the ensemble average due to the system being unable to explore its entire configuration space [147]. Hence, the technique must be adapted. One way is to use a second cell containing a suspension of ergodic scatters, which allows the sampling of multiple photon paths in the target (nonergodic) cell, and hence provide an ensemble average from the time average [148]. An alternative method, used here, is to measure the temporal intensity fluctuations of multiple speckles and perform a spatial averaging of the correlation function [146]. This is done by using a fast CCD camera, and by treating each pixel as an individual correlator.

Once a sequence of frames is captured by the CCD camera, with each pixel's intensity fluctuating over time, the correlation function g_2 is calculated as follows;

$$g_2(\tau) = \frac{\langle I_i(0) I_i(\tau) \rangle_i}{\langle I_i(0) \rangle_i \langle I_i(\tau) \rangle_i} \tag{5.1}$$

where $I_i(0)$ is the intensity of pixel i in the first frame of the sequence, and $I_i(\tau)$ is the intensity of the same pixel in a subsequent frame separated by time τ. Notice the averaging over pixels i.

To be able to extract information about the motion of the scatterers, g_2 must be converted to g_1 via the Siegert relation, assuming that the pixel intensity fluctuations are Gaussian in nature [98];

$$|g_1(\tau)|^2 = \frac{g_2(\tau) - g_\infty}{\beta - g_\infty} \tag{5.2}$$

where β (the contrast) is the value of g_2 at $\tau = 0$ and g_∞ is the value of g_2 at $\tau = \infty$. The Gaussian nature of the fluctuations has been demonstrated previously for the case of a coarsening foam [149]. In the transmission geometry we use here, g_1 can be derived by modelling the diffusion of photons through the multiply-scattering sample and applying boundary conditions, giving [145]

$$g_1(\tau) \approx \frac{(\frac{L}{l*} + \frac{4}{3})\sqrt{\frac{6\tau}{\tau_0}}}{(1 + \frac{8\tau}{3\tau_0})\sinh(\frac{L}{l*}\sqrt{\frac{6\tau}{\tau_0}}) + \frac{4}{3}\sqrt{\frac{6\tau}{\tau_0}}\cosh(\frac{L}{l*}\sqrt{\frac{6\tau}{\tau_0}})} \tag{5.3}$$

with $\tau_0 = (Dk^2)^{-1}$, D a diffusion coefficient, $k = \frac{2\pi n}{\lambda}$ and n the refractive index of the sample medium. Since this expression has essentially exponential form, it can be approximated by the exponential [150]

$$g_1 \approx e^{-(\frac{L}{l^*})^2 k^2 \langle \Delta R^2(\tau) \rangle} \tag{5.4}$$

where L is the sample thickness, l^* is the photon mean free path and $\langle \Delta R^2(t) \rangle$ is the mean-squared displacement of the scatterers.

To determine l^*, a well-characterized sample (here polystyrene latex beads suspended in water, diameter 1 μm, Fluka) is measured under the same optical conditions (laser intensity, camera exposure time and gain settings, distance between sample and camera), and the correlation function is calculated. The $\langle \Delta R^2(t) \rangle$ term in the exponential is then replaced with the Brownian term $6D\tau$, with the Stokes-Einstein diffusion coefficient $D = \frac{k_b T}{6\pi\eta r}$. By fitting an exponential to the correlation function, and substituting in the known values of the other terms, l^* is extracted for the PS system. To obtain l^* for the sample system, the

transmission constant c is calculated using

$$cT_i = c\frac{I_i}{I_0} = \frac{\frac{5l_i^*}{3L_i}}{1+\frac{4l_i^*}{3L_i}} \tag{5.5}$$

where T_i is the transmission coefficient for the PS system, I_0 is the incident laser intensity and I_i is the transmitted intensity [151]. Using this value for c the same equation is used to arrive at l^* for the sample system, by substituting in the values I_0 and L_i for the sample system.

5.3.5 MS-DWS with bijels

After quenching a bijel sample in the microwave, the cuvette was placed inside a metal block which was encased in a copper ring attached to a thermostat for temperature control. In all cases, the thermostat was set to 50°C. A laser (Milles Griot Helium-Neon, 30mW max output) with a wavelength $\lambda = 632.8$ nm was directed at the sample, and a fast CCD camera (Mikrotron EoSens MC1362) was placed after the sample to collect the scattered light (as shown in Figure 5.1). The distance between the camera and the sample was chosen to produce a speckle radius of about 3-4 pixels. To capture the temporal variations in the intensities of the observed speckles, an AVI video was recorded with a frame size of 200 × 200 pixels. The frame rate of the camera was initially set to a high value, e.g. 2000fps, to capture the early-time dynamics (i.e. to begin capturing at a delay time of 1 frame $\times 1/(2000\text{fps}) = 0.005$s), but was decreased as the samples aged. Due to the limitations of the recording software, the file size was limited to 1Gb, effectively introducing a time 'window' from 0.005s (or 1/frame-rate) up to 26000 frames (determined by the image size) divided by the frame-rate (e.g. 26000/2000 = 13 seconds) per AVI. For the younger samples a quick high frame-rate AVI was recorded followed by a slower low frame-rate AVI to capture both early time and late time behaviour. The correlation functions were then appended to each other to expand the time window. A sequence of AVIs were captured as the sample aged, and in all cases the temporal fluctuations of speckle intensity was observed by eye to slow down with age.

The AVIs were subsequently analysed (offline) using a Matlab script to construct the correlation function (g_2) as per Equation 5.1, and Equation 5.2 was used to arrive at g_1. To calculate l^*, the cuvette containing the bijel was replaced with a well-characterized sample of polystyrene (PS) latex. All optical settings were

left untouched. After calculating g_1 for the PS system, Equation 5.5 was used to arrive at l^* for the PS and then the sample system. To evaluate the term $\frac{I_i}{I_0}$ in Equation 5.5, a photodiode was used to measure the intensity of incident laser light, and the transmitted intensity was measured by taking the average pixel intensity over an entire AVI movie. l^* is compared to the sample thickness L. For the diffusion approximation of light to be valid, $L >> l^*$. An analysis of the l^* values is presented in section 3.3, showing that here L is at least twice l^*.

During the DWS experiment the laser light was multiply scattered by the particles in the sample. In a bijel, the particles can be either attached to the liquid-liquid interface and part of the jammed layer or be freely diffusing in either of the liquid channels. Therefore, if the results are to be interpreted correctly, the possible effects of the free particles must be considered. We expect the contribution from free particles towards the scattering to decrease as the particles sediment – they will only have to sediment on average one channel width of about 50μm before they presumably aggregate with the jammed particle layer. Another possibility is that they simply perform Brownian motion near the channel wall, but as the particle concentration near the wall builds-up aggregation with each other and then with the particle network making up the channel wall seems likely. In addition, even if the free particles perform Brownian motion indefinitely and they contributed strongly to the scattered signal we would not expect to see an indefinite slowing down of the dynamics, which is what we have observed (see Results). Table 5.1 shows the times taken to sediment 50μm for the three cases

r (nm)	Liquids	Time to sediment 50μm (seconds/hours)
63	W/L	17,014/4.7
367	W/L	406/0.11
290	NM/ED	11,534/3.2

Table 5.1: The times taken to sediment one bijel channel width of 50μm for the three cases studied; W/L = water/lutidine, NM/ED = nitromethane/ethanediol.

studied. Note that most of the free particles will have sedimented after half this time, as the average distance a particle will sediment will be half a channel width. We propose that free particles will only contribute significantly in the case of NP stabilized W/L bijels, due to the larger number of free particles in this system compared with the MP systems (see Chapter 3). However, since the dynamics of free particles are not expected to slow down with time, as long as the free particles do not decorrelate all of the light then any slower (aging) process will

still be visible.

To reiterate, in the following sections the data obtained from performing DWS experiments on microparticle (MP, $r = 367$ nm) and nanoparticle (NP, $r = 63$ nm) stabilized water/lutidine (W/L) bijels, as well as MP stabilized ($r = 290$ nm) NM/ED bijels will be analyzed and discussed.

5.4 Results

5.4.1 Correlation functions

W/L with MPs

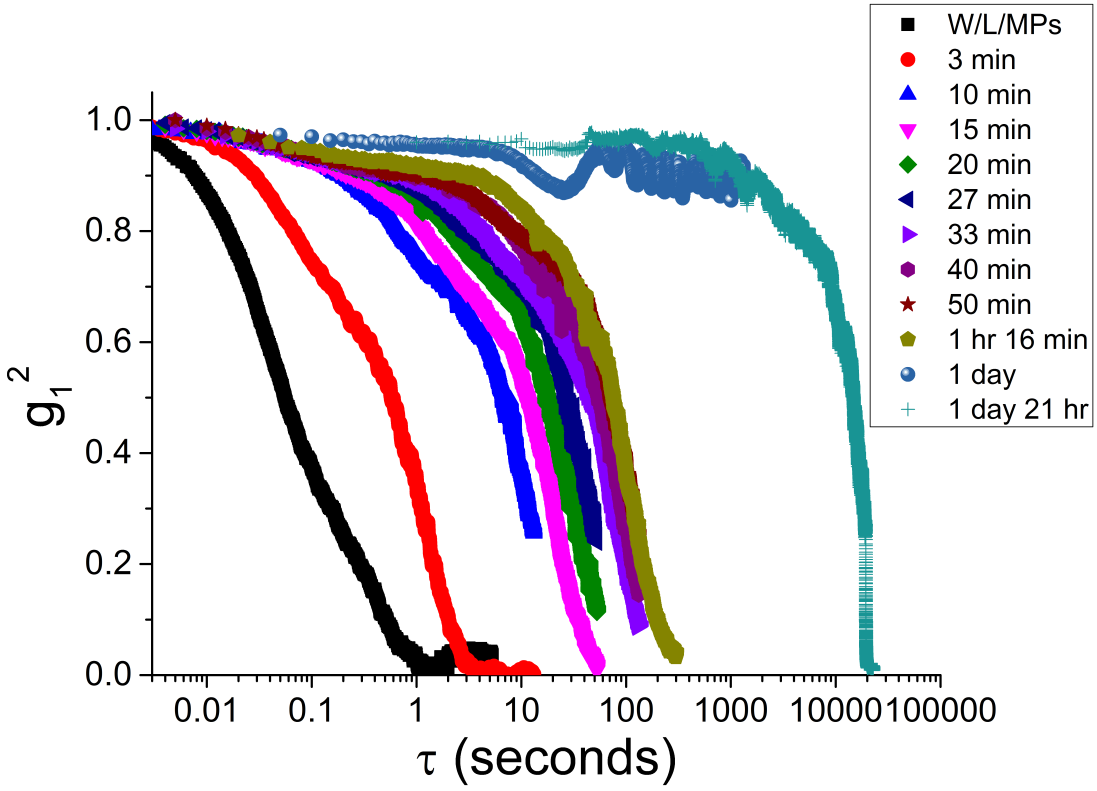

Figure 5.2: The correlation functions of microparticle (MP, $r = 367$ nm) stabilized water/lutidine (W/L) bijels as a function of delay time τ, labelled by sample age. The first data set (black squares) is the correlation function when only an MP dispersion in W/L is studied, at the same concentration and temperature (i.e. not a bijel). Note that the '1 day' data ends at around 2000 seconds and is not hidden by the '1 day 21 hr' data, as it may appear.

Figure 5.2 shows the correlation functions of MP stabilized W/L bijels labelled by sample age t_w. As t_w increases, the dynamics of the sample slows down, which shows that the sample is aging. Remarkably, complete decay of the correlation function is observed for a sample almost 2 days old, which suggests that the structure is still not completely solid after this time. There appears to be a two-step decay, evidenced by the double-bend in the 3 min - 40 min old curves. The second decay slows down faster than the first, leading to the appearance of a plateau between the aging times of 50 min and 1 hr 16 min at a value of ≈ 0.9, which moves to larger values with subsequent aging. This early time plateau is reminiscent of the behaviour observed for DLCA gels – the motion which causes the decorrelation being the thermally-activated elastic modes of the gel network [141]. The final complete decay of the correlation function is also reminiscent of the anomalous late-time behaviour observed in the same system, attributed to the emergence and relaxation of internal stresses due to gel syneresis and the subsequent restructuring of the particle network over lengthscales comparable to the cluster size [140]. Such restructuring, due to Laplace pressure, is seen in (2D) simulations of bijels stabilized by ellipsoids, for example [61].

W/L with NPs

Figure 5.3 shows the correlation functions of the NP stabilized W/L bijels labelled by sample age t_w. As t_w increases, the dynamics slow down, which again shows that the sample is aging. Much like the MP stabilized W/L bijel, there is a two step decay present in the correlation functions. However, this is not as clear as in the MP case (i.e. the early age curves look more like single decay, but are in fact double decay). This is probably because of the reduction in contrast due to the use of the 5mm cell – g_2 in the NP case only varied between $\approx$1.035 and $\approx$1.009, compared to a variation of between $\approx$1.28 and $\approx$1.008 in the MP case. Again, the second decay slows down faster than the first, resulting in a plateau which emerges between the 1 & 2 hour measurements at a value of ≈ 0.6 here as opposed to ≈ 0.9 in the MP case. The difference in height is likely due to the larger number of scattering events from the bijel channel 'walls' in this experiment because of the thicker 5mm cell - the height of the plateau gives an indication of the proportion of fast vs slow scatterers present in the system [152]. The lower the plateau, the greater the fraction of light decorrelated by the fast scatterers (in this case probably the thermally-oscillating walls of the bijel network). Almost complete decorrelation is observed when the sample is almost a day old, but the

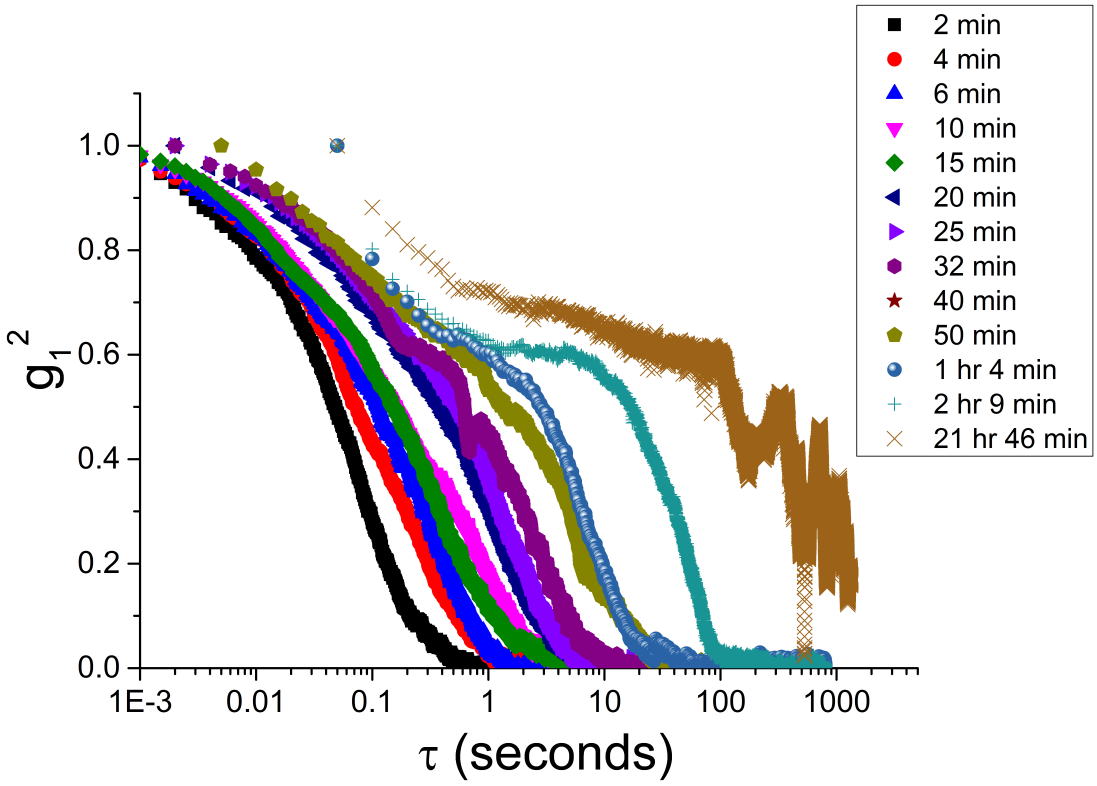

Figure 5.3: The correlation functions of water/lutidine (W/L) bijels stabilized by nanoparticles (NPs, r = 63 nm) as a function of delay time τ, labelled by sample age.

oscillatory pattern indicates that this is likely due to low-frequency vibrations or knocks of the experimental setup, with the now (essentially) solid sample unable to mask them with faster dynamics.

NM/ED

Figure 5.4 shows the correlation functions of the MP_2 stabilized NM/ED bijels labelled by sample age t_w. Like the W/L bijels there is a two-step decay, with a plateau emerging between the 2 hr 1 min & 3 hr 2 min measurements at a value of ≈ 0.8, which moves to higher values after subsequent aging. Complete decorrelation at high t_w cannot be ruled out as the 1 day 1 hr measurement was only taken for $\approx$ 2000 seconds, and again the oscillatory pattern suggests that vibrations of the equipment were present during the measurement. However, the correlation function at high t_w is more similar to the MP W/L bijel rather than the NP W/L bijel because of the higher value at τ = 1000 seconds.

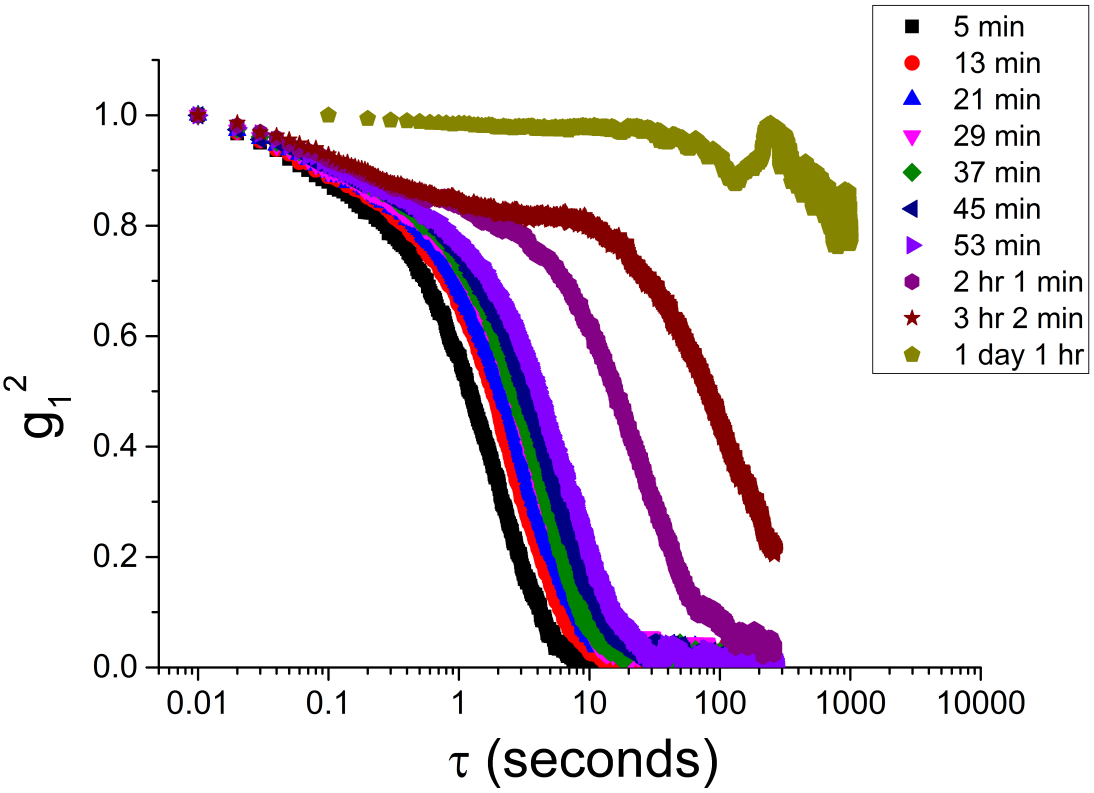

Figure 5.4: The correlation functions of nitromethane/ethanediol (NM/ED) bijels stabilized by microparticles (MPs, r = 290 nm) as a function of delay time τ, labelled by sample age.

5.4.2 Rescaled curves and aging

To quantitatively characterize and compare the aging of the bijel samples, we have measured each correlation function's characteristic decay time τ_d, which we define as $|g_1(\tau_d)|^2 = 0.5$, and replotted the curves as a function of τ/τ_d. We use a single characteristic time for each curve because we are interested in the dynamical aging of the entire system and not focussing on any individual decay process. Plotting the data in this way allows an easier comparison between samples of different ages. We also plot τ_d as a function of t_w to measure the aging rate.

Figure 5.5 shows the rescaled correlation functions (a)-(c) and the characteristic decay times plotted as a function of bijel age (d). In all cases, the correlation functions change shape in various ways as the sample age. In the MP W/L bijel case (a), the shape of the first decay becomes flatter and the second decay becomes increasingly compressed. In the NP W/L bijel case (b), the shape of the first decay becomes flatter and the second decay becomes stretched, until the plateau emerges at which time it reverts back to the shape exhibited by the

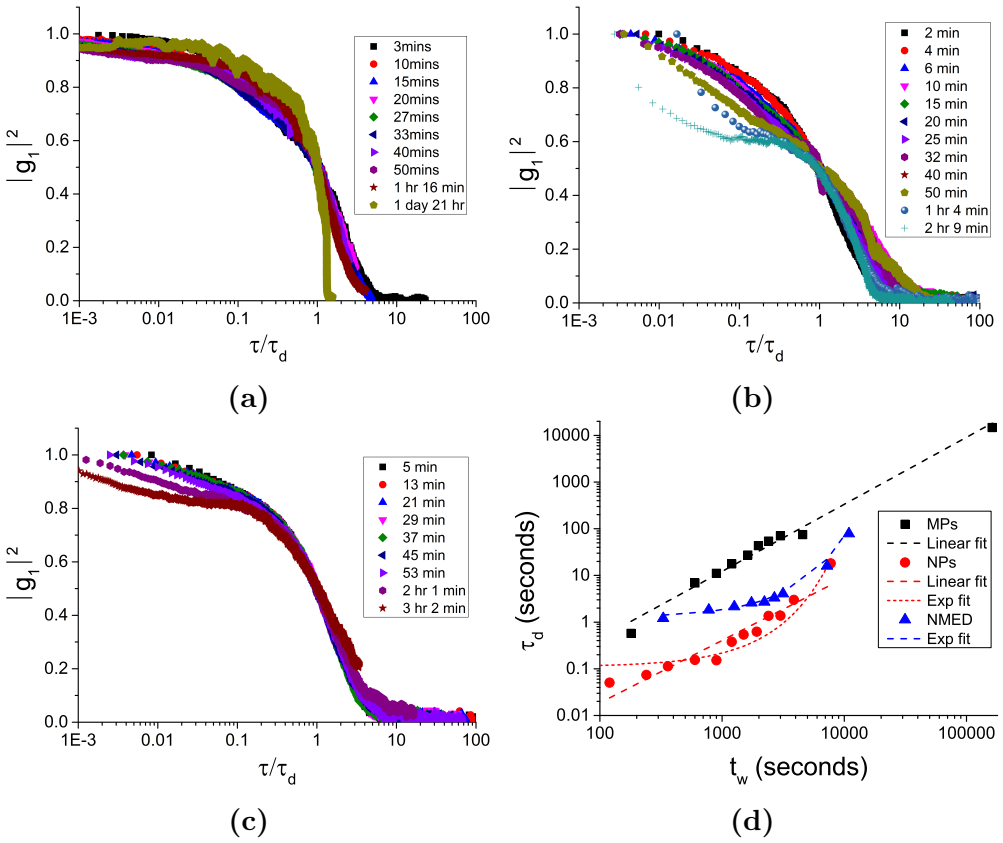

Figure 5.5: The rescaled correlation functions as a function of τ/τ_d for (a) W/L with MPs, (b) W/L with NPs and (c) NM/ED with MPs. τ is the delay time and τ_d is the delay time at which the value of the correlation function is 0.5. (d) The dependence of τ_d on sample age for the three systems presented in (a)-(c).

2 min sample. In the NM/ED case (c), the curves corresponding to $t_w < 1$ hour superimpose almost exactly, with a slight flattening of the first decay and a slight stretching of the second. A perfect superposition on to a master curve is a characteristic of universal aging [140, 144, 153, 154].

The dependence of the characteristic decay time τ_d with bijel age t_w in the MP W/L case follows a power-law behaviour ($\tau_d \sim t_w^\beta$, with $\beta = 1.44(6)$). In the NM/ED case the behaviour is exponential. In the NP W/L case, the behaviour is either a power law (with $\beta = 1.36(14)$) or exponential – both are relatively poor fits. However, a basic analysis of the sum of the square of the residuals suggests the exponential fit is the better of the two (61 for the exponential fit and 183 for the linear fit).

As expected, τ_d values in the NP case are about an order of magnitude smaller, given that the particles are about 7 times smaller and will move quicker under

thermal motion. Power-law dependence with an exponent of 1 is a characteristic of the universal aging picture of DLCA gels in the late-stage [140, 153, 154], with early-stage dependence predicted to be exponential. The exponential dependence is attributed to particle cage-forming [155]. Therefore, only the NM/ED bijel (arguably also the NP W/L bijel) shows signs of universal aging properties, assuming that the time window we have studied is indeed the early-stage. The W/L bijels both age faster than the NM/ED bijel, and due to the power-law dependence (of τ_d on t_w) appear to be in the late-stage of aging. Note however that in the universal aging picture (for DLCA gels) the power law dependence is expected to emerge after an initial exponential dependence which allows τ_d to catch up with t_w, at which point τ_d simply follows t_w linearly since it obviously cannot exceed t_w, whereas here the power-law dependence is observed in a range $\tau_d < t_w$. In other words, we assume here that we are observing the early stage of bijel aging, since all relaxation times are less than the sample ages, even though the MP W/L bijel shows power-law aging, which would typically arise in the late stage. Also, we expect in the late stage for the power law exponent to be 1, not 1.44 or 1.36.

One major difference between these two systems is their monogelation behaviour – the W/L bijels form a monogel (after a minute in the case of NPs and after about 40 minutes in the case of MPs, evidenced by the survival of the particle network after remixing the liquid phases [91]) whereas the NM/ED bijel doesn't [90]. This suggests that the monogelation process could have something to with this differing aging behaviour, especially since there is a further difference between the MP (slow monogelling) and NP (fast monogelling) W/L samples, in that the latter's behaviour is somewhere between a power-law and an exponential. However, since the MP and NP W/L correlation functions change differently over time, and the NM/ED curves also change shape eventually, this suggests that there is another aging mechanism present, over and above monogelation. To identify the possible mechanisms at play, we can extract the mean-squared displacements (MSDs) as a function of delay time τ and look at the nature of the dependence of MSD on τ.

5.4.3 Mean-squared displacements and l^*

To investigate the nature of the scatterer dynamics, we can use equation 5.4 to calculate the mean squared displacements (MSDs) as a function of delay time τ

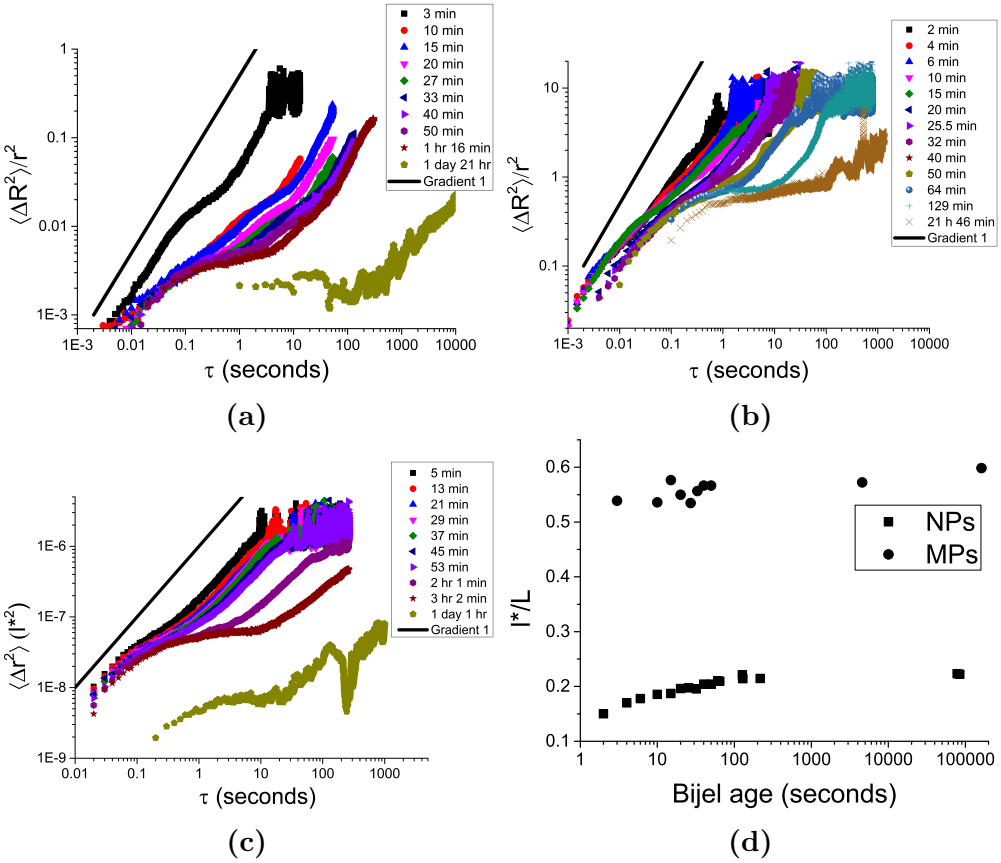

Figure 5.6: The mean-squared displacements (MSDs, $\langle \Delta R^2 \rangle$) for the correlation functions presented in the previous sections, labelled by sample age, with a solid line of gradient 1 added for illustration purposes. (a) Water/lutidine (W/L) with microparticles (MPs), (b) W/L with nanoparticles (NPs) and (c) Nitromethane/ethanediol NM/ED with MPs. (d) shows the photon mean free path l^* as a function of sample age for both W/L systems.

for all of the correlation functions presented in the previous section. This is done by taking the natural logarithm of the correlation functions and rearranging for $\langle \Delta R^2 \rangle$. To reiterate, this approach assumes that the diffusion approximation for the photon path length distribution is valid. The dependence of the MSDs on time can indicate the type of motion - a gradient of 1 indicates diffusive motion, whereas sub/super-diffusive motion would be indicated by a gradient of < 1 and > 1 respectively [12].

Figure 5.6 shows the MSDs for the MP W/L bijel (a), NP W/L bijel (b) and NM/ED MP bijel (c) labelled by sample age, with a solid line of gradient 1 added for illustration purposes. The photon mean free path l* is plotted as a function of bijel age in (d).

In the MP_1 W/L case (a), diffusive motion is observed in the early and late time of $t_w = 3$ min, whereas for all $t_w > 3$ min the early time motion is sub-diffusive and the late time motion is diffusive. Only for $t_w = 1$ day 21 hr is the late time motion sub-diffusive. In-between the early and late time motion the MSDs level off as the samples age. Note that the range of MSDs is below the particle diameter, which in squared units is 5.4 $\times 10^{-13}$ m^2.

In the NP W/L case (b), the early time motion remains roughly diffusive until $t_w = 32$ min, at which point it becomes sub-diffusive. The late-time motion is mostly slightly sub-diffusive (the exception being $t_w = 129$ min). Like (a), in-between the early and late time motion the MSDs level off as the samples age. But unlike (a), the range of MSDs exceeds the particle radius.

In the MP_2 NM/ED case (c), the MSDs are very similar to (b) in that the early time motion is diffusive up to about $t_w = 53$ min, becoming sub-diffusive after that, while the late time motion is mostly diffusive until about $t_w = 2$ hr 1 min when it becomes sub-diffusive. Like (a) and (b), the MSD levels off between the early and late time as the samples age.

Figure 5.6(d) shows how the photon mean free path l^* changes with sample age for the MP and NP stabilized W/L bijels. In the MP case, l^* begins at ≈ 0.55 mm and increases slightly to ≈ 0.6 after 10^6 seconds. This is rather low, as $L/l^* \approx 2$. In the NP case, l^* increases from ≈ 0.75 to ≈ 1.1 mm over the course of 10^6 seconds. These values are more acceptable as $L/l^* \approx 5$. The cause of the change in l^* could either be coarsening of the bijel macrostructure, or the sedimentation of 'free' particles, i.e. particles not attached to the liquid-liquid interface, or a combination of both. We do not observe significant coarsening of NP stabilized bijels (Chapter 3), so we turn to the sedimentation times shown in section 5.3.4 which may be of use here. We expect that most of the free particles will have sedimented by 10^4 seconds in the case of NP W/L, which is in the region that l^* has levelled-off. The slight increase in l^* in the MP bijel could also be caused by sedimentation, but since there are fewer free particles in an MP bijel sample, this is more likely due to coarsening.

5.5 Discussion

Here we summarize the results and discuss how they add to our understanding of bijel dynamics and aging, while pointing out remaining questions to be answered. Previous simulation and experimental studies on bijels have shown a range of macroscopic aging behaviours. For example, in simulations the characteristic domain size L increases during the phase separation and appears to saturate when the bijel is formed but may or may not continue to increase beyond this point [5, 11, 45, 48]. This is experimentally observed but again the behaviour of L beyond about 100 seconds is unknown [1]. The elastic modulus G' has been shown to increase over time in the case of MP W/L bijels, coinciding with the time observed to be required for the formation of a monogel [91], and the non-monogelling NM/ED system G does not show an increase over time [90]. Another bijel study, using graphene oxide sheets as the interfacial species, suggests that the enhanced rigidity of the structure and the interfacial arrest may be caused mainly by the interfacial rheological activity of the particle layer [74]. Measurements of the distributions of interfacial curvatures have shown a marked aging behaviour in the case of MP W/L bijels and to a lesser degree in NP W/L bijels, with NM/ED bijels showing next to no aging (Chapter 4).

In terms of dynamics, simulations have suggested that particles' diffusive motion at early delay times is retained as the system ages but that the particles' range of MSD decreases monotonically with age (i.e. waiting time t_w) [11]. At long t_w and long delay time, a slight upward curvature of the MSD is observed, suggesting some kind of super-diffusive motion. Experimentally, particle dynamics in a bijel on a microscopic level have never been studied before the current investigation.

The results presented in this chapter begin to explore the microscopic dynamics and aging of the interfacial particle network in a bijel, which are presumably linked to the macroscopic behaviour. In all cases studied, the microscopic dynamics follow a two-step decay, with a clear plateau emerging after 1-3 hours. Figure 5.7 shows the correlation functions with the clear plateaus from the three different systems studied. These dynamics are also seen for DLCA gels, whereby the initial decay to a plateau is caused by thermally-activated modes of the gel network, and the final decay is attributed to the relaxation of randomly located internal stresses [140, 156]. Moreover, these dynamics are seen not only in DLCA colloidal gels, but a range of other jammed materials e.g. micellar polycrystals and concentrated emulsions [144].

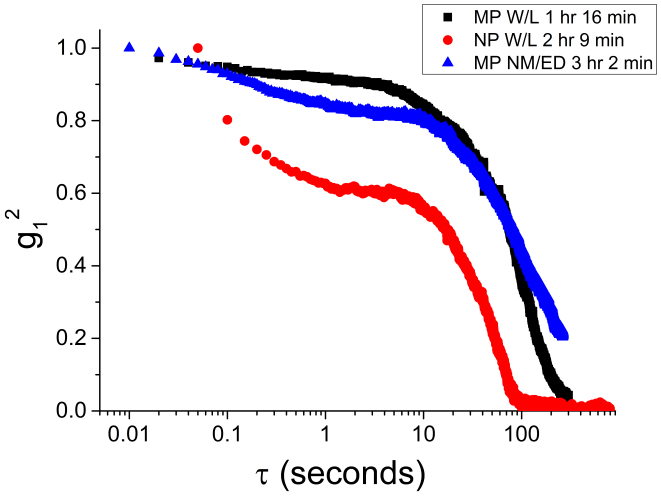

Figure 5.7: Correlation functions for the three systems studied as a function of delay time τ, at the sample age which shows a clear plateau. Water/lutidine with microparticles (black squares), with nanoparticles (red circles) and nitromethane/ethanediol with microparticles (blue triangles).

In DLCA gels, it is claimed that the origin of the internal stresses is the occurrence of micro-collapses within the gel network, whereby particles rearrange locally and create a force dipole [140, 156]. It was observed in [140] that these micro-collapses are due to gel syneresis, but this is only one possible source. The relaxation of these stresses tends to create new stresses with longer relaxation times, explaining the dependence of τ_d on t_w i.e. the aging behaviour [156]. However, the nature of the dependence of τ_d on t_w varies from system to system [144].

Returning now to the bijel systems studied here, we clearly see the slowing down of the dynamics as the bijels age, with τ_d increasing with t_w. In addition, the aging behaviour shows a clear demarcation between the W/L (monogel) and NM/ED (non-monogel) systems. The W/L systems' correlation functions do not rescale on to a master curve and show a linear dependence of τ_d on t_w (in the case of MPs) or a somewhat linear dependence (in the case of NPs), whereas the NM/ED system's correlation functions rescale almost entirely on to a master curve and τ_d shows an exponential dependence on t_w. In this respect, the NM/ED bijel shows features of universal aging [140, 144], whereas in the case of the W/L bijels, other factors appear to be in play.

It could be that we are seeing the same microscopic behaviour in the bijel as is observed for DLCA gels and other systems – the relaxation of internal stresses. If so, there would be a few possible sources for the internal stresses.

They could be built-in to the system during the jamming transition of the interfacial particles due to the liquid-liquid coarsening and then relax to allow the formation of locally crystalline order in the particle layer as proposed in the original simulations [5]. Such relaxation has been observed in simulations of anisotropic particles (ellipsoids) at L-L interfaces [61] and has been attributed to Laplace pressure differences across the interface. Although here we are using ostensibly isotropic spherical particles, we know there to be some degree of surface roughness, anisotropy and chemical heterogeneity (Chapter 2) and hence rearrangement/relaxation due to this effect is a distinct possibility due to local capillary forces [104, 157, 158]. Small rearrangements of particles could also be caused by the interfacial forces pushing neighbouring particles in to their primary van der Waals minimum (i.e. monogelation [91]) or be induced by syneresis as seen in Ref. [140]. New stress sites could be produced by the subsequent action of the particle layer on the interface (bending moments [1, 119]). It is also possible that any combination of these potential factors are active in creating and relaxing internal stress sites. Note that the major differences between bijels and DLCA gels is involvement of the L-L interface, which both pushes particles together and is (potentially) acted upon by the particle layer, as argued in Chapter 4.

In addition, there is an important difference between the measurement methods (DLS vs DWS) which has to be considered when comparing these two systems (DLCA gels vs bijels). DLS allows a choice of wavevector and hence a choice of lengthscale which is to be probed. This allows the measurement of the range of lengthscales over which these micro-collapses occur. It has been found that they occur over lengthscales comparable to the cluster size, i.e. many multiples of the particle size r. However, in DWS, the probe lengthscale is essentially fixed by the wavelength of light and the concentration of scatterers (via l^*), which is roughly $0.01r$. Hence, the individual particle motion required for the decay-to-zero of the correlation function is drastically less than that for a DLCA gel studied by DLS. This means that we do not know the range of lengthscales over which the particles are (potentially) rearranging in a bijel, but can say with some certainty that the particles are indeed moving over distances comparable to their size.

Now, to try and explain the separation of aging behaviours amongst the systems studied, we carefully consider each case in turn and make conjectures about the link to the possible microscopic mechanisms. For example, since we know that the NM/ED bijel doesn't monogel or show a change in interfacial curvature over time, we can potentially see why its aging behaviour most closely resembles that

of DLCA gels. We argue that in the case of NM/ED the only possible source of internal stresses are the jamming transition and syneresis and therefore expect the system to age in a similar fashion to DLCA gels. The fact that the correlation functions don't completely overlap could be due to the extra stresses imposed by the jamming transition and/or the differing nature of the stresses imposed by syneresis.

Now, if we look at the W/L bijels, we can see the effect of the monogelation and/or impact of the bending moments on the aging behaviour. We see that the system with the most potential sources of creation of internal stresses (W/L) age faster than the system with only two (NM/ED) – τ_d increases with t_w as a power law with exponent $\beta > 1$.

To differentiate between W/L MP and W/L NP, we consider the following. As the W/L MP bijel ages it also goes through the process of monogelation – this leads to the fastest aging of all. For the W/L NP bijel, the aging is slightly slower, and the data is somewhere between a power-law and an exponential. This may be because the system has already (mostly) formed a monogel (Chapter 3), i.e. for t_w >1 minute, the system is a monogelled state, whereas for MPs the system is a monogel for $t_w > 30$ minutes and is forming a monogel up to that point. It could also be because the particle layer doesn't express as large a bending moment on the interface [2] (from Chapter 4), or due to the larger van der Waals attraction between particles [12].

Unfortunately, a fuller understanding of the microscopic dynamics and its influence on the aging of bijels eludes us at this point. As stated above, we propose several possible microscopic mechanisms which could be in play and outline why the dynamical behaviour would be similar to DLCA gels, but the exact link between microscopic mechanisms and dynamical aging is yet to be established, both in terms of which mechanisms contribute and to what extent they contribute. Experimentally, this will be difficult to ascertain unless we can improve imaging resolution to be able to look at the movement of individual particles and small sections of the L-L interface. Simulations could however shine some light on the issue by building in various combinations of microscopic mechanisms and studying the effect on the interfacial particle motion.

5.6 Conclusions

Bijels have been shown to exhibit dynamical aging properties, placing them within the larger class of jammed materials [144]. The nature of the aging shows variations between different particle sizes and liquid-liquid combinations. Contrary to previous assumptions, the particles in the jammed layer continue to move over a distance of 1 - 10% (MPs) and 10% - 100% (NPs) of their radius after the (water/lutidine) bijel is formed, with the distance reducing as the bijel ages, but still significant even after 1 - 2 days. However, it is not clear whether this motion is cooperative (i.e. large interfacial regions moving together) or independent (i.e. local particle rearrangements).

The dynamics of bijels which form a monogel (water/lutidine bijels) slow down either linearly with aging time (MP stabilized) or somewhere between linearly and exponentially (NP stabilized), whereas the non-monogelling system (nitromethane/ethanediol) slows down exponentially with aging time. The latter is similar to the aging behaviour of DLCA gels as elucidated via DLS, which is attributed to the relaxation of internal stresses [140]. It could be that the aging behaviour of the monogelling systems is due to the same mechanisms but with different and/or additional sources of internal stresses. Interestingly, this separation of dynamical aging behaviour (in terms of monogelation) is not observed when monitoring the time-dependence of interfacial curvature distributions (Chapter 4). Instead, the microparticle water/lutidine system is the only system that shows unambiguous signs of aging when looking at changes in interfacial curvature only.

Although the monogelling systems exhibit power-law behaviour, the exponents are larger than expected and in this respect do not fit into the universal picture for aging [140, 153, 154]. In addition, since in all cases the correlation functions cannot be perfectly superimposed, this implies that there are other factors contributing to the aging behaviour which are not found in other systems like DLCA gels. This may include the monogelation process, the jamming transition and/or the presence of the liquid-liquid interface. Further work, including higher resolution imaging and simulations, will be required to separate out the range of factors present to identify the causes of the varying aging behaviours. For example, the identification of the elastic modes of the interfacial particle network may help differentiate between the dynamics of the particle network and the individual particles.

5.7 Acknowledgements

We would like to thank Joe Tavacoli for assistance with the DWS experimental setup and useful discussions, Jochen Arlt for assistance with the use of the fast CCD camera, and Katherine Rumble for preparation of the NM/ED bijels.

Chapter 6

Bijels stabilized by bimodal particles

6.1 Abstract

Experimental studies on bijels so far have stabilized the structure with monomodal particles, whereas simulations have explored the stabilization with bimodal particles revealing some interesting behaviour, including segregation by size. In addition, the spectrum of behaviour as a function of particle size in the monomodal case can be further probed by performing experiments with bimodal particles. Here we develop both an experimental protocol for the preparation of bimodal bijels and a theoretical framework which allows us to quantitatively estimate the relative interfacial uptake fractions of both particles. We also examine the formation kinetics and look for evidence of particle segregation on the interface. We find that the uptake of nanoparticles (NPs) is roughly half that of microparticles (MPs), that the bimodal bijel takes significantly longer to jam in to its final structure, and limited evidence of particle segregation. Intriguingly, we observe that the quench rate plays a larger-than-expected role in determining the final structure, with faster quenches producing bijels with larger lengthscales, providing a novel new control parameter over and above particle size, volume fraction and contact angle.

6.2 Introduction

The preceding chapters in this thesis, along with some published literature, have outlined some very intriguing differences in bijels stabilized by different sizes of particles (i.e. nanoparticles, NPs vs microparticles, MPs). For example, the scaling law $L \propto r/\phi$ (where L is the characteristic interfacial separation, r is the particle radius and ϕ the particle volume fraction) in the case of NP stabilized bijels has a larger prefactor than in the case of MP stabilized bijels (Chapter 3), and NPs are more successful at stabilizing bijels than MPs when varying the quench rate [1]. However, these experimental studies have only ever used one (principle) size of particle to stabilize the structure. Given these interesting differences between NPs and MPs, it seems pertinent to explore the properties of bijels stabilized by a mixture of both. Doing this could give us greater insight into their respective individual behaviours.

The original simulations on bijels looked at the case of stabilization by a bimodal particle population, with the aim of ruling out a potential explanation for the late-time behaviour of $L(t)$ [5]. A bimodal particle population suppresses the potential formation of semicrystalline rafts at the interface, which is a candidate explanation for the residual (slow) dynamics. The authors observed particle segregation by size on the interface which may even be a slower process than the formation of the rafts, meaning that the approach was unable to rule-out the raft formation as an explanation for the late-time dynamics. Importantly, such segregation has not been observed experimentally.

In Chapter 3 we presented results which suggest that the interfacial uptake of MPs is greater than that of NPs ($\alpha_{\mathrm{MP}} > \alpha_{\mathrm{NP}}$, where $0 \leq \alpha \leq 1$) but had no easy way of directly or indirectly quantifying these values. We also looked at formation kinetics to understand why MPs fail to produce bijels at slow quench rates. In this chapter we present a scheme by which the relative uptake rates of NPs vs MPs can be quantified and measure the formation kinetics for bimodal bijels to compare to the monomodal case. In addition, we explore the effect of the quench rate on the final bimodal bijel lengthscale and how bijel formation depends on the total volume fraction, and relative volume fraction of particle species.

We find that the relative interfacial uptake of NPs is roughly half that of MPs, which corroborates the different scaling gradients as shown in Chapter 3. The bimodal bijel takes longer to jam than an equivalent bijel made with only one

size of particle, suggesting that in the bimodal case the particles either have more opportunity for rearrangement before arriving at the jammed metastable state, or take longer to do so (in comparison to the monomodal case). While we observe that the NPs and MPs are roughly dispersed throughout the bijel structure equally, we do see a stronger fluorescence signal from MPs around droplets, possibly as a result of the stronger MP bending moment towards a non-zero interfacial mean curvature, corroborating results from Chapter 4. Intriguingly, we also observe that when the relative amounts of NPs and MPs present is similar, the lengthscale is dependent on quench rate, which we can explain by way of considering the quench rate as a particle-selector. This phenomenon potentially provides a new way of tuning bijel lengthscale over and above particle size, volume fraction and contact angle.

The following sections are arranged as follows. In Section 6.3 we recap the theoretical framework devised for understanding monomodal bijels and develop this framework for quantifying relative uptake fractions in a bimodal bijel. In Section 6.4 we document a new experimental protocol for preparing bimodal bijels and list our chemicals and procedures for preparing the particles. In Section 6.5 we proceed to calculate relative particle uptake fractions, explore the effect of quench rate on the final bijel lengthscale, quantify the formation kinetics and look for particle segregation on the interface. We then summarize the results in Section 6.6 and discuss how they fit in to our understanding of bijel formation, finishing with the overall conclusions in Section 6.7.

6.3 Theory

6.3.1 Monomodal bijel

The area of liquid-liquid (L-L) interface A_{LL} in a bijel covered by particles (assuming contact angle $\theta = 90°$) is given by

$$A_{\mathrm{LL}} = \frac{\pi r_m^2 N_{\mathrm{int}}}{\phi_{\mathrm{2D}}} \tag{6.1}$$

where N_{int} is the number of particles attached at the interface, ϕ_{2D} is the 2D packing fraction and r_{m} is the radii of the monomodal particles. The number of

particles at the interface is given by

$$N_{\text{int}} = \alpha_{\text{m}} N \tag{6.2}$$

where α is the fraction ($0 < \alpha < 1$) of particles added to the sample which end up attached to the interface, and N is the total number of particles added to the sample,

$$N = \frac{\phi_{\text{m}} V_{\text{tot}}}{\frac{4}{3}\pi r_{\text{m}}^3} \tag{6.3}$$

where ϕ_{m} is the volume fraction of monomodal particles added and V_{tot} is the total sample volume. We then make the substitution $\frac{V_{\text{tot}}}{A_{\text{LL}}} = CL_{\text{m}}$, where C is a geometrical constant and L_{m} the average interface separation in the monomodal bijel. Combining these expressions gives

$$L_{\text{m}} = \frac{1}{C}\frac{\phi_{\text{2D}}}{\alpha_{\text{m}}}\frac{r_{\text{m}}}{\phi_{\text{m}}} \tag{6.4}$$

which can be rearranged for the unknown quantity C

$$C = \frac{\phi_{\text{2D}} r_{\text{m}}}{L_{\text{m}} \alpha_{\text{m}} \phi_{\text{m}}} \tag{6.5}$$

6.3.2 Bimodal bijel

The area of L-L interface covered by particles in a bimodal bijel will be the sum of the areas covered by MPs and NPs, given by

$$A_{\text{LL}} = \frac{\pi r_{\text{NP}}^2 N_{\text{NP,int}}}{\phi_{\text{2D}}} + \frac{\pi r_{\text{MP}}^2 N_{\text{MP,int}}}{\phi_{\text{2D}}} \tag{6.6}$$

Making the same substitutions as before, we arrive at

$$L_{\text{b}} = \frac{\phi_{\text{2D}}}{C}\left(\frac{\phi_{\text{NP}}\alpha_{\text{NP}}}{r_{\text{NP}}} + \frac{\phi_{\text{MP}}\alpha_{\text{MP}}}{r_{\text{MP}}}\right)^{-1} \tag{6.7}$$

where L_{b} is the average interfacial separation in the bimodal bijel. Finally,

$$C = \frac{\phi_{\text{2D}}}{L_{\text{b}}}\left(\frac{\phi_{\text{NP}}\alpha_{\text{NP}}}{r_{\text{NP}}} + \frac{\phi_{\text{MP}}\alpha_{\text{MP}}}{r_{\text{MP}}}\right)^{-1} \tag{6.8}$$

6.3.3 Measuring relative particle uptake

In order to proceed, a couple of assumptions must be made. First, we assume that the geometrical constant in both cases is comparable, i.e. that C is roughly constant and not heavily dependent on the size of the stabilizing particles. Although we expect C to depend on morphology (i.e. bijel vs emulsion), we are comparing two systems of identical morphology here (bijel vs bijel). This assumption is further justified by the results (see section 6.5.1). Second, we assume that the monomodal particle uptake fraction does not significantly change upon the introduction of the second particle species, i.e. that both species adsorb to the interface independently and do not interact. When we perform the experiments we fix the relevant parameter with respect to these assumptions which is the relative maximal areas of the particles – to a ratio of 1:1 (i.e. we fix the ratio $r_1/\phi_1 = r_2/\phi_2$, see Section 6.5.1). This should mitigate any impact of these assumptions being incorrect. For example, if C does depend on particle size, or the particles interact when attaching to the interface, changing the maximal particle ratios from sample to sample would potentially skew results. Hence, we fix the *relative* area, but vary the *total* area to see how the bijel lengthscale changes.

Now we can substitute the expression for C from the monomodal bijel into the expression for the bimodal bijel, and we arrive at

$$\frac{\alpha_{\mathrm{NP}}}{\alpha_{\mathrm{MP}}} = \frac{L_{\mathrm{m}} r_{\mathrm{NP}} \phi_{\mathrm{m}}}{L_{\mathrm{b}} r_{\mathrm{MP}} \phi_{\mathrm{NP}}} (1 - \frac{L_{\mathrm{b}} \phi_{\mathrm{MP}}}{L_{\mathrm{m}} \phi_{\mathrm{m}}}) \tag{6.9}$$

Note that all of the quantities on the right hand side of equation 6.9 can be measured and hence a value of $\alpha_{\mathrm{NP}}/\alpha_{\mathrm{MP}}$ can be arrived at experimentally.

6.4 Methods

6.4.1 Particle synthesis

The particles used here were prepared according to the methods outlined in Chapter 2. Stöber silica particles of radius r = 44 or 50 nm (nanoparticles, NPs) and 348 nm or 367 nm (microparticles, MPs) were labelled with RITC and FITC respectively. These sizes were obtained from TEM analysis.

6.4.2 Bimodal bijel preparation

Bimodal bijels were prepared using a method adapted from the standard bijel method as outlined in Chapter 2. The specific method is outlined here. A mass m_1 of NPs of radius r_1 was dispersed in a volume V_1 of deionised water as per the standard method. Subsequently, a mass m_2 of MPs of radius r_2 were dispersed in a volume V_2 of deionised water as per the standard method. Dispersion was carried out in this order due to the shorter dispersion time for MPs, minimising the time between particle dispersion and lutidine addition for both dispersions. With both particles dispersed, a fraction χ of the NP dispersion was added to the MP dispersion to give a number ratio of NP:MP 1:1. χ is given by the following equation;

$$\chi = \frac{m_2 \rho_1 V_1 r_1}{m_1 \rho_2 V_2 r_2} \tag{6.10}$$

where ρ is the particle density. With the total amount of water known (i.e. $V_1 + V_2$), lutidine (either without dye, or with Nile Red or Nile Blue Blue at $\approx$ 10 μM concentration) was added to give a water:lutidine ratio of 72:28 as per the standard method. The bijel mixture was then transferred to a 1mm path length cuvette (Starna) and quenched as per the standard procedure, depending on the desired rate (Chapter 2).

6.4.3 Imaging

Bijels were imaged using fluorescence confocal microscopy as per the standard method (Chapter 2). When looking for particle segregation on the interface however, bare lutidine was used to allow the signal from the RITC on the NPs to be seen and not swamped by the signal from either Nile Red or Nile Blue. Note that we do not expect the choice of dye for the liquids to affect the physics of the system, especially at such low concentrations [159] (see Chapter 2).

FITC has an excitation/emission wavelength of 495/517 nm. RITC has an excitation/emission wavelength of 550/573 nm. The FITC/RITC was excited using the 488/555 nm laser. To optimally separate the signals from FITC and RITC, emission wavelengths of 560 nm and above were sent to PMT-2 while wavelengths less than 550 nm were sent to PMT-1. Dichroic mirrors and emission filters were used to achieve this. To reduce the amount of FITC signal leaking in to the second channel, the power of the 488 nm laser was reduced relative to the

555 nm laser and the gain of PMT-1 increased (to maintain some image quality).

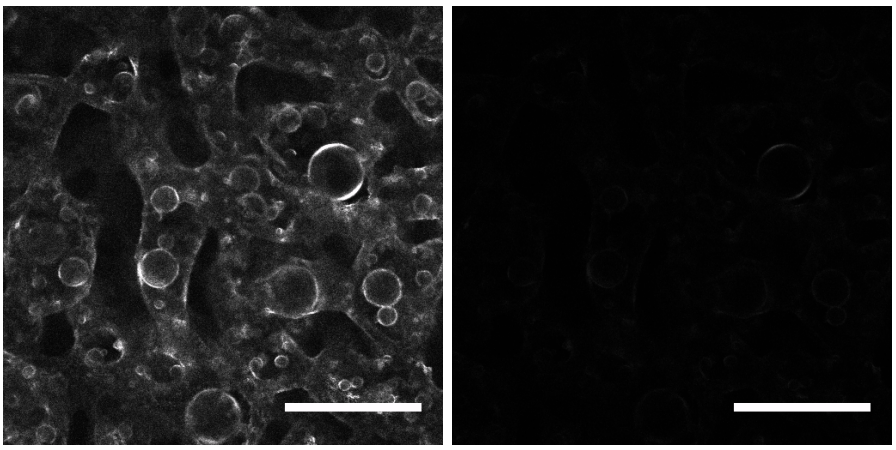

(a) **(b)**

Figure 6.1: Example fluorescence confocal micrographs of a bimodal bijel with only the 488 nm laser activated. (a) is the signal arising from the FITC being detected on PMT-1, and (b) is the leaked signal from the FITC being detected on PMT-2.

To illustrate the amount of leakage under this scenario, Figure 6.1 shows the signal from the FITC in PMT-1 (a) and the leaked signal in PMT-2 (b) with the 555 nm laser (which would excite the RITC) turned off. Hence, under this protocol the signals are suitably separated.

6.5 Results

6.5.1 Interfacial uptake fractions

In this section we analyze lengthscale measurements performed on carefully prepared monomodal/bimodal bijel sample pairs in order to arrive at an estimate of the relative interfacial uptake of nanoparticles (NPs) vs microparticles (MPs). In preparing the bimodal bijels, we fix the relative theoretical (maximum) area fraction of particles at 50:50, so that $\phi_1 r_2 = \phi_2 r_1$ ($A_{\mathrm{MP,max}} = A_{\mathrm{NP,max}}$). Doing so allows us to attribute the change in L to a difference in the uptake fractions α_1 and α_2, as according to Equation 6.9. Also, fixing the relative area fractions in this way should nullify any effect of particle adsorption competition and/or dependence of the geometrical parameter C on the particle types.

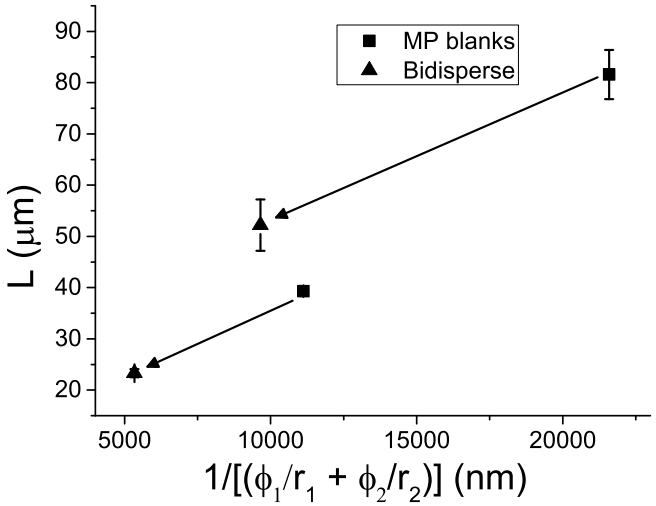

Figure 6.2: The lengthscales of bijels stabilized by a monomodal particle population (r = 367 nm, squares) and a bimodal particle population (r_1 = 367 nm and r_2 = 50 nm, triangles). The volume fraction of the second (smaller) particle species is equal to the equivalent volume fraction of large particles modified by the difference in radius, i.e. $\phi_2 = r_2\phi_1/r_1$.

Figure 6.2 shows the lengthscales of two bimodal bijels (triangles) with the corresponding 'blanks' – a bijel made with the same amount of MPs but no NPs. Upon addition of a volume fraction of NPs, given by $\phi_{\mathrm{NP}} = \phi_{\mathrm{MP}} r_{\mathrm{NP}}/r_{\mathrm{MP}}$, to the blanks the lengthscales are reduced from 82(5) μm and 39(1) μm to 52(5) μm and 23(1) μm respectively. Using Equation 6.9 we can estimate the value of $\frac{\alpha_{\mathrm{NP}}}{\alpha_{\mathrm{MP}}}$ by substituting in the values of L, ϕ and r. This gives us estimates of 0.4(2)

and 0.63(9) on L reductions of $\approx 36\%$ and $\approx 41\%$ respectively. Note that due to experimental error, in the bimodal samples the actual $A_{\mathrm{MP,max}}$ values were 0.91 and 0.88 times $A_{\mathrm{NP,max}}$, so there was a slightly larger maximum possible area of NPs in both cases.

The estimates of relative interfacial uptake both imply that $\alpha_{\mathrm{NP}} < \alpha_{\mathrm{MP}}$, which is what we expect from inspecting the monomodal bijel graphs of L vs $1/\phi$ and the comparison of fluorescence confocal images in Chapter 3. The gradient of the straight-line fitting to the NP data is twice that of the MP data which, assuming other variables constant, implies a lower interfacial particle uptake. Indeed, as the average value of the two independent estimates presented here of $\frac{\alpha_{\mathrm{NP}}}{\alpha_{\mathrm{MP}}}$ is ≈ 0.52, this corroborates the fact that the gradient of the NP data is twice that of the MP data, and suggests that the other variables in the prefactor (of which one is the geometrical constant C) are not significantly changed when stabilizing a bijel with a bimodal particle population. In other words, assuming that C does not change has allowed us to arrive at the same value for $\frac{\alpha_{\mathrm{NP}}}{\alpha_{\mathrm{MP}}}$ using two separate methods.

Also, $\alpha_{\mathrm{NP}} < \alpha_{\mathrm{MP}}$ is implied by a more rudimentary and semi-quantitative analysis of the data in Figure 6.2. When we add an area of NPs equivalent to the area of MPs, we expect a reduction in L of 50% – the same reduction which would result if we added the same (extra) area of MPs instead, according to $L \propto r/\phi$. As the reduction in L in both cases was less than 50%, this implies that a smaller fraction of the added NPs (than that expected for the MPs) attached to the interface. Note that all of the arguments here are corroborated by the qualitative observation made in Chapter 3 that the confocal micrographs of NP stabilized bijels show a stronger signal from the liquid channels than the MP stabilized bijels, suggesting a greater number of free particles in the NP case.

Thanks to these measurements and calculations we now have a reasonable estimate of the relative uptake fraction $\alpha_{\mathrm{NP}}/\alpha_{\mathrm{MP}}$ of ≈ 0.52, and have ascertained that the geometrical constant C is roughly the same for monomodal (MP or NP) and bimodal bijels (MP and NP), at least when they are both quenched at a fast rate. However, we have seen from Chapter 3 that the choice of quench rate has an effect on the final outcome of the temperature quench, which we explore in the next section.

6.5.2 Lengthscales as a function of quench rate

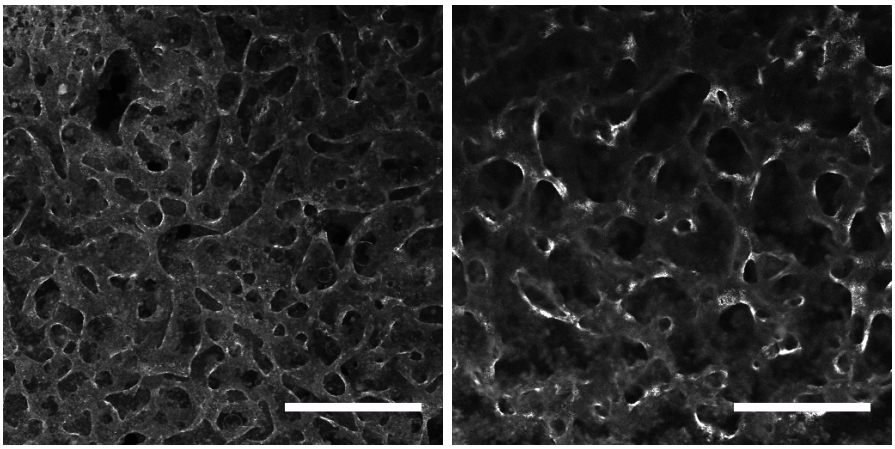

(a) **(b)**

Figure 6.3: Confocal micrographs of bimodal bijels prepared with identical amounts of nanoparticles (NPs, $r = 44$ nm) and microparticles (MPs, $r = 348$ nm), but quenched at 1°C/min (a) and 350°C/min (b), resulting in clearly different final bijel lengthscales. The signal arises from the fluorescence of RITC on the NPs. Scale bars 100 μm. Note that the micrographs were not taken at precisely the same position in the sample, so differences in absolute fluorescence intensity should be ignored.

We now explore the possible effect of quench rate on the final bimodal bijel lengthscale given our understanding of bijel formation from Chapter 3. We begin by inspecting confocal micrographs of bimodal bijels quenched at different rates as an example. Figure 6.3 shows two such micrographs, depicting a (a) slowly quenched (1°C/min) and (b) quickly quenched (350°C/min) bimodal bijel with no change in particle composition between (a) and (b) ($r_{\mathrm{NP}} = 44$ nm, $\phi_{\mathrm{NP}} = 0.24\%$ and $r_{\mathrm{MP}} = 348$ nm, $\phi_{\mathrm{MP}} = 0.69\%$). The signal in the micrographs arises from the fluorescence of the RITC on the NPs. Clearly there is a drastic difference in lengthscale between (a) and (b), and perhaps surprisingly the faster quench results in the larger lengthscale.

To continue the investigation, we prepared two further bijel samples with different volume fractions of particles and again quenched at different rates. Figure 6.4 shows the final bijel lengthscales for three different NP and MP combinations, as a function of the total scaled volume fraction. The relative amounts of NPs and MPs ($\phi_{\mathrm{MP}} r_{\mathrm{MP}} / \phi_{\mathrm{NP}} r_{\mathrm{NP}}$) from left to right are 0.05, 0.36 and 0.46 (meaning that NPs are in excess in all cases), with the circled point corresponding to the bijel depicted in Figure 6.3(b) quenched at 350°C/min, whereas the two other

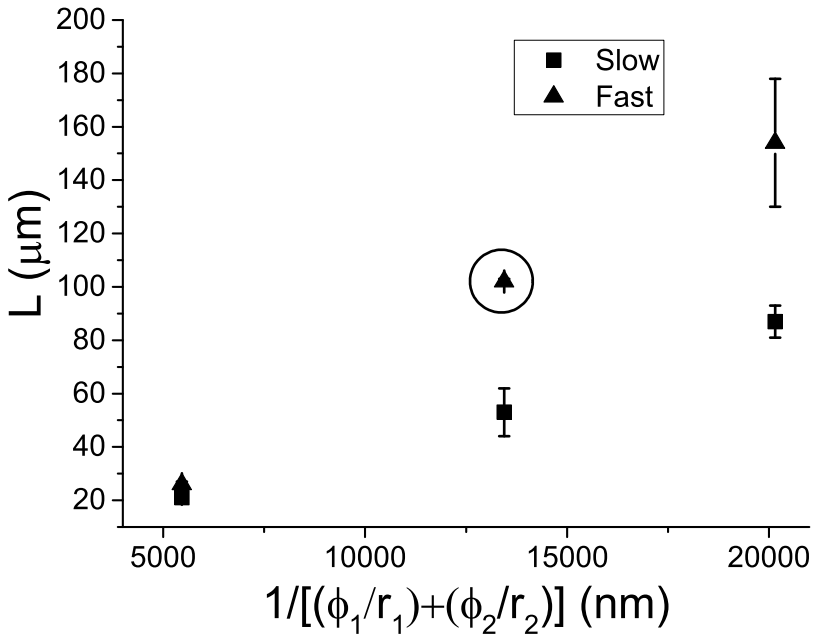

Figure 6.4: The lengthscales of bimodal bijels quenched fast (17°C/min, triangles) and slow (1°C/min, squares), as a function of total scaled volume fraction. The data point highlighted by the circle was quenched at 350°C/min as per the microwave method (see Chapter 2).

'fast' samples were quenched at the slower rate 17°C/min, but still an order of magnitude faster than the slowly quenched samples.

To qualify these results, note that small changes in L are observed in both monomodal cases (MPs or NPs) when different quench rates are used, but the differences here are much more significant. Since the quench rate effect becomes more pronounced as the relative amount of MPs is increased, we can assert that this (potentially useful) effect is due to the presence of the bimodal particle population (and not simply a more pronounced occurrence of the monomodal effect).

In the case where the relative area fractions are 0.36 and 0.46, when the quench rate is increased the lengthscale of the bijel increases. By using Equation 6.9, we can construct a range of possible causes of this behaviour.

Table 6.1 outlines the range of possible scenarios. Scenarios B, C, D and E are unlikely due to the large differences in L observed and the large individual decreases in α (and larger in the case of D or E) which would be required for such a change. For example, an increase in L of a factor of 2 means a reduction

Scenario	Explanation
A	α_{NP} and α_{MP} has decreased (but not necessarily by the same amount)
B	α_{NP} is constant while α_{MP} has decreased
C	α_{MP} is constant while α_{NP} has decreased
D	α_{NP} has increased while α_{MP} has decreased more
E	α_{NP} has decreased while α_{MP} has increased more

Table 6.1: The range of scenarios which could explain the increase in lengthscale of the bimodal bijels upon an increase in quench rate.

in total area of a factor of 4, and if this reduction in particle attachment were to only come from one of the species this would severely deplete that species from the interface. Since inspecting the confocal micrographs reveals similar levels of signal arising from FITC on the surface of the MPs and RITC on the surface of the NPs when comparing the samples quenched quickly and slowly, scenario A seems the only viable explanation to be explored.

MP/NP 'area'	MP 'area'	Total 'area'	Result (1°C/min)	Result (Fast)
	μm^{-1}	μm^{-1}	μm	μm
1.392	0.0035	0.0060	Fail	134(18)
0.456	0.0016	0.0050	87(6)	154(24)
0.364	0.0020	0.0074	53(9)	102(1)
0.164	0.0027	0.0190	Fail	55(15)
0.046	0.0008	0.0183	21(1)	26(1)
0.000	0.000	0.0395	20(1)	18(2)

Table 6.2: The results of quenching bimodal mixtures at 1°C/min or a fast rate (either 17°C/min or 350°C/min) with different amounts of MPs (r = 348 nm) and NPs (r = 44 nm)

Table 6.2 shows the data presented in Figure 6.4 plus two other data sets which include particle mixtures which fail to produce a bijel at the slow quench of 1°C/min. Note that by 'area' we are referring to the quantity ϕ/r, which although having units of inverse length, is concomitant with the (maximum) area of interface that the particles occupy. With the data in Table 6.2 we can say a number of things about the behaviour of bimodal bijels. The likelihood of failure appears not to depend on the total 'area' of added particles in the mixture, since bijel production fails at both a high (0.019 μm^{-1}) and low (0.006 μm^{-1}) maximal 'area' coverage. However, the systems which fail have the highest maximal 'areas' of MPs, 0.0027 μm^{-1} and 0.0035 μm^{-1}, although they do not have the highest values of MP vs NP area (1.392 and 0.164). So it appears that if you add too many MPs to the system (an 'area' greater than or equal to 0.0027

μm^{-1}, equivalent to a volume fraction of 0.93%) and quench at 1°C/min, you have to add a minimum amount of NPs (MP/NP less than 0.164) to have a chance at stabilizing a bijel, otherwise it will fail.

In terms of scenario A, it is difficult to say whether both particle uptake fractions reduce by the same amount when the quench-rate is reduced, or if the quench rate change effectively chooses a particle species for preferential absorption. Assuming the former, it seems strange that upon tripling the maximum total 'area' from 0.006 μm^{-1} to 0.019 μm^{-1}, which is more than enough required to stabilize a bijel with higher MP/NP values (and more than enough required if that area was solely made up of NPs) still doesn't result in bijel formation. This leads us to conclude that it is likely that slower quenches result in an increase in the uptake of MPs vs NPs, increasing the likelihood of the MPs being able to bend the particle-laden interface [1]. From a thermodynamic perspective this seems reasonable – the interfacial attachment energy of the MPs is almost an order of magnitude higher at constant interfacial tension as the NPs [4], and at early times during a slow quench, the attachment energy of the NPs may not even be high enough for irreversible attachment. This makes it more likely for MPs to attach irreversibly to the interface than NPs, although the evidence presented here is not entirely conclusive.

6.5.3 Kinetics

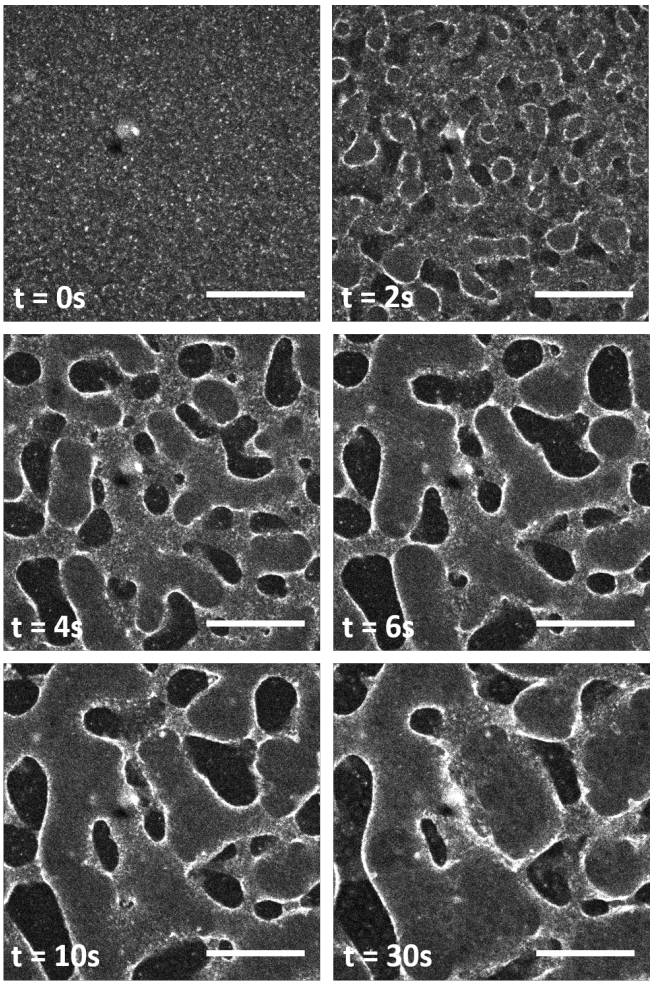

Figure 6.5: Confocal micrographs taken at different times during a 1°C/min quench of a bimodal mixture of NPs (r = 50 nm, ϕ_{NP} = 0.27%) and MPs (r = 367 nm, ϕ_{MP} = 1.82%). The fluorescence signal arises from the FITC on the surfaces of the MPs only. Scale bars 100 μm.

To potentially assist in our explanation of the bimodal bijel behaviour covered in the previous sections, we are interested here (as we were in Chapter 3) in the early time dynamics of the bijel (i.e. between the start of phase separation and emergence of a plateau in the $L(t)$ curve). The inclusion of two particle species may alter these dynamics, compared with the monomodal case – one obvious question is whether or not the failure mechanism is the same in both cases.

To investigate, we compare the timeseries of two bimodal samples, one which succeeds at producing a bijel and one which fails. Figure 6.5 shows confocal micrographs of a successful mixture of NPs (r = 50 nm, ϕ_{NP} = 0.27%) and MPs

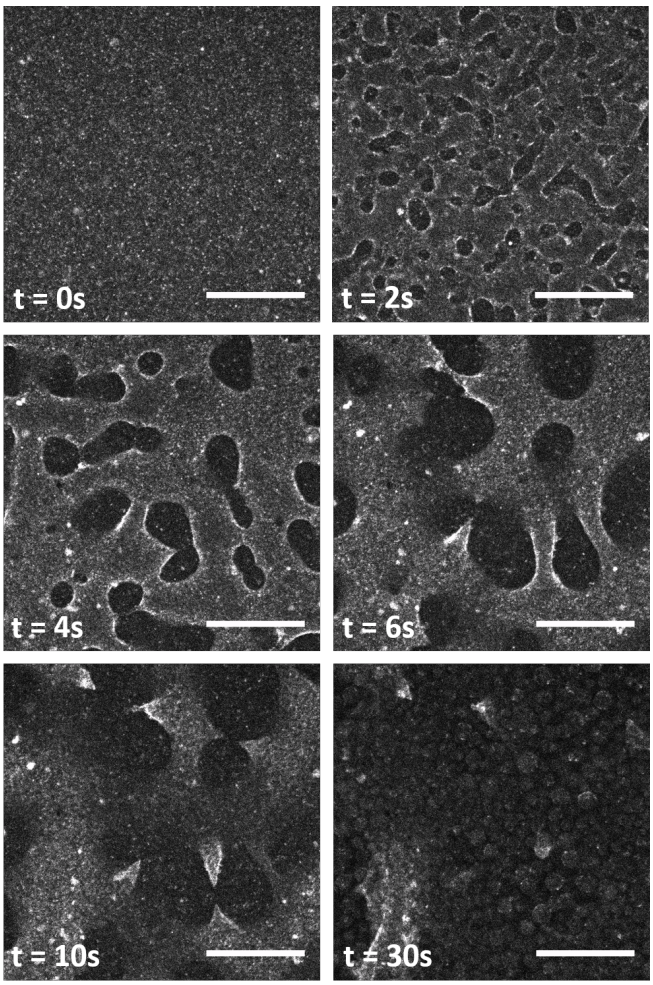

Figure 6.6: Confocal micrographs taken at different times during a 1°C/min quench of a bimodal mixture of NPs (r = 50 nm, ϕ_{NP} = 0.24%) and MPs (r = 367 nm, ϕ_{MP} = 1.69%). The fluorescence signal arises from the FITC on the surfaces of the MPs. Scale bars 100 μm.

(r = 367 nm, ϕ_{MP} = 1.82%), and Figure 6.6 shows confocal micrographs of a failure mixture of NPs (r = 50 nm, ϕ_{NP} = 0.24%) and MPs (r = 367 nm, ϕ_{MP} = 1.69%). These sets of particle mixtures would be expected to produce a bijel with a similar final characteristic lengthscale – but crucially the successful mixture has a slightly larger amount of NPs vs MPs, as well as having a slightly larger amount of particles overall.

From inspecting the micrographs of the failed system, it is clear that the failure is due to depercolation 'pinch-off' events, in a similar fashion to the monomodal MP case. Looking at the successful system, we still see some pinch-off events but much fewer than in the failed system, in the same way as the monomodal NP case [1]. The inter-connectivity of the domains is maintained until the interfacial particle

network jams somewhere between 10s and 30s, a substantially longer period than in the monomodal NP case (but note that the final lengthscale here is three times that of the final lengthscale in the monomodal NP case which would account for at least some of this difference). Hence, in the bimodal system, the failure of bijel formation is due to the same mechanism as in the monomodal system, with the presence of MPs leading to an unsustainable number of pinch-off events.

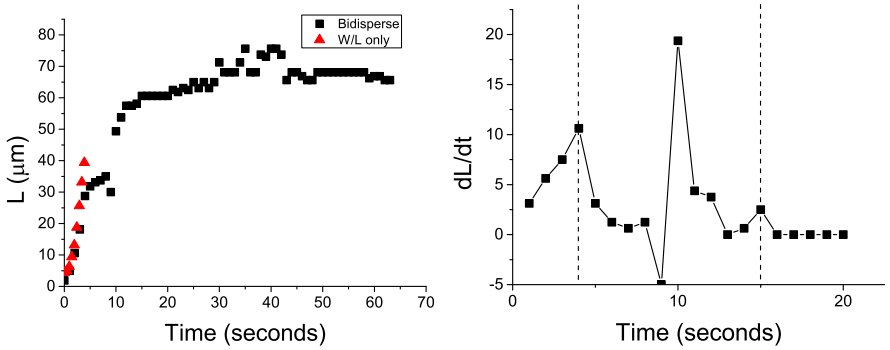

(a) **(b)**

Figure 6.7: (a) The lengthscale of a bimodal bijel during a 1°C/min quench (squares) and the lengthscale of the phase separating water/lutidine (W/L) mixture only (triangles). (b) the coarsening speed dL/dt as a function of time from the onset of phase separation at $t = 0$. The dashed lines indicate the beginning and end of the jamming process, with the gap defined as the jamming time (see text).

To further compare monomodal and bimodal systems, we measure the phase separation speed of the successful bimodal system (Figure 6.5) by applying the lengthscale analysis method (Chapter 2) to all the frames in the timeseries. The speed is defined as

$$dL/dt = \frac{L_{t_i} - L_{t_{i-1}}}{t_i - t_{i-1}} \tag{6.11}$$

Figure 6.7(a) shows the lengthscale of the phase separating mixture (and of the W/L mixture without particles) as a function of time, with t = 0 corresponding to the onset of phase separation, and (b) shows the corresponding phase separation speed dL/dt as a function of time (see Chapter 7 Figure 7.1 for a comparison between the monomodal and bimodal case as well as simulation data). The time interval marked by the dashed lines indicates the jamming time Δt_j, which for this bimodal bijel is approximately 11 seconds, about 7 seconds longer than the jamming time measured for a monomodal NP bijel [1]. Note however that the final lengthscale here was about 65 μm, whereas in the NP-only case studied in Chapter 3 the final lengthscale was about 20 μm, which may account for some of the increase in jamming time. The longer jamming time suggests that

this system is indeed more susceptible to failure, but not as susceptible as the equivalent monomodal MP system, which invariably fails at slow quench rates. Again, this is evidence that it is the MPs which contribute to the bijel production failure even in the presence of NPs.

6.5.4 Particle locations

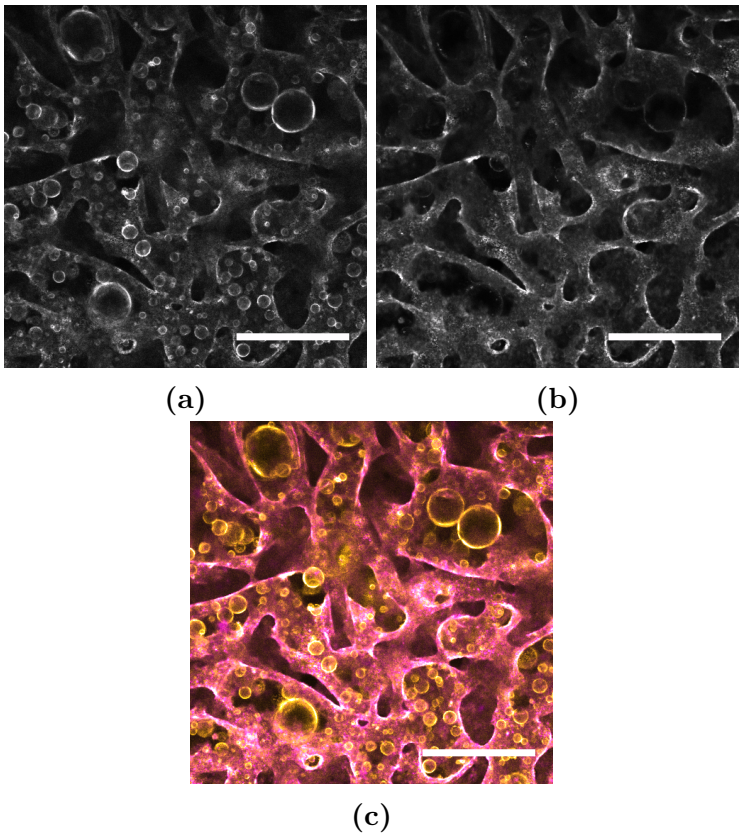

Figure 6.8: Confocal micrographs of a bimodal bijel with nanoparticles (NPs, $r_{NP} = 44$ nm, $\phi_{NP} = 0.24\%$) and microparticles (MPs, $r_{MP} = 348$ nm and $\phi_{MP} = 0.69\%$) quenched at 1°C/min. The fluorescence signal arises from the FITC-labelled MPs (a) and the RITC-labelled NPs (b). (c) An overlayed image to show the contrast between the particle locations; yellow for MPs, magenta for NPs. Scale bars 200 μm.

Simulations on bimodal bijels show particle segregation by size on the interface [5]. This is the first time that this behaviour has been looked for experimentally. To differentiate between the particle sizes, the large microparticles (MPs) are labelled with FITC, and the smaller nanoparticles (NPs) are labelled with RITC. These two dyes are excited by different lasers and the signal from both are separated by the use of emission filters and sent to separate PMT detectors.

Figure 6.8 shows confocal micrographs of a bimodal bijel, with $r_{NP} = 44$ nm, $\phi_{NP} = 0.24\%$, $r_{MP} = 348$ nm and $\phi_{MP} = 0.69\%$, quenched at 1°C/min. One striking difference is that although the percolating interface is visible in both the NP and MP channels, the droplets can only be clearly seen in the MP channel (hardly visible in the NP channel). At this level of magnification (limited by the difficulty of using oil immersion objective on this setup) there is not much evidence of size segregation of particles on the bicontinuous L-L interface (such segregation could take the form of patches of MPs or NPs or NPs/MPs residing at positions of high/low interfacial curvature). There are arguably a few areas of high curvature where the signal from the NPs is stronger, but in general there is no significant difference in the MP and NP signals along the L-L interface.

The data presented here supports the arguments of the previous section, i.e. that (bimodal) bijel failure during a slow quench is due to the same mechanism as the monomodal bijel, namely that an unsustainable number of pinch-off events are caused by the MPs. Even when bimodal bijel production is successful, as it is here, we see MPs (but not NPs) around droplets. If MPs and NPs were equally likely to promote pinch-off, we would expect to see both around droplets, but we only see MPs. Even if the droplets were formed by secondary nucleation, the fact that it is MPs which attach to their interfaces suggest that they are promoting curvature in one direction only.

6.6 Discussion

Here we summarize the results and discuss how they have enhanced our understanding of bijel formation, as well as identifying questions which remain to be answered. The experiments performed on bimodal bijels have allowed a quantitative estimation of the relative particle adsorption fractions, giving $\alpha_{\mathrm{NP}}/\alpha_{\mathrm{MP}} \approx 0.52$. This value is in line with previous results with monomodal MP and NP bijels (Chapter 3) and suggests that the geometrical parameter C in the $A_{\mathrm{LL}} = CL$ relationship (linking total stabilized liquid-liquid (L-L) area to the characteristic lengthscale L) is roughly the same in the monomodal and bimodal case. The reasons for the lower NP adsorption are not entirely clear, although from a thermodynamic perspective we would expect this to be the case. NPs will begin to attach irreversibly (i.e. attachment energy $E \geq 10\ k_b\mathrm{T}$) to the L-L interface during the quench at a later point in time than the MPs (E scales with r^2 [4]), by which time the total L-L area will be lower, and hence less

opportunity for particle attachment. This theory could potentially be explored by simulations.

The experiments have also uncovered the somewhat surprising phenomenon whereby the final bimodal bijel lengthscale L can be changed by varying the quench rate. Unfortunately, due to the range of particle volume fractions explored we have been unable to conclusively identify the cause of this change, although we hypothesize that more MPs vs NPs adsorb to the interface as the quench rate is reduced. We support this with a thermodynamic argument along the same lines as in the previous paragraph and the argument given in Chapter 3. As quench rate is reduced, the phase separation speed is reduced through the prefactor in the growth law [50]. Because of this, there will be a longer period of time during which the MPs are adsorbing irreversibly but the NPs aren't. Hence, reducing the quench rate reduces the opportunity for irreversible adsorption of NPs. Again, this could potentially be explored by simulations.

Despite the lack of a conclusive explanation, this phenomenon potentially opens up a novel route for controlling bijel lengthscales – for a monomodal bijel, L is controlled by r and ϕ only, whereas for a bimodal bijel, quench rate is an additional control parameter. This has the advantage of being able to obtain bijels of different lengthscales from the same initial mixture of liquids and particles, which may prove a useful property when scaling up bijel production for applications.

In a similar fashion to the MP-only bijel, some combinations of NPs and MPs fail to produce bijels at slow quench rates (1°C/min). By measuring the change in L over time, we arrive at a jamming time of about 11 seconds, significantly longer than the NP-only bijel, which means that it is more likely to fail at this quench rate. The jamming time may or may not be dependent on the relative amounts of NPs and MPs present. This is in line with current understanding (including evidence from simulations [5]), since a MP-only system quenched at 1°C/min will have an infinite jamming time (i.e. it never jams), an NP-only system has a jamming time of 4 seconds and the NP+MP system has a jamming time somewhere in between these two extremes.

Inspection of confocal timeseries shows the same failure mechanism in the bimodal case – unsustainable depercolation of the liquid channels via pinch-off events. Since this is what we see happening in the case of MP-only mixtures, we hypothesise that it is the MPs which are also responsible for the pinch-offs seen

here. Moreover, when we inspect confocal micrographs allowing us to differentiate between the signals arising from the MPs and NPs, we see a greater instance of MPs around droplets, whereas the NP signal only comes from the percolating L-L interface, which again suggests the culpability of the MPs in enforcing the L-L interface to bend in one direction only. However, we do not see much evidence of particle segregation other than this, with the signals from both particles being similar along the bicontinuous L-L interface. This could be further explored by trying to increase the magnification to look for segregation on the lengthscale of the particle sizes rather than the lengthscale of the channel width, and performing simulations to look for this phenomenon.

6.7 Conclusions

In this Chapter we have presented, for the first time, experimental results on bijels stabilized by bimodal particles. We have estimated that the interfacial uptake of nanoparticles is half that of microparticles which, as it corroborates previous results, suggests that the geometrical value C is the same for monomodal and bimodal bijels at least in the range of particle sizes studied so far. We presented a thermodynamic argument to take account of this, although this will have to verified, potentially by simulations.

In terms of size segregation on the interface, we find some limited but inconclusive evidence, which will have to be looked at again at higher magnifications. Bimodal bijels take over twice as long to jam than monomodal bijels and at certain particle concentrations fail due to a similar mechanism when quenched at 1°C/min. When bimodal bijels are formed, the quench rate is observed to change the final characteristic lengthscale, with faster quenches producing larger lengthscales. We have proposed that slower quenches promote the adsorption of microparticles over nanoparticles, but the precise reasons for this are still to be conclusively established. Importantly, this provides a new control parameter for choosing the final bijel lengthscale, which may be useful when scaling up bijel production for applications.

6.8 Acknowledgements

Mark Haw for useful discussions.

Chapter 7

Summary, discussion and outlook

7.1 Summary

In Chapter 1 we summarize the bijel research field and identify the rationale for the present studies. Before beginning the research there were several gaps between the knowledge obtained from simulation and the knowledge obtained from experimental preparation of bijels in the laboratory, with many open questions regarding the formation and stability of bijels. We address in this thesis the questions regarding the ability of nanoparticles to stabilize bijels, monogel formation (i.e. interfacial particle dynamics) and the role of the temperature quench rate in bijel formation generally.

In Chapter 2 we outlined the materials and procedures used throughout the thesis, most importantly the particle synthesis (and characterization), bijel preparation and imaging with confocal microscopy . We used reaction temperature to control the size of Stöber silica particles, and by adapting the concentration of dye in the reaction mixture, we prepared a range of particles with different sizes but similar surface chemistry, allowing us to explore the effect of particle size on bijel fabrication, structure and aging.

In Chapter 3 we prepared water/lutidine (W/L) bijels with nanoparticles (NPs) as opposed to microparticles (MPs). We found interesting deviations in behaviour from the equivalent structures stabilized by MPs. The most striking was the ability of NPs to stabilize bijels when slow (<17°C/min) quench rates were used. NPs provided a reduction in L less than expected based on $L \propto r/\phi$ at constant

volume fraction ϕ which we attributed to a lower interfacial uptake fraction $\alpha_{NP} < \alpha_{MP}$. The NPs took less time to form a permanent bonded network at the liquid-liquid interface (monogel) than the MPs, less than a minute as opposed to around half an hour. In an attempt to explain the results, we (along with Mike Cates and Aidan Brown [1]) developed a new theoretical framework for describing bijel formation in terms of interfacial bending moments and spontaneous radii of curvature induced by the particle layer, similar to the description of lipid membranes. We also demonstrated the ability of NP stabilized bijel to be polymerized in the same fashion as their MP counterparts, allowing us to translate the reduction in the lower bound of L into polymer monoliths with higher internal porosities.

In Chapter 4 we systematically characterized bijel morphology by measuring distributions of interfacial curvatures, and explored how the distributions depended on particle size, quench rate and time after bijel formation. We also compared the results to the curvature distributions of a simulated bijel structure (data provided by Kevin Stratford), and demonstrated the 3D bicontinuity of the bijel by performing a region growing analysis (carried out by Job Thijssen). We found that the most hyperbolic (most negative value for area-averaged Gaussian curvature) bijels were made when the smallest particles and the fastest quench rate was used. The simulated structure was found to be more hyperbolic than the equivalent experimental sample, although the existence of a distribution of contact angles in experiments, and the larger lengthscales explored in experiments, could feasibly account for this difference. MP-stabilized bijels were observed to mutate over a time period corresponding to the time taken for monogelation, whereas NP-stabilized bijels and nitromethane/ethanediol (NM/ED) bijels (a non-monogelling system) were not (although the NP system may mutate as it forms a monogel, but this takes less than one minute, less than the time taken to perform one measurement). The changes in the distributions were found to take place around the $\langle K \rangle = 0$ line, meaning that points of small negative Gaussian curvature were transforming into points of small positive Gaussian curvature, with the precise mechanisms still to be elucidated.

In Chapter 5 we studied particle dynamics in W/L and NM/ED bijels with diffusing-wave spectroscopy (DWS) and explored the effect of particle size and bijel age. We discovered that there is sufficient particle motion (between 10 and 100% of their radius) to completely decorrelate the scattered light, with a plateau emerging in the correlation functions after an aging time of between 1 and 3 hours

indicating a 2-mode process. The characteristic decay time τ_d increases as the samples age, to various degrees dependent on the specifics of the system. The NM/ED bijels showed aging behaviour similar to the universal aging observed in other soft matter systems, namely an exponential dependence of τ_d on sample age, whereas the W/L bijels showed a linear dependence. We suggested that we might have been observing the relaxation of internal stresses, which have been used to explain the final (late-time) complete decorrelation of the scattered light in other soft matter systems studied by light scattering. The sources of internal stresses could be, but are not limited to, the jamming transition, the monogelation process and/or the action of the particle layer on the liquid-liquid interface via the non-zero bending moments discussed in Chapter 4.

In Chapter 6 we prepared W/L bijels with two principle sizes of particles, i.e. NPs and MPs in the same mixture, to quantify the relative particle uptake $\alpha_{\mathrm{NP}}/\alpha_{\mathrm{MP}}$, look for particle segregation at the interface, and test this system's resilience to the use of slow quench rates. We found a relative uptake of roughly 0.5, corroborating the earlier assessment in Chapter 3, and found that the MPs prefer to reside at the interfaces of lutidine droplets, perhaps for the same reason as discussed in Chapters 3 and 4. When quenching samples with relatively similar amounts of NPs and MPs present, the resultant lengthscale L was found to be heavily dependent on the choice of quench rate, opening up a new avenue for tuning the bijel structure. Bimodal bijels were found to jam slower than their monomodal counterpart, suggesting that the particles either have more ability to reorganize before arriving at a jammed metastable state or simply take longer do to so compared to their monomodal equivalent.

7.2 Discussion

7.2.1 Experiments vs simulations

We have presented in this thesis several new pieces of experimental evidence which can be compared to simulations (and have done so already in Chapter 4). For example, the $L(t)$ graphs from Chapters 3 and 6 can be directly compared to the $L(t)$ graphs presented in the simulation studies [5, 11, 45, 48].

Figure 7.1 shows the experimentally measured coarsening behaviour of the bare W/L mixture, a monomodal (NP stabilized) and a bimodal W/L bijel quenched

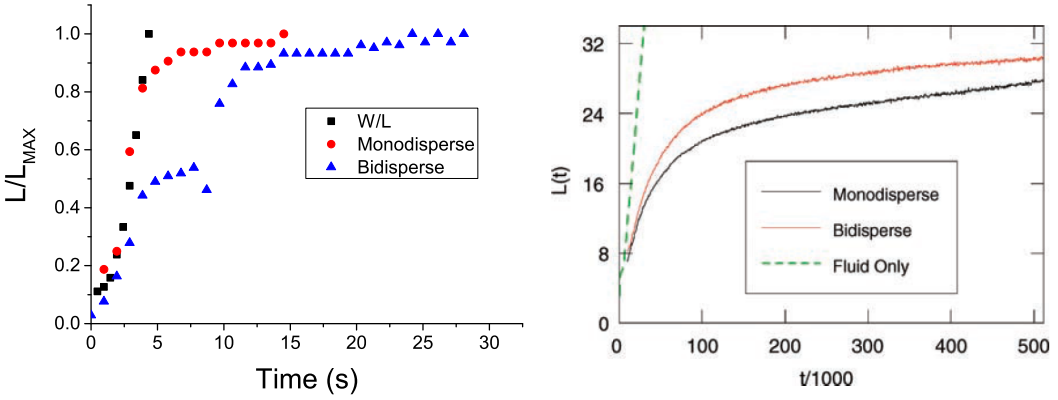

(a) (b)

Figure 7.1: (a) The experimentally measured coarsening behaviour for a bare water/lutidine (W/L) mixture, monomodal nanoparticle (r = 63 nm) stabilized W/L bijel and a bimodal (r = 63 nm and 348 nm) stabilized W/L bijel. The lengthscale values have been normalized by the final bijel lengthscale L_{MAX}. (b) The simulated coarsening behaviour as presented in Ref. [5].

at 1°C/min, along with the simulated coarsening behaviour as presented in ref [5]. In the monomodal case, the L-L coarsening follows the bare liquid case initially but then levels off to a plateau. With an appropriate rescaling, the experimentally measured $L(t)$ matches those measured in the simulated systems. The rescaling is required because the particles used in experiments are 10-100 times larger, and hence stabilize bijels with domain sizes 10-100 times larger. In the case of a bimodal particle population, the L-L coarsening again follows the bare liquid case initially then levels off to a plateau. The curve deviates from the bare W/L curve earlier and takes longer to reach the plateau. This, apart from the earlier deviation, qualitatively matches the $L(t)$ behaviour in Ref. [5]. The earlier deviation could indeed be present in the simulations but it is not clear from the figures presented. Note also the large discrepancies between the experimental systems and the simulated system – the former are volumetrically asymmetric and quenched slowly at 1°C/min, whereas the latter is volumetrically symmetric and subject to an instantaneous quench. The different quench rates, as we have demonstrated throughout this thesis, are likely to have an effect on the physics, possibly allowing the experimental bijel coarsening to follow the bare W/L coarsening for longer than in simulations.

More experimental evidence which can be compared to simulations is the mean-squared displacement (RMSD) data calculated in Chapter 5 from the diffusing-wave spectroscopy (DWS) measurements. Figure 7.2 shows the root mean squared

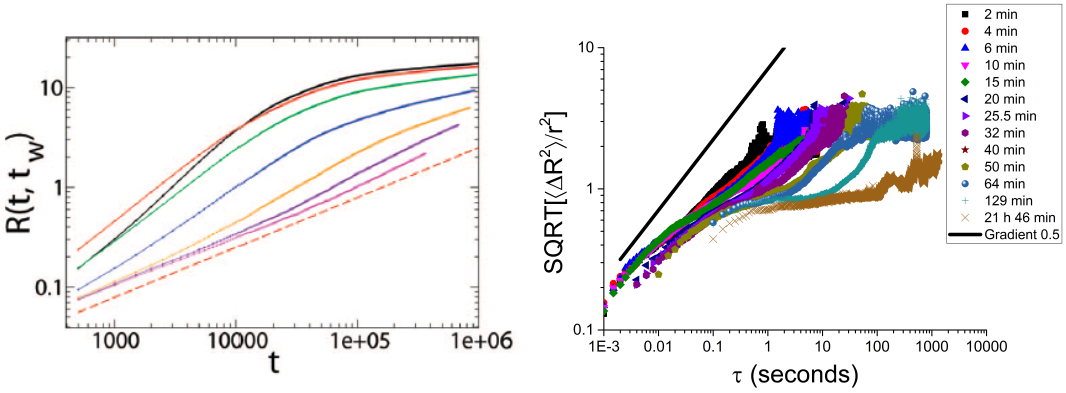

(a) **(b)**

Figure 7.2: (a) The simulated root mean squared displacements (RMSD) of the interfacial colloidal particles (r = 5 nm) as presented in ref [11] as a function of time, increasing from top to bottom. The red dashed line has gradient 1/2 which indicates diffusive motion. (b) The root mean squared displacements (RMSD) of the particles in a nanoparticle (NP, r = 63 nm) stabilized water/lutidine (W/L) bijel as measured by diffusing-wave spectroscopy in Chapter 5 labelled by sample age. The solid black line has gradient 0.5 which indicates diffusive motion.

displacements (RMSD) of the interfacial particles (r = 5 nm) in simulations [11] and the DWS measured mean-squared displacement (MSD) of interfacial NPs (r = 63 nm) in a W/L bijel. In some respects, the data qualitatively matches the simulations. As the sample age increases, the MSD curves shift downwards on the y-axis. The simulation MSDs also show an initial diffusive period followed by a levelling off for 'young' bijels, and for 'old' bijels the behaviour is entirely diffusive. However, the experimental MSDs show a return to either diffusive or slightly subdiffusive behaviour after the levelling-off at long times. This discrepancy is probably because the experiments greatly exceed the run time of the simulations. The disappearance of the levelling-off in the simulations is probably due to the fact that the simulations only proceed up to a few multiples of the Brownian time of the particles, and as the particles slow down as the bijel ages this lengthens the period of diffusive motion, while reducing the magnitude of the distances travelled (i.e. a downward shift on the y-axis).

In Chapter 3 we hypothesized that more NPs than MPs remain in the liquid channels (i.e. not at the interface) and in Chapter 6 we measured the relative amounts of NPs and MPs which make it to the interface and found that NPs attach 50% less readily than MPs under identical conditions. We did not however manage to produce an absolute estimate of the fraction of particles left behind

in the liquid channels, since an analytical relationship between bijel lengthscale and total interfacial area is lacking due to the bijel's complex shape. However, we can estimate the fraction from Ref. [11], which simulated approximately 8000 colloidal particles and measured the number of 'free' particles as a function of time. The number of free particles observed was between 0 and 4% – an ostensibly low amount, and unlikely to be true in experiments given the strong (and even stronger in the case of NPs) fluorescence signal from the lutidine-rich channel. Future simulations which could vary particle size and quench rate could study the relationship between these parameters and the number of free particles.

7.2.2 Bijel fabrication paradigms

Through the modification of pre-existing experimental procedures, from particle synthesis to bijel fabrication, we have reduced the lower bound on L (in W/L bijels) to around 10 μm by using smaller particles at the liquid-liquid interface. This makes use of charge-stabilized Stöber silica particles, dried at high temperature to obtain neutral wetting properties. The lower bound may be reduced to about 1 μm (by increasing ϕ) if more of these particles can be dispersed, however the dispersion becomes more difficult as particle size is reduced. This presents an experimental challenge which, whilst potentially difficult, is by no means impossible. But, unfortunately, we have shown in Chapter 3 that this overall approach (of using redispersed dried charge-stabilized silica) finds its limit at a particle size of about $r = 44$ nm, because the reduction in r is offset by a decrease in the attachment fraction α to the liquid-liquid interface. To achieve a further order of magnitude reduction in L, and hence probe the lengthscales envisaged in simulations, a new paradigm of bijel fabrication must be sought, possibly utilising steric stabilization with a combination of hydrophobic and hydrophilic hairs.

Nonetheless, the understanding of the current paradigm has been improved by this thesis. We now know that particles of size $r = 63$ nm are relatively insensitive to the quench rate used in the procedure, which will assist in the bijel's future development for applications, especially when the production is scaled up to an industrial level. As sample size is increased it becomes more difficult to maintain a homogenous and fast heating step, which for the original MP system would be a problem, which has now been potentially solved by the use of NPs. The knowledge about the effect of particle size, combined with the use of commercial

silica particles as outlined by Cai *et al.* [78] to remove the need for tuning the wetting properties by drying, has the potential to provide more robust protocols for the scaling up of bijel formation.

In addition to the qualitative success/failure scenarios we now have a quantitative measure of the structural differences between samples prepared with different particle sizes and quench rates thanks to Chapter 4. If and when further fine-tuning of the bijel morphology is required for applications, combinations of particle size and quench rate can be used not only to achieve structures of the desired porosity L, but also hyperbolicity $\langle K \rangle \Sigma^{-2}$.

Chapter 6 outlines a brand new (experimental) paradigm of bijel formation, where we can use two different particle sizes in the same sample. What this could mean in practice is the inclusion of a small amount of NPs to decrease the system's sensitivity to quench rate while retaining the morphological characteristics (e.g. relatively large L and low hyperbolicity) of an MP bijel. This adds yet another avenue of control over bijel morphology which could aid its development for applications.

7.2.3 Aging

One theme which emerges from the results presented in this thesis is that of bijel aging. In previous studies when only the characteristic lengthscale L was monitored over time, the bijel appeared to be in a completely jammed, unperturbed state. Now that we have studied bijels in terms of interfacial curvature and particle dynamics, we have seen that bijels do continue to age post-formation. Interestingly however, the aging observed in curvatures (mutation) do not exactly align with the aging observed for particle dynamics (an increase in τ_d with waiting time), as explained below.

MP W/L bijels are shown to mutate over a period of about an hour in Chapter 4, which is roughly the period associated with monogel formation in that system. Both a quickly-monogelling system (NP W/L) and a non-monogelling system (MP NM/ED) do not exhibit such a mutation. Hence, it is likely that the monogelation mechanism has something to do with this behaviour. However, for all systems, the particle dynamics slow down with time regardless of monogelation behaviour, suggesting that there is some other mechanism(s) at play. Although we suggest that the idea of relaxation of internal stresses could be applied to

bijels, as it is to diffusion-limited cluster aggregation (DLCA) gels, the fixed probe lengthscale in DWS (l^*) makes it difficult to provide a more conclusive analysis. One interesting question to be explored in this respect is whether or not particle rearrangements are confined to the L-L interface or, like DLCA gels, rearrangements can occur in 3 dimensions. Such rearrangements were seen when simulating the evolution of a monogel with only a short-ranged attraction present [91] – but with a long-ranged repulsive interaction added, in essence providing a barrier to 3D rearrangement of a few $k_\mathrm{b}T$, the monogel network persisted with a much slower rate of rearrangement. The presence of the L-L interface would presumably raise this barrier height considerably because of the individual particle interfacial attachment energy [4]. Although the resultant energy barrier would be large (compared to $k_\mathrm{b}T$), it may be overcome by cooperative effects (akin to the keystone effect [59]) which might emerge at long wait times.

7.3 Outlook & open questions

As mentioned above, in order to completely bridge the gap between experiments and simulations in terms of lengthscales, a new bijel fabrication paradigm is required which does not rely on colloidal charge stabilization. For example, sterically-stabilized polystyrene (PS) latex particles can be used as Pickering emulsifiers [160–162], as well as sterically-stabilized PMMA [159, 163] and silica [164] although the wetting properties of such particles may not be appropriate for the W/L system. Any success at reducing L in the W/L system even further would expand its applicability.

Another gap which needs to be bridged is the effect of the finite quench rate on bijel formation. In experiments there will always be a finite quench rate, whereas simulations have so far mainly used instantaneous quenches. Simulating the spinodal decomposition with a time dependent interfacial tension may shed light on the reason(s) why particle attachment fractions α depend on particle size. We hypothesize in Chapter 3 that this could be due to smaller particles spending a longer time in a reversible attachment regime, with their interfacial attachment energy below some value (say, 10 k_bT), but we have no direct evidence to support this hypothesis over any other. The disruption and jamming times calculated using the new theoretical framework at the end of Chapter 3 should be verified by simulations if possible.

There are also some other experimental observations which have yet to be looked at in simulations. For example, In Chapters 3 and 6 we suggest that the interfacial particle attachment fractions decrease when particle size is decreased. this could be looked at along with the effect of quench rate as discussed above, if such a simulation scheme can be devised. Also, the dependence of the curvature distributions on particle size and quench rate could also be measured for simulations given the image analysis protocols devised in Chapter 4.

Although we measured the interfacial particle dynamics with DWS we have not been able to directly verify or disprove the proposed mechanisms of monogelation [91]. What could help in this endeavour would be finding a way to use a different technique, for example differential-dynamic microscopy, to allow a range of lengthscales to be probed, which would allow the separation of the possible mechanisms at play during the bijel aging. It would also be interesting to see if the bijel does indeed sit within the universal picture for aging, or whether it exhibits aging phenomenon not accounted for under this model.

Chapter 8

Conclusions

This thesis has explored experimentally (and in some cases theoretically and computationally) many important and interesting aspects of bijels, such as the effect of particle size and temperature quench rate on the structure and dynamics as well as preparing (for the first time in the laboratory) bijels stabilized by bimodal particles. While answering and beginning to answer some of the open questions identified at the outset, several questions remain open for future consideration. In addition, by experimentally characterizing bijels in new ways (systematic characterization of interfacial curvatures in Chapter 4 and measurement of dynamics in Chapter 5) we have introduced new questions to be considered.

We have demonstrated that bijel formation with nanoparticles (NPs, $r = 63$ nm) in the water/lutidine (W/L) system is more robust than the equivalent process with microparticles (MPs, $r \approx 300$ nm), owing to a drastically reduced sensitivity to quench rate and quicker monogelation formation. We (along with Mike Cates and Aidan Brown) introduced a new theoretical framework to take account of the reduced sensitivity to quench rate (published in Ref. [1]). However, the theory remains to be more rigorously tested. For example, if a simulation methodology could be devised which would take into a account a finite quench rate along with a range of particle sizes, the scaling of the jamming and disruption times with particle size and quench rate could be verified. Nonetheless, we can use this knowledge to inform future experimental preparation of bijels and can in principle produce polymer scaffolds with a channel diameter of roughly 1 μm, widening the applicability of the bijel approach for the fabrication of functional

materials. However, to go below 1 μm, a new design paradigm must be sought based on steric stabilization rather than electrostatic, of which there are a few candidate routes (see Chapter 7).

We have also demonstrated that bijel topology can be tuned by varying particle size and quench rate, which will inform future decisions about the tailoring to specific applications. Smaller particles and faster quenches result in more hyperbolic 'open' structures, preferable for applications involving flow through the bijel channels. A more 'closed' structure might be preferable for applications involving filtration by size, for example (small species becoming trapped in thin necks). This aspect of bijels could be explored in future simulations, to verify the role of the particle layer in modifying the curvature distributions, given our establishment of robust image-analysis protocols in Chapter 4 which can be used on both experimental and simulation data. The apparent curvature mutation with sample age could also be explored in this way, as well as experimentally with, for example, higher magnification/resolution imaging combined with improved mitigation for the effects of drift, to monitor the mutation in real-space. Also, a full theoretical description of this phenomenon is lacking which, if developed, may offer additional insight for the fine-tuning of bijel macro- and micro-structure.

For the first time, bijel dynamics have been measured experimentally, using diffusing-wave spectroscopy (DWS). We have demonstrated that bijels age, but show different aging behaviour dependent on the specific combination of particle size and coexisting liquids. The process of forming a permanent particle gel ('monogel') at the interface appears to accelerate the aging, and a system which does not form a monogel shows characteristics of universal aging, placing it within a larger class of jammed (i.e. out of equilibrium) systems. However, to elucidate the precise mechanisms of particle motion, e.g. particle rearrangements or movement of the particle-laden liquid-liquid interface, more experimental study is required with a technique that can separate out the lengthscales of motion. Then, the individual particle trajectories and dynamics can be compared to the proposed mechanisms for monogelation proposed in Ref. [91].

Also for the first time, we prepared W/L bijels using two different sizes of particles, NPs and MPs, to make a 'bimodal' bijel. The coarsening behaviour of the bimodal bijel qualitatively matches the behaviour predicted by simulations [5], and we have quantitatively estimated the ratio of interfacial particle attachments – NPs adsorb half as readily as MPs. Again, this phenomenon (more NPs being left behind in the liquid channels than MPs) could be explored in simulations

if both quench rate and particle size are varied. We presented evidence that the MPs prefer to reside at interfaces with curvature in one direction only i.e. droplet interfaces, but did not find any evidence of particle segregation by size on the bicontinuous bijel interface, although the search for such evidence was not exhaustive. Higher magnification and resolution imaging may resolve this question in future. We also demonstrated the potential for controlling lengthscale at fixed (combined) particle volume fraction by varying the quench rate – faster rates resulted in smaller lengthscales.

Overall, we have identified the limits of current experimental protocols and suggested a path to continue towards the goal of realizing the simulated structures in the laboratory. We have also introduced a new quantitative analysis in terms of bijel topology and identified new design rules which could be used for tailoring the bijel structure for specific applications. Bijel dynamics have been probed for the first time, as have the behaviour of bijels stablilized by bimodal particles, with avenues for future research identified.

Appendix A

Timescales of bijel formation

A.1 Disruption time

The following is adapted from Ref. [1]. Following Canham and Helfrich [121, 122], we start with the bending-energy density of a membrane

$$w = 2\kappa \left(H - C_0\right)^2 + \kappa_{\mathrm{G}} K \ , \tag{A.1}$$

in which κ is the bending modulus, H the mean curvature, C_0 the spontaneous curvature, κ_{G} the Gaussian bending modulus and K the Gaussian curvature. Assuming the topology of the surface does not change substantially during the crucial stages of bijel formation, we omit the K term [165]:

$$w = 2\kappa \left(H - C_0\right)^2 \ . \tag{A.2}$$

Next, we consider the (generalized) driving force F towards spontaneous curvature. Taking H as constant over a small membrane patch,

$$\begin{aligned} F &= \tfrac{\partial w}{\partial H} \\ &= \tfrac{\partial}{\partial H}\left[2\kappa \left(H - C_0\right)^2\right] \\ &= -4\kappa \left(C_0 - H\right) \ . \end{aligned} \tag{A.3}$$

Eq. (A.3) resembles Hooke's law for a spring with spring constant $k = 4\kappa$ and

extension $u = (C_0 - H)$. The equilibrium position of the spring is $H = C_0$, which is a minimum as $(\partial^2 w/\partial H^2) = 4\kappa$ (which is positive for $\kappa > 0$). Note that it has been shown empirically that the average mean curvature $\langle H \rangle = 0$ for bijels [2, 54].

In order to understand how the driving force F scales with particle size r, we first consider how the spontaneous curvature C_0 and the bending modulus κ scale with r. C_0 has units of inverse length (m^{-1}) and is expected to scale as $-1/r$, which is backed up by analytical calculations for spherical particles on a spherical cap [119]. In that geometry, the result can also be explained using a scaling argument: to keep the angles fixed, including the particle's contact angle, both r and the radius of curvature R_c of the spherical cap have to be reduced by the same factor, showing that

$$C_0 = -\frac{1}{R_\mathrm{c}} \propto -\frac{1}{r} \ . \tag{A.4}$$

Note that C_0 also depends on the particle's contact angle θ and that $C_0 = 0$ for neutrally wetting particles ($\theta = 90°$) [119].

The bending modulus κ has units of energy (J). As it is expected to depend on the W-L interfacial tension γ_WL (units $\mathrm{N\,m}^{-1}$) and on the presence of the particles, one might guess

$$\kappa \propto \gamma_\mathrm{WL} r^2 \ . \tag{A.5}$$

This claim is backed up by analytical calculations of κ for a close-packed monolayer of spherical particles on a spherical cap [119].

In our experiments, the final bijel-channel width $L_\mathrm{f} \gg r$, so $|H| \sim 1/L_\mathrm{f} \ll |C_0|$ (Eq. (A.4)). Combined with Eqs. (A.3) and (A.5), this means the driving force F scales with r:

$$\begin{aligned} F &= -4\kappa\,(C_0 - H) \\ &\approx -4\kappa C_0 \\ &\propto -\gamma_\mathrm{WL} r^2 \cdot -\tfrac{1}{r} \\ &\propto \gamma_\mathrm{WL} r \ . \end{aligned} \tag{A.6}$$

In words, for the same binary liquid (γ_WL) and a given off-neutral wetting ($\theta \neq 90°$), the driving force towards the spontaneous curvature is smaller for NPs than it is for MPs, which can help explain why fabricating bijels is possible over a larger range of heating rates with NPs than with MPs.

To gain a simple estimate of the disruption time Δt_{d}, which is the time it takes for the driving force F to cause so much curvature that bijel formation fails, we balance F with a viscous drag force:

$$\begin{aligned} F &= F_{\mathrm{drag}} \\ &\propto \eta\lambda v \ , \end{aligned} \tag{A.7}$$

where η is viscosity, $\lambda \gg r$ the typical length scale of the disruption (independent of particle radius) and $v \sim \lambda/\Delta t_{\mathrm{d}}$. Combining Eqs. (A.6) and (A.7), we get

$$\Delta t_{\mathrm{d}} \propto \frac{\eta\lambda^2}{\gamma_{\mathrm{WL}} r} \ . \tag{A.8}$$

Alternatively, consider the equation of motion of a damped oscillator (compare Eq. (A.3)),

$$m\ddot{u} + \mu\dot{u} + 4\kappa u = 0 \ , \tag{A.9}$$

in which μ is a drag coefficient. We assume here that, at least initially, the drag mainly comes from the bulk fluids. In that case,

$$\mu = \eta\lambda^3 \ . \tag{A.10}$$

In our experiments $L_{\mathrm{f}} \gg r$, but if $L_{\mathrm{f}} \sim r$ then bulk drag may no longer dominate and effects of surface viscosity would have to be considered (which is outside of the scope of the current paper).

As the Reynolds number $\mathrm{Re} \ll 1$ here, even when considering motion at the scale of the channel width L, we can ignore the inertial term [166]:

$$\mu\dot{u} + 4\kappa u = 0 \ . \tag{A.11}$$

Re-writing Eq. (A.11) results in an expression for the rate of change of curvature $(\partial H/\partial t)$

$$\begin{aligned} \dot{u} &= -\tfrac{4\kappa u}{\mu} \\ \tfrac{\partial(C_0 - H)}{\partial t} &= -\tfrac{4\kappa(C_0 - H)}{\mu} \\ \tfrac{\partial H}{\partial t} &= \tfrac{4\kappa(C_0 - H)}{\mu} \end{aligned} \tag{A.12}$$

Let us denote the time when the interfacial particles start interacting as t_{in}. As

at that time the bijel channel width $L \gg r$, we can write

$$\left(\frac{\partial H}{\partial t}\right)_{\text{in}} \propto \frac{\kappa C_0}{\mu} \ . \tag{A.13}$$

For bijel disruption to occur, the curvature H has to change by a threshold amount $\Delta H_{\text{d}} \sim \lambda^{-1}$. For the disruption time, we can then write

$$\begin{aligned} \Delta t_{\text{disrupt}} &\sim \tfrac{\Delta H_{\text{d}}}{\kappa C_0/\mu} \\ &\propto \tfrac{\eta\lambda^2}{\gamma_{\text{WL}} r} \ , \end{aligned} \tag{A.14}$$

which is the same as Eq. (A.8). Interestingly, Eqs. (A.8) and (A.14) suggest that lower quench rates could be used when using high-viscosity fluids (larger η). It has been reported that the binary liquid nitromethane-ethanediol is more forgiving in bijel fabrication than the W-L system (the viscosity of ethanediol is 16 times larger than for water) [36].

A.2 Jamming Time

Consider a bijel surface S of area $A(t)$, i.e. the area of the liquid-liquid interface between the two channels is decreasing during coarsening. Then the 2D packing fraction of particles on S is

$$\phi(t) = \frac{N a_{\text{WL}}(\theta)}{A(t)} \ , \tag{A.15}$$

with $a_{\text{WL}}(\theta)$ the particle-interface cross-sectional area and N the number of interfacial particles. Here, we assume that both $a_{\text{WL}}(\theta)$ and N are constant during the crucial (jamming) stages of bijel formation, for there is hardly any area left on S for new particles to attach to. Eq. (A.15) still holds for the bijel in its final i.e. jammed state, so

$$\begin{aligned} \phi_{\text{f}} &= \tfrac{N a_{\text{WL}}(\theta)}{A_{\text{f}}} \\ N a_{\text{WL}}(\theta) &= \phi_{\text{f}} A_{\text{f}} \ , \end{aligned} \tag{A.16}$$

which leads to

$$\phi(t) = \phi_{\text{f}} \frac{A_{\text{f}}}{A(t)} \ . \tag{A.17}$$

As it is $L(t)$ rather than $A(t)$ that is typically reported from simulations and experiments, we write

$$A(t) = c_{\mathrm{g}} \frac{V_{\mathrm{c}}}{L(t)} \ , \tag{A.18}$$

in which c_{g} is a geometrical pre-factor and V_{c} is the total volume of the bijel channel (which is constant during the phase separation of a symmetric binary liquid). Combining Eq. (A.16) with (A.18) gives

$$\begin{aligned} \phi(t) &= \phi_{\mathrm{f}} \tfrac{c_{\mathrm{g}} V_{\mathrm{c}}}{L_{\mathrm{f}}} \tfrac{L(t)}{c_{\mathrm{g}} V_{\mathrm{c}}} \\ &= \tfrac{\phi_{\mathrm{f}}}{L_{\mathrm{f}}} L(t) \ , \end{aligned} \tag{A.19}$$

where we have assumed that c_{g} is constant i.e. the topology of the bijel does not change substantially during the final stages of (successful) formation (evidence in support of this assumption is found in Chapter 6).

If ϕ_{in} is the packing fraction at which interfacial particles start interacting, thereby affecting the phase separation [61], then

$$\begin{aligned} \phi_{\mathrm{f}} - \phi_{\mathrm{in}} &= \left(\tfrac{\phi_{\mathrm{f}}}{L_{\mathrm{f}}}\right) \int_{t_{\mathrm{in}}}^{t_{\mathrm{f}}} \tfrac{\mathrm{d}L}{\mathrm{d}t} \mathrm{d}t \\ &\approx \left(\tfrac{\phi_{\mathrm{f}}}{L_{\mathrm{f}}}\right) v_L \left(t_{\mathrm{f}} - t_{\mathrm{in}}\right) \\ \Delta t_{\mathrm{j}} &= t_{\mathrm{f}} - t_{\mathrm{in}} \approx \left(1 - \tfrac{\phi_{\mathrm{in}}}{\phi_{\mathrm{f}}}\right) \left(\tfrac{L_{\mathrm{f}}}{v_L}\right) \ , \end{aligned} \tag{A.20}$$

where in the second line we have used $L(t) \propto t$, which is valid in the relevant phase-separation regime for bijel formation (viscous-hydrodynamic) [50].

Note that Eq. (A.20) can explain several observations. First, the larger L_{f}, the longer the jamming time, which may help explain the empirical upper limit to bijel channel width [75]. Secondly, the larger the coarsening speed v_L, the shorter the jamming time. As v_L increases with heating rate, through its dependence on the temperature-dependent interfacial tension [117], this may help explain why heating faster facilitates successful bijel formation (even for MPs).

Appendix B

Fishtank effect

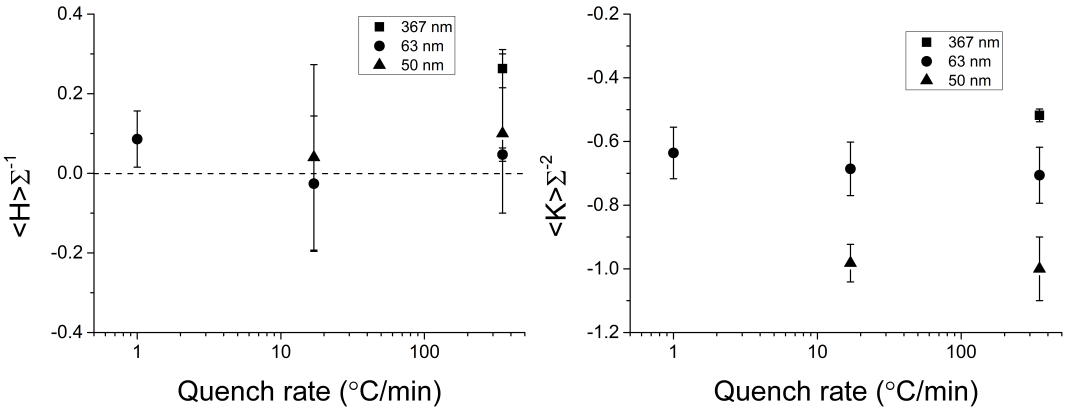

(a) (b)

Figure B.1: The area-averaged mean curvatures (a) and Gaussian curvatures (b) as a function of quench rate, with the three sizes of particles used in the study, after the data has been corrected for the fishtank effect. The absolute values are slightly changed compared to Chapter 4 Figure 4.10, but the trends remain. This analysis was not used in Chapter 4 because of the non-linear effect of stretching the voxels on the accuracy of the curvature measurement protocol, as evidenced in Chapter 4 Figure 4.5.

Bibliography

[1] M. Reeves, A. T. Brown, A. B. Schofield, M. E. Cates and J. H. J. Thijssen, *Phys. Rev. E.*, 2015, **92**, 032308.

[2] M. Reeves, K. Stratford and J. H. J. Thijssen, *Soft Matter*, 2016, **12**, 4082–4092.

[3] M. E. Cates and P. S. Clegg, *Soft Matter*, 2008, **4**, 2132–2138.

[4] R. Aveyard, B. P. Binks and J. H. Clint, *Adv. Colloid Interface Sci.*, 2003, **100-102**, 503–546.

[5] K. Stratford, R. Adhikari, I. Pagonabarraga, J.-C. Desplat and M. E. Cates, *Science*, 2005, **309**, 2198–2201.

[6] E. M. Herzig, K. A. White, A. B. Schofield, W. C. K. Poon and P. S. Clegg, *Nat. Mater.*, 2007, **6**, 966–971.

[7] M. Instruments, *Zetasizer Nano User Manual*, 1st edn, 2013.

[8] C. A. Grattoni, R. A. Dawe, C. Y. Seah and J. D. Gray, *J. Chem. Eng. Data*, 1993, **38**, 516–519.

[9] *LSM700 Manual*, Carl Zeiss, Jena, Germany, M60-1-0036e edn, 2011.

[10] https://www.micro–shop.zeiss.com/?s=30646114a6407a&l=en&p=us&f=f&a=i accessed March 2016.

[11] E. Kim, K. Stratford, R. Adhikari and M. E. Cates, *Langmuir*, 2008, **24**, 6549–6556.

[12] R. A. L. Jones, *Soft Condensed Matter*, Oxford University Press, Oxford, UK, 2002.

[13] J. M. Schultz, *Polymer materials science*, Prentice Hall, Upper Saddle River, New Jersey, USA, 1974.

[14] D. Lingwood and K. Simons, *Science*, 2010, **327**, 46–50.

[15] A. C. Balazs, T. Emrick and T. P. Russell, *Science*, 2006, **314**, 1107–1110.

[16] L. Cipelletti and L. Ramos, *J. Phys. Condens. Matter*, 2005, **17**, R253–R285.

[17] P. Becher, *Emulsions: Theory and Practice*, Chemical Rubber Co. Scientific Review Press, Cleveland, Ohio, USA, 2nd edn, 1965.

[18] T. Cosgrove, *Colloid Science*, Blackwell Publishing Ltd., Oxford, UK, 2005.

[19] W. Ramsden, *P. R. Soc. London*, 1903, **72**, 156–164.

[20] S. U. Pickering, *J. Chem. Soc. T.*, 1907, **91**, 2001–2021.

[21] B. P. Binks, *Curr. Opin. Colloid. In.*, 2002, **7**, 21–41.

[22] S. D. Kimmins and N. R. Cameron, *Adv. Funct. Mater.*, 2011, **21**, 211–225.

[23] A. R. Studart, U. T. Gonzenbach, I. Akartuna, E. Tervoort and L. J. Gauckler, *J. Mater. Chem.*, 2007, **17**, 3283–3289.

[24] B. P. Binks and T. S. Horozov, *Colloidal Particles at Liquid Interfaces*, Cambridge University Press, Cambridge, UK, 2006.

[25] N. Tanaka, H. Kobayashi, N. Ishizuka, H. Minakuchi, K. Nakanishi, K. Hosoya and T. Ikegami, *J. Chromatogr. A*, 2002, **965**, 35–49.

[26] D. Pukazhselvan, V. Kumar and S. Singh, *Nano Energy*, 2012, **1**, 566–589.

[27] I.-K. Sung, M. Mitchell, D.-P. Kim and P. J. A. Kenis, *Adv. Funct. Mater.*, 2005, **15**, 1336–1342.

[28] G. S. Chai, S. B. Yoon, J.-S. Yu, J.-H. Choi and Y.-E. Sung, *J. Phys. Chem. B*, 2004, **108**, 7074–7079.

[29] J.-C. Baret, F. Kleinschmidt, A. El Harrak and A. D. Griffiths, *Langmuir*, 2009, **25**, 6088–6093.

[30] D. J. McClements, *Curr. Opin. Colloid In.*, 2004, **9**, 305–313.

[31] K. Shinoda and B. Lindman, *Langmuir*, 1987, **3**, 135–149.

[32] M. J. Lawrence and G. D. Rees, *Adv. Drug Deliv. Rev.*, 2000, **45**, 89–121.

[33] A. Kogan and N. Garti, *Adv. Colloid Interface Sci.*, 2006, **123-126**, 369–385.

[34] A. J. Zarur and J. Y. Ying, *Nature*, 2000, **403**, 65–67.

[35] I. Capek, *Adv. Colloid Interface Sci.*, 2004, **110**, 49–74.

[36] J. W. Tavacoli, J. H. J. Thijssen, A. B. Schofield and P. S. Clegg, *Adv. Funct. Mater.*, 2011, **21**, 2020–2027.

[37] J. W. Cahn, *J. Chem. Phys.*, 1965, **42**, 93–99.

[38] J. Cahn, *Trans. Met. Soc. Aime*, 1968, **242**, 166–180.

[39] J. E. Hilliard, *Phase Transf.*, 1970, 497–560.

[40] V. M. Kendon, M. E. Cates, I. Pagonabarraga, J.-C. Desplat and P. Bladon, *J. Fluid Mech.*, 2001, **440**, 147–203.

[41] A. Onuki, *Phase Transition Dynamics*, Cambridge University Press, Cambridge, UK, 2002.

[42] *CRC Handbook of Chemistry and Physics*, ed. W. M. Haynes, CRC Press/Taylor and Francis, Boca Raton, FL, 96th edn.

[43] P. S. Clegg, E. M. Herzig, A. B. Schofield, S. U. Egelhaaf, T. S. Horozov, B. P. Binks, M. E. Cates and W. C. K. Poon, *Langmuir*, 2007, **23**, 5984–5994.

[44] E. Kim, K. Stratford and M. E. Cates, *Langmuir*, 2010, **26**, 7928–7936.

[45] F. Jansen and J. Harting, *Phys. Rev. E.*, 2011, **83**, 046707.

[46] S. Aland, J. Lowengrub and A. Voigt, *Phys. Fluids*, 2011, **23**, 062103.

[47] F. Günther, F. Janoschek, S. Frijters and J. Harting, *Comput. Fluids*, 2013, **80**, 184–189.

[48] S. Frijters, F. Günther and J. Harting, *Phys. Rev. E.*, 2014, **90**, 042307.

[49] J. M. Carmack and P. C. Millett, *J. Chem. Phys.*, 2015, **143**, 154701.

[50] I. Pagonabarraga, J. C. Desplat, A. J. Wagner and M. E. Cates, *New J. Phys.*, 2001, **3**, 9.1–9.18.

[51] S. Frijters and J. Harting, *http://arxiv.org/abs/1408.2974*, 2014, 1–4.

[52] D. J. Pine and A. Imhof, *Nature*, 1997, **389**, 948–951.

[53] V. N. Manoharan, A. Imhof, J. D. Thorne and D. J. Pine, *Adv. Mater.*, 2001, **13**, 447–450.

[54] M. N. Lee and A. Mohraz, *Adv. Mater.*, 2010, **22**, 4836–4841.

[55] H. Wang, C. C. Oey, A. B. Djurisic, M. H. Xie, Y. H. Leung, K. K. Y. Man, W. K. Chan, A. Pandey, J.-M. Nunzi and P. C. Chui, *Appl. Phys. Lett.*, 2005, **87**, 023507.

[56] M. Martina, G. Subramanyam, J. C. Weaver, D. W. Hutmacher, D. E. Morse and S. Valiyaveettil, *Biomaterials*, 2005, **26**, 5609–5616.

[57] S. C. Hess, A. X. Kohll, R. A. Raso, C. M. Schumacher, R. N. Grass and W. J. Stark, *ACS Appl. Mater. Interfaces*, 2015, **7**, 611–617.

[58] M. J. A. Hore and M. Laradji, *J. Chem. Phys.*, 2007, **126**, 244903.

[59] J. Tavacoli, G. Katgert, E. Kim, M. Cates and P. Clegg, *Phys. Rev. Lett.*, 2012, **108**, 1–5.

[60] K. D. Danov, P. A. Kralchevsky, B. N. Naydenov and G. Brenn, *J. Colloid Interface Sci.*, 2005, **287**, 121–134.

[61] T.-l. Cheng and Y. U. Wang, *J. Colloid Interface Sci.*, 2013, **402**, 267–278.

[62] K. A. Rumble, J. H. J. Thijssen, A. B. Schofield and P. S. Clegg, *Soft Matter*, 2016, **12**, 4375–4383.

[63] S. Melle, M. Lask and G. G. Fuller, *Langmuir*, 2005, **21**, 2158–2162.

[64] J. W. Tavacoli, J. H. J. Thijssen and P. S. Clegg, *Particle-Stabilized Emulsions and Colloids: Formation and Applications*, The Royal Society of Chemistry, 2015, pp. 129–168.

[65] W. Stöber, A. Fink and E. Bohn, *J. Colloid Interface Sci.*, 1968, **26**, 62–69.

[66] S. K. Park, K. D. Kim and H. T. Kim, *Colloid. Surface. A*, 2002, **197**, 7–17.

[67] J. W. Goodwin, R. S. Harbron and P. A. Reynolds, *Colloid Polym. Sci.*, 1990, **777**, 766–777.

[68] K. A. White, A. B. Schofield, P. Wormald, J. W. Tavacoli, B. P. Binks and P. S. Clegg, *J. Colloid Interface Sci.*, 2011, **359**, 126–135.

[69] K. A. White, A. B. Schofield, B. P. Binks and P. S. Clegg, *J. Phys.: Condens. Matter*, 2008, **20**, 494223.

[70] D. Beysens and D. Estève, *Phys. Rev. Lett.*, 1985, **54**, 2123–2126.

[71] D. W. Pohl and W. I. Goldburg, *Phys. Rev. Lett.*, 1982, **48**, 1111–1114.

[72] L. Zhuravlev, *Colloid. Surface. A*, 2000, **173**, 1–38.

[73] T. J. Sluckin, *Phys. Rev. A.*, 1990, **41**, 960–964.

[74] L. Imperiali, C. Clasen, J. Fransaer, C. W. Macosko and J. Vermant, *Mater. Horiz.*, 2014, **1**, 139.

[75] J. A. Witt, D. R. Mumm and A. Mohraz, *Soft Matter*, 2013, **9**, 6773–6780.

[76] H. Tanaka and T. Araki, *Phys. Rev. Lett.*, 1998, **81**, 389–392.

[77] N. Hijnen, D. Cai and P. Clegg, *Soft Matter*, 2015, **11**, 4351–4355.

[78] D. Cai and P. S. Clegg, *Chem. Commun.*, 2015, **51**, 16984–16987.

[79] M. Cui, T. Emrick and T. P. Russell, *Science*, 2013, **342**, 460–463.

[80] M. F. Haase, K. J. Stebe and D. Lee, *Adv. Mater.*, 2015, **27**, 7065–7071.

[81] K. C. Bryson, T. I. Löbling, A. H. E. Müller, T. P. Russell and R. C. Hayward, *Macromolecules*, 2015, **48**, 4220–4227.

[82] P. S. Clegg, *J. Phys.: Condens. Matter*, 2008, **20**, 113101.

[83] H. Firoozmand, B. S. Murray and E. Dickinson, *Langmuir*, 2009, **25**, 1300–1305.

[84] B. S. Murray and N. Phisarnchananan, *Food Hydrocolloid.*, 2014, **42**, 92–99.

[85] H. Firoozmand and D. Rousseau, *Food Hydrocolloids*, 2015, **48**, 208–212.

[86] S. Gam, A. Corlu, H.-J. Chung, K. Ohno, M. J. A. Hore and R. J. Composto, *Soft Matter*, 2011, **7**, 7262.

[87] J. A. Witt, D. R. Mumm and A. Mohraz, *J. Mater. Chem. A*, 2016, **4**, 1000–1007.

[88] M. N. Lee and A. Mohraz, *J. Am. Chem. Soc.*, 2011, **133**, 6945–6947.

[89] M. N. Lee, M. A. Santiago-Cordoba, C. E. Hamilton, N. K. Subbaiyan, J. G. Duque and K. A. D. Obrey, *J. Phys. Chem. Lett.*, 2014, 809–812.

[90] M. N. Lee, J. H. J. Thijssen, J. A. Witt, P. S. Clegg and A. Mohraz, *Adv. Funct. Mater.*, 2013, **23**, 417–423.

[91] E. Sanz, K. A. White, P. S. Clegg and M. E. Cates, *Phys. Rev. Lett.*, 2009, **103**, 255502.

[92] L. Bai, J. W. Fruehwirth, X. Cheng and C. W. Macosko, *Soft Matter*, 2015.

[93] M. Rüllmann and I. Alig, *J. Chem. Phys.*, 2004, **120**, 7801–7810.

[94] H. O. Carmesin, D. W. Heermann and K. Binder, *Phys. B Condens. Matter*, 1986, **65**, 89–102.

[95] C. G. Tan, B. D. Bowen and N. Epstein, *J. Colloid Interface Sci.*, 1987, **118**, 290–293.

[96] A. Van Blaaderen and A. Vrij, *Langmuir*, 1992, **8**, 2921–2931.

[97] A. Vrij and A. Van Blaaderen, *J. Colloid Interface Sci.*, 1993, **156**, 1–18.

[98] B. J. Berne and R. Pecora, *Dynamic Light Scattering*, Wiley, New York, 1976.

[99] W. S. Rasband, *ImageJ, U.S. National Institutes of Health, Bethesda, Maryland, USA*, http://imagej.nih.gov/ij/.

[100] D. Stamou, C. Duschl and D. Johannsmann, *Phys. Rev. E.*, 2000, **62**, 5263–5272.

[101] H.-J. Butt, *Langmuir*, 2008, **24**, 4715–4721.

[102] N. Sharifi-Mood, I. B. Liu and K. J. Stebe, *Soft Matter*, 2015, **11**, 6768–6779.

[103] L. Botto, E. P. Lewandowski, M. Cavallaro and K. J. Stebe, *Soft Matter*, 2012, **8**, 9957.

[104] L. Yao, L. Botto, M. Cavallaro, Jr, B. J. Bleier, V. Garbin and K. J. Stebe, *Soft Matter*, 2013, **9**, 779.

[105] R. K. Iler, *The Chemistry of Silica: Solubility, Polymerization, Colloid and Surface Properties and Biochemistry*, Wiley-Interscience, New York, 1979.

[106] A. Imhof, M. Megens, J. J. Engelberts, D. T. N. de Lang, R. Sprik and W. L. Vos, *J. Phys. Chem. B*, 1999, **103**, 1408–1415.

[107] M. Kobayashi, F. Juillerat, P. Galletto, P. Bowen and M. Borkovec, *Langmuir*, 2005, **21**, 5761–5769.

[108] A. Sadeghpour, F. Pirolt and O. Glatter, *Langmuir*, 2013, **29**, 6004–6012.

[109] B. Binks and J. Clint, *Langmuir*, 2002, **18**, 1270–1273.

[110] B. P. Binks and S. O. Lumsdon, *Langmuir*, 2000, **16**, 2539–2547.

[111] Z. Chen, F. C. Hsu, D. Battigelli and H. C. Chang, *Analytica Chimica Acta*, 2006, **569**, 76–82.

[112] C. Graf, Q. Gao, I. Schütz, C. N. Noufele, W. Ruan, U. Posselt, E. Korotianskiy, D. Nordmeyer, F. Rancan, S. Hadam, A. Vogt, J. Lademann, V. Haucke and E. Rühl, *Langmuir*, 2012, **28**, 7598–7613.

[113] J. Liang, Z. Xue, J. Xu, J. Li, H. Zhang and W. Yang, *Colloid. Surface. A*, 2013, **426**, 33–38.

[114] R. H. Webb, *Rep. Prog. Phys.*, 1999, **59**, 427–471.

[115] Z. Földes-Papp, U. Demel and G. P. Tilz, *Int. Immunopharmacol.*, 2003, **3**, 1715–1729.

[116] P. M. Chaikin and T. C. Lubensky, *Principles of condensed matter physics*, Cambridge University Press, Cambridge, UK, 1995.

[117] A. J. Bray, *Adv. Phys.*, 2002, **51**, 481–587.

[118] E. J. W. Verwey and J. T. G. Overbeek, *Theory of the Stability of Lyophobic Colloids*, Dover Publications, Inc. (Mineola, New York), 1999.

[119] P. A. Kralchevsky, I. B. Ivanov, K. P. Ananthapadmanabhan and A. Lips, *Langmuir*, 2005, **21**, 50–63.

[120] C. Planchette, E. Lorenceau and A.-L. Biance, *Soft Matter*, 2012, **8**, 2444.

[121] P. B. Canham, *J. Theor. Biol.*, 1970, **26**, 61–81.

[122] W. Helfrich, *Z. Naturforsch. C*, 1973, **28**, 693–703.

[123] T. Hashimoto, M. Itakura and H. Hasegawa, *J. Chem. Phys.*, 1986, **85**, 6118–6128.

[124] H. Jinnai, T. Kajihara, H. Watashiba, Y. Nishikawa and R. Spontak, *Phys. Rev. E.*, 2001, **64**, 010803.

[125] S. Hyde, B. W. Ninham, S. Andersson, K. Larsson, T. Landh, Z. Blum and S. Lidin, *The Language of Shape*, Elsevier, Amsterdam, 1997, pp. 1–42.

[126] S. T. Hyde, *Langmuir*, 1997, **13**, 842–851.

[127] Y. Nishikawa, H. Jinnai, T. Koga, T. Hashimoto and S. T. Hyde, *Langmuir*, 1998, **14**, 1242–1249.

[128] H. Saito, M. Yoshinaga, T. Mihara, T. Nishi and H. Jinnai, *J. Phys.: Conference Series*, 2009, **184**, 012029.

[129] H. Jinnai, T. Koga, Y. Nishikawa, T. Hashimoto and S. Hyde, *Phys. Rev. Lett.*, 1997, **78**, 2248–2251.

[130] https://svi.nl/FishtankEffect, accessed on 26th October 2015.

[131] Y. Matsushita, J. Suzuki and M. Seki, *Physica B*, 1998, **248**, 238–242.

[132] H. Jinnai, Y. Nishikawa, R. Spontak, S. Smith, D. Agard and T. Hashimoto, *Phys. Rev. Lett.*, 2000, **84**, 518–521.

[133] L. Isa, F. Lucas, R. Wepf and E. Reimhult, *Nature Commun.*, 2011, **2**, 438.

[134] E. D. Siggia, *Phys. Rev. A.*, 1979, **20**, 595–605.

[135] E. Gulari, *J. Chem. Phys.*, 1972, **56**, 6169.

[136] E. Zaccarelli, *J. Phys.: Condens. Matter*, 2007, **19**, 323101.

[137] P. J. Lu and D. A. Weitz, *Annu. Rev. Condens. Matter Phys.*, 2013, **4**, 217–233.

[138] H. M. Wyss, S. Romer, F. Scheffold, P. Schurtenberger and L. J. Gauckler, *J. Colloid Interface Sci.*, 2001, **241**, 89–97.

[139] J. Liu, V. Boyko, Z. Yi and Y. Men, *Langmuir*, 2013, **29**, 14044–9.

[140] L. Cipelletti, S. Manley, R. C. Ball and D. A. Weitz, *Phys. Rev. Lett.*, 2000, **84**, 2275–2278.

[141] A. Krall and D. Weitz, *Phys. Rev. Lett.*, 1998, **80**, 778–781.

[142] P. N. Segrè, V. Prasad, A. B. Schofield and D. A. Weitz, *Phys. Rev. Lett.*, 2001, **86**, 6042–6045.

[143] A. S. Negi and C. O. Osuji, *Phys. Rev. E.*, 2010, **82**, 031404.

[144] L. Cipelletti, L. Ramos, S. Manley, E. Pitard, D. A. Weitz, E. E. Pashkovski and M. Johansson, *Faraday Discuss.*, 2003, **123**, 237–251.

[145] D. Pine, D. Weitz, J. Zhu and E. Herbolzheimer, *J. Phys. France*, 1990, **51**, 2101–2127.

[146] V. Viasnoff, F. Lequeux and D. J. Pine, *Rev. Sci. Instrum.*, 2002, **73**, 2336.

[147] P. Pusey and W. Van Megen, *Physica A*, 1989, **157**, 705–741.

[148] F. Scheffold, S. Skipetrov, S. Romer and P. Schurtenberger, *Phys. Rev. E.*, 2001, **63**, 061404.

[149] A. S. Gittings and D. J. Durian, *Appl. Optics*, 2006, **45**, 2199–2204.

[150] D. A. Weitz, J. X. Zhu, D. J. Durian, H. Gang and D. J. Pine, *Phys. Scripta*, 1993, **T49B**, 610–621.

[151] P. D. Kaplan, M. H. Kao, A. G. Yodh and D. J. Pine, *Appl. Optics*, 1993, **32**, 3828–3836.

[152] A. Stocco, J. Crassous, A. Salonen, A. Saint-Jalmes and D. Langevin, *PCCP*, 2011, **13**, 3064–3072.

[153] W. Kob and J.-L. Barrat, *Phys. Rev. Lett.*, 1997, **78**, 4581.

[154] J.-P. Bouchaud, L. F. Cugliandolo, J. Kurchan and M. Mézard, *arXiv*, 1997, pp. 1–65.

[155] H. Tanaka, S. Jabbari-Farouji, J. Meunier and D. Bonn, *Phys. Rev. E.*, 2005, **71**, 021402.

[156] J. P. Bouchaud and E. Pitard, *Eur. Phys. J. E*, 2001, **6**, 231–236.

[157] M. E. Cates, R. Adhikari and K. Stratford, *J. Phys. Condens. Matter*, 2005, **17**, S2771–S2778.

[158] D. Ershov, J. Sprakel, J. Appel, M. A. Cohen Stuart and J. van der Gucht, *PNAS*, 2013, **110**, 9220–9224.

[159] J. H. J. Thijssen, A. B. Schofield and P. S. Clegg, *Soft Matter*, 2011, **7**, 7965–7968.

[160] J. I. Amalvy, S. P. Armes, B. P. Binks, J. A. Rodrigues and G. F. Unali, *Chem. Commun.*, 2003, 1826–1827.

[161] D. Dupin, S. P. Armes, C. Connan, P. Reeve and S. M. Baxter, *Langmuir*, 2007, **23**, 6903–6910.

[162] K. M. Reed, J. Borovicka, T. S. Horozov, V. N. Paunov, K. L. Thompson, A. Walsh and S. P. Armes, *Langmuir*, 2012, **28**, 7291–7298.

[163] J. W. O. Salari, F. a. M. Leermakers and B. Klumperman, *Langmuir*, 2011, **27**, 6574–6583.

[164] T. Saigal, H. Dong, K. Matyjaszewski and R. D. Tilton, *Langmuir*, 2010, **26**, 15200–15209.

[165] M. Nakahara, *Geometry, Topology and Physics*, Institute of Physics Publishing, Bristol and Philadelphia, 1st edn, 1990.

[166] W. B. Russel, D. A. Saville and W. R. Schowalter, *Colloidal Dispersions*, Cambridge University Press, Cambridge, UK, 1989.